PFC/RR-82-15 DOE/ET-51013-45

THERMAL & NON-THERMAL SUBMILLIMETRE EMISSION FROM ALCATOR TOKAMAK

by

S. EMIL KISSEL
Department of Physics
Plasma Fusion Center
Massachusetts Institute of Technology
Cambridge, MA 02139

June 1982

THERMAL & NON-THERMAL SUBMILLIMETRE EMISSION FROM ALCATOR TOKAMAK

by

S. EMIL KISSEL

S.B., M.I.T.

(1977)

SUBMITTED TO THE DEPARTMENT OF PHYSICS
IN PARTIAL FULFILLMENT OF THE
REQUIREMENTS FOR THE DEGREE OF

DOCTOR OF SCIENCE

at the
MASSACHUSETTS INSTITUTE OF TECHNOLOGY
June 1982

Signature of Author _____
Department of Physics
31 April 1982

Certified by _____
Prof. Ronald R. Parker
Thesis Supervisor

Accepted by _____
Prof. George F. Koster
Chairman, Department Committee

THERMAL & NON-THERMAL SUBMILLIMETRE EMISSION FROM ALCATOR TOKAMAK

by

S. EMIL KISSEL

Submitted to the Department of Physics on 31 April 1982
in partial fulfillment of the requirements for the Degree of
Doctor of Science in Physics

ABSTRACT

An experimental investigation was undertaken of submillimetre radiation from The Alcator Tokamak.

Thermal emission at the cyclotron frequencies was used to determine spatial electron temperature distributions. Measurements of temperature profiles corroborated classical models of plasma electrical conductivity, and provided graphic displays of unusual discharge behaviour. Temperature fluctuations, such as sawteeth, were also investigated.

Non-thermal radiation was observed at the electron plasma frequency, and occurred in two distinct fashions; a steady broadband feature, and a fluctuating emission of very narrow bandwidth. The fluctuating emission has not been previously documented from Tokamak plasmas. Pertinent theoretical considerations are outlined.

Thesis Supervisor: Prof. R.R. Parker

TABLE OF CONTENT

SECTION NULL INTRODUCTION 7

SEC 0.1 The Alcator Tokamak 7
SEC 0.2 Organisation Of Thesis 8
SEC 0.3 Introduction To Instrument 10
SEC 0.4 List Of Symbols 12

SECTION ONE REVIEW OF CYCLOTRON EMISSION 15

SEC 1.1 Single Particle Emission 15
SEC 1.2 Plasma Effects 17
SEC 1.3 Optical Depth 19
SEC 1.4 Reflections & Polarisation 23
SEC 1.5 Temperature Profile 25
SEC 1.6 References & Figures 27

SECTION TWO ELECTRON TEMPERATURE PROFILES 35

SEC 2.1 Gaussian Profile 35
SEC 2.2 Comparison To Classical Resistivity 36
SEC 2.3 Profile Width 40
SEC 2.4 Profile Centre 42
SEC 2.5 References & Figures 43

SECTION THREE NON-GAUSSIAN PROFILES 51

SEC 3.1 Current Rise 51
SEC 3.2 Impurity Radiation 53
SEC 3.3 References & Figures 56

SECTION FOUR THIRD HARMONIC EMISSION 60

SEC 4.1 Reflections & Optical Depth 60
SEC 4.2 Profile Shape 62
SEC 4.3 References & Figures 63

SECTION FIVE TEMPERATURE FLUCTUATIONS 68

SEC 5.1 Fabry-Perot Interferometer 68
SEC 5.2 Sawtooth Instability 69
SEC 5.3 Sympathetic Plasma Oscillation 73
SEC 5.4 References & Figures 75

SECTION SIX DOMINANT PLASMA FREQUENCY EMISSION 81

SEC 6.1 Spectral Character 81
SEC 6.2 Review Of Previous Experiments 83
SEC 6.3 Cerenkov Emission 84
SEC 6.4 Ray Trapping 86
SEC 6.5 References & Figures 89

SECTION SEVEN FLUCTUATING PLASMA FREQUENCY EMISSION 96

SEC 7.1 Temporal Behaviour 97
SEC 7.2 Correlated Behaviour 99
SEC 7.3 Comparison With Other Experiments 100
SEC 7.4 References & Figures 101

SECTION EIGHT SPECTRAL MEASUREMENTS OF FLUCTUATING EMISSION ..110

SEC 8.1 Michelson Interferometer 110
SEC 8.2 Fabry-Perot System 112
SEC 8.3 High-Resolution Spectra 114
SEC 8.4 Shifts In Emitted Frequency 116
SEC 8.5 References & Figures 118

SECTION NINE FLUCTUATING EMISSION: PLASMA WAVES 126

SEC 9.1 Stimulated Emission 126
SEC 9.2 Related Experimental Observations 128
SEC 9.3 Runaway Electrons 132
SEC 9.4 Plasma Wave Modes 134
SEC 9.5 Other Waves 136
SEC 9.6 Saturation Of Plasma Waves 137
SEC 9.7 Linear Radiation Processes 139
SEC 9.8 References & Figures 141

SECTION TEN FLUCTUATING EMISSION: NON-LINEAR EFFECTS 144

SEC 10.1 Resonance Conditions 144
SEC 10.2 Dispersion Relation 147
SEC 10.3 Non-linear Current 149
SEC 10.4 Absorption 151
SEC 10.5 Relation To Experiment 153
SEC 10.6 References & Figures 155

APPENDICES

APX 1 Optical Path 159
APX 2 Reflections & Polarisation 162
APX 3 The Michelson Interferometer 163
APX 4 Fourier Transform Spectroscopy 165
APX 5 Detector 170
APX 6 Calibration 171
APX 7 Atmospheric Water Vapour Absorption 174
APX 8 References & Figures 175

T O T H E H A P P Y F E W

ACKNOWLEDGEMENT

The Alcator experiment is a collective effort requiring the labours of numerous individuals. I would like to acknowledge the contributions by the support staff, technicians and scientists which allowed this work to be performed.

I am especially grateful for the guidance, encouragement, and occasionally necessary prodding provided by Dr. Ian Hutchinson. While I might question what pernicious product our proximity has presented him, there is no doubt of the great personal gain which I have received from our collaboration. Of greatest importance to me, as a student, has been the inspiration Ian has provided while serving as my role model of the true scientist and scholar.

I also thank the eclectic community of graduate student 'seagulls' with whom I have lived and shared. Their indomitable spirit surely makes them birds that have not lost faith in the high virtue of flying.

Dedicated in memory of Therese Crossley

with rue my heart is laden
for golden friends I once had
for many a rose lipped maiden
and many a light foot lad

by brooks to broad for leaping
the light foot boys are laid
the rose lipped girls are sleeping
in fields where roses fade

SEC 0.0 INTRODUCTION

This thesis presents measurements of submillimetre plasma radiation made in conjunction with the Alcator tokamak experiment during the period 1978 through 1981. As stipulated by the requirements for the award of Advanced Degrees, the included material represents novel results of original investigation. Most of the research documented herein is related directly to the operation of Tokamak devices and should be of interest to persons involved in this field, particularly the area of submillimetre plasma diagnostics. However, some of the items recorded are pertinent to the more general field of plasma physics. For this reason the reader is assumed to be knowledgeable in the area of plasma physics, but not specifically au fait in the arena of Tokamak research.

SEC 0.1 THE ALCATOR TOKAMAK

The Alcator C tokamak is shown schematically in fig.(1). The plasma is produced and confined within a magnetic field of toroidal geometry. A large toroidal field is externally produced by magnet coils, while a relatively smaller poloidal magnetic field is generated by an induced toroidal current within the plasma. The plasma current is necessary both to provide a confining force, and as a source of energy to heat the plasma. Because of the induced nature of the plasma current, the plasma generated can only be maintained for a finite time. This discharge time of several hundred milliseconds is much longer than characteristic collision or transport times, so a steady state is said to occur during the middle portion of a discharge. Typical parameters for steady state operation are:

Plasma Density:	$.5 \times 10^{14}$ - 6×10^{14} cm^{-3}
Plasma Current:	200 - 600 kAmperes
Electron Temperature:	1000 - 2000 Electron Volts
Ion Temperature:	800 - 1500 Electron Volts
Toroidal Field:	50 - 100 KGauss
Majority Species:	Hydrogen, Deuterium, Helium

Of course the temperature, current, and density are nill at the beginning and end of a discharge, so a rise and fall phase will precede and follow the steady state portion. The time evolution of a representative discharge is shown in fig.(2).

The hot plasma is confined entirely within a toroidal vacuum chamber so that measurements of plasma properties, particularly conditions at the discharge centre, must be inferred by some benign technique. For this reason the study of electromagnetic radiation emitted by the plasma is well suited as a diagnostic since by this method information can be gathered without perturbing the discharge. Observations of submillimetre wave radiation, in particular, have proven to be so useful in this respect, that in recent years measurement systems of this kind have become integral components of most tokamak experiments.

SEC 0.2 ORGANISATION OF THESIS

Cyclotron radiation is the principle mechanism responsible for most submillimetre emission from tokamak plasmas. A review of this radiation process is outlined in sec (1). An implication of cyclotron emission is the capability of determining electron temperature, in

particular the spatial dependence or temperature profile, from the second harmonic radiation. This technique has become standard recently, so there is nothing new in the presentation of temperature profiles per se. The purpose of the first half of the thesis is to apply the measured temperature profiles towards a better understanding of the physics involved in the discharge.

In sec (2), (3) it is shown that the measured profiles are consistent with a classical resistance model over the full range of operating conditions. The importance of this is the justification of applying the classical model to the plasma, and the generation of confidence toward the accuracy of the temperature profile measurements. Radiation at the third harmonic has been the topic of recent discussion, chiefly as a means of determining electron density. Sec (4) present measurements of the third harmonic emission which demonstrate that although the method is inadequate for acquiring density profiles, it does represent a useful technique for self-consistent calibration of the cyclotron diagnostic. This has important practical consequences for anyone involved in this area of tokamak research. Sec (5) presents measurements of temperature fluctuations commonly observed during tokamak operation. While these results demonstrate the wide ranged applicability of the submillimetre diagnostic, they also represent a worthwhile addition to the data base regarding phenomena, such as sawteeth, which are of current topical interest.

The remaining half of the thesis deals with radiation of a non-thermal origin, in particular emission near the plasma frequency. Some kind of radiation of this sort has been observed by most current and previous experiments. Theoretical explanations have been advanced to the point where the agreement between theory and experiment is quite good for some types of non-thermal emission. This is true of the emission discussed in sec (6). The material presented in this section however does expand upon the existing data, and helps distinguish two similar types of non-thermal emission. Sec (7), (8) present measurements of a second type of emission which has not been previously documented. The measurements in these sections clearly differentiate this new emission from the process discussed in sec (6). Sec (9), (10) review the pertinent theoretical and experimental results currently available concerning this novel type of radiation. The intent in these sections is not so much to identify the actual processes involved, as it is to focus attention on the sorts of mechanisms which can be reasonably expected to apply, and to indicate those which cannot.

SEC 0.3 INTRODUCTION TO INSTRUMENT

Most of the submillimetre spectral measurements presented within this thesis were made with a Michelson interferometer. A detailed discussion of the operation of this instrument is presented in the appendix. However, a brief introduction to the interferometer system is appropriate prior to a presentation of measured spectra.

Given some spectral intensity $I(\omega)$ of frequency ω, the output of an ideal interferometer is:

EQ (1) $$J(x) = \overline{J} - \frac{1}{2} \int_0^\infty I(\omega) \cos(\omega x/c)\, d\omega$$

where x is the optical path difference of the system. In operation the optical path is varied so that $J(x)$ is measured over a range of x. The spectral intensity is related to the interferometer output by the inverse transformation:

EQ (2) $$I(\omega) = \frac{-4}{c\pi} \int_0^\infty \cos(\omega x/c)\{J(x)-\overline{J}\}\, dx$$

where $\overline{J}$ is the average value of $J(x)$. The exact spectral intensity $I(\omega)$ can be constructed provided that $J(x)$ is measured over a semi-infinite range of x. In practice this is of course impossible. Instead x is periodically varied over a limited range. The spectral intensities deduced from eq (2) are thus based on incomplete sets of information, and therefore will have limited frequency resolution. The period with which x is varied sets the time resolution of the measured spectra. Since it is necessary to assume a constant $I(\omega)$ during one measurement cycle, the spectra will represent an average over this cycle time.

Two important aspects of the interferometric measurements can be summarised by the following: The produced spectra result from the application of some form of eq (2) to the entire interferometer output, not from individual measurements of intensities at separate frequencies. Although there is a direct relation between the path

difference x and the time during which the measurement of J(x) is made, no such relation connects the intensity at a specific frequency with a specific time. The intensity at a specific frequency results from information gathered over the entire time during which x is varied.

SEC 0.4 LIST OF SYMBOLS

Tokamak research has produced a vocabulary peculiar to the field. Producing a lexicography of Tokamak terminology would be a thankless chore, so the usage of non-standard terminology has been avoided. The commonly used symbols are listed below as a convenience. It should be noted that most of these quantities are functions of space or time or both.

a..... Temperature profile width

B..... Magnetic field (Toroidal)

I..... Plasma current

I(ω)... Spectral intensity

J(r)... Plasma current density

n..... Plasma density

n..... Refractive index

q..... Safety factor

R..... Major radius of torus

r_{lim}... Minor radius, limiter radius

T..... Temperature

V..... Toroidal loop voltage

v..... Particle velocity

Z_{eff}... Effective ion charge number

γ..... Relativistic factor

τ..... Optical depth

ω_p..... Plasma frequency

ω_c..... Gyrofrequency

η..... Resistivity

Subscripts, Superscripts

o..... Ordinary

x..... Extraordinary

0..... Central value

e..... Electron

i..... Ion

THE ALCATOR TOKAMAK

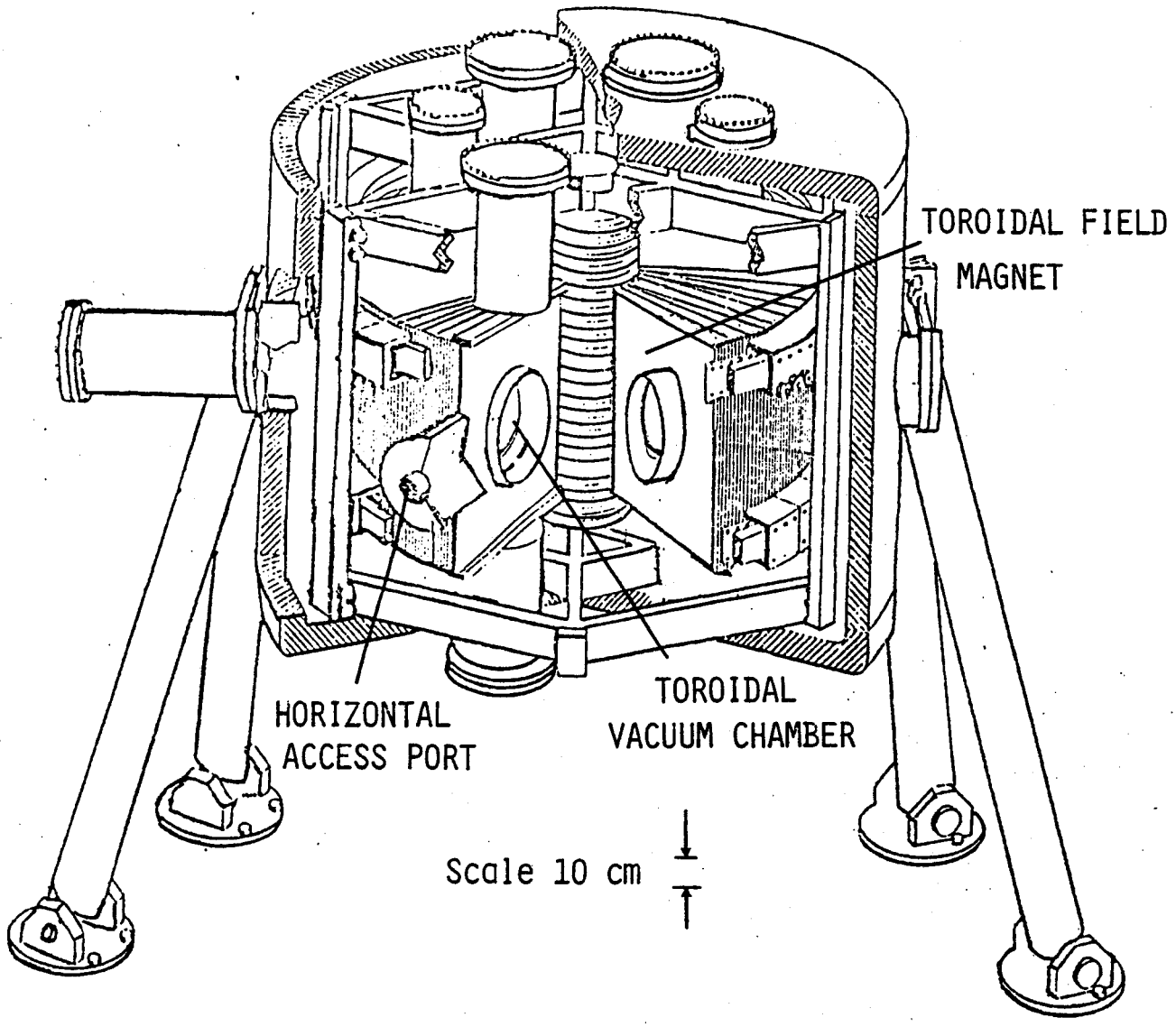

Fig.(1)

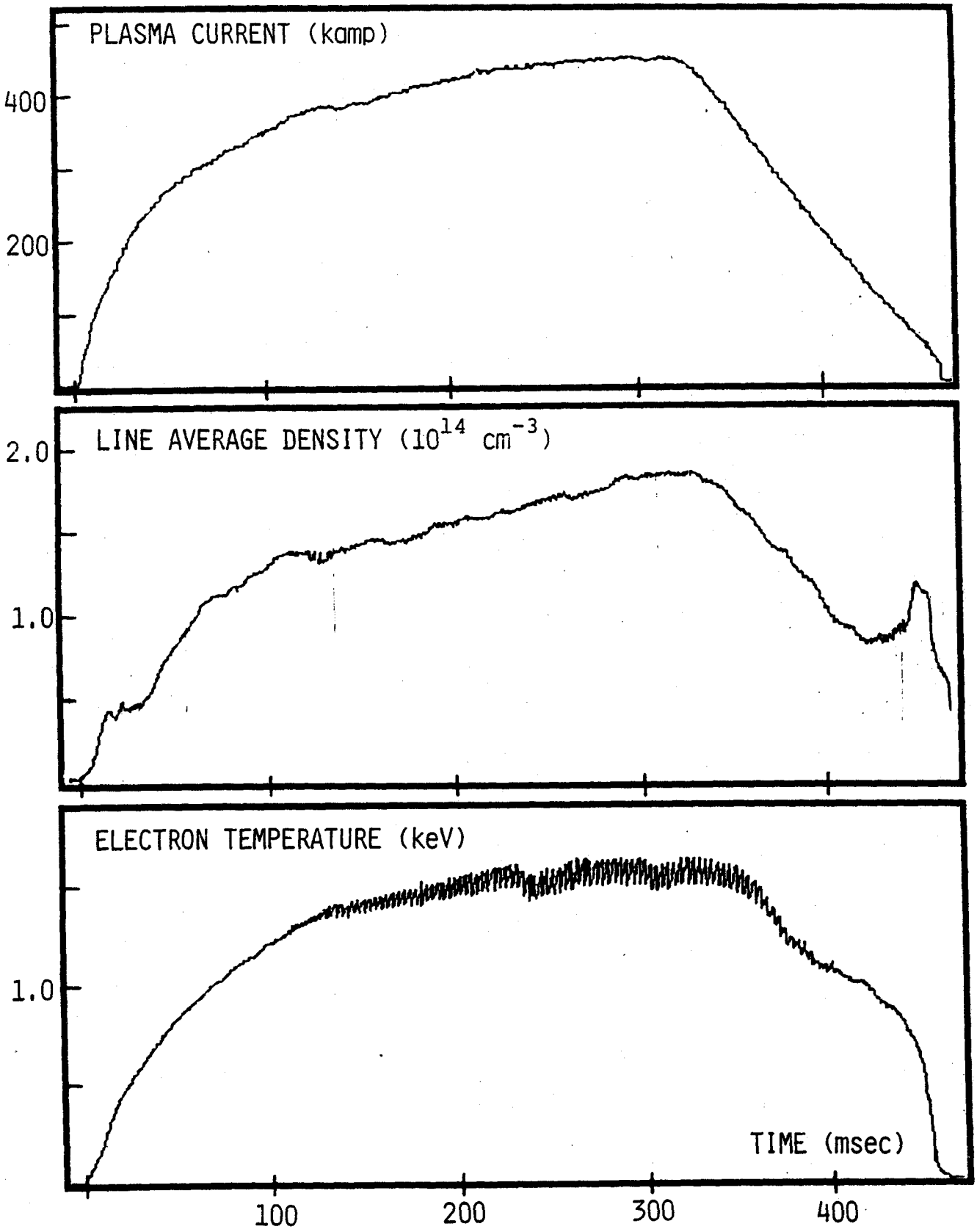

Fig.(2)

Typical time evolution of Alcator plasma discharge. Current is determined by measurement of magnetic flux, density by laser interferometry, temperature by central second gyroharmonic radiation. Fluctuations in temperature are caused by sawtooth instability.

SEC 1.0 REVIEW OF CYCLOTRON EMISSION

Electron cyclotron emission results from the centripetal acceleration of the charged particle in a static magnetic field. 'Synchrotron radiation' is a term connoting relativistic energies and is misleading when applied to a plasma with non-relativistic particle energies. Cyclotron emission by the plasma can be regarded as the superposition of numerous independently radiating electrons, although the effects of dispersion, absorption and other aspects of the Tokamak environment must be considered.

The submillimetre emission measured from typical Alcator discharges results entirely from cyclotron emission. Because of the larger magnetic fields encountered in Alcator, the emission occurs at higher frequencies but is otherwise similar to measured spectra from other Tokamaks.

SEC 1.1 SINGLE PARTICLE EMISSION

The exercise of computing the emission by a single electron in a magnetic field can be found in numerous textbooks[1,2], and consists of determining the radiation field arising from the current distribution of a gyrating electron. For the geometry of fig.(1) the emitted power from a single particle is:

EQ (1)
$$\frac{d^2P}{d\Omega d\omega} = \sum_{n=1}^{\infty} \frac{e^2\omega_n^2}{2\pi c} \left| \begin{array}{l} \underline{x}\ \cot\Theta\ (\cos\Theta - v_\parallel/c)\ J_n(\psi) \\ \underline{y}\ v_\perp/c\ J_n'(\psi) \\ \underline{z}\ (\cos\Theta - v_\parallel/c)\ J_n(\psi) \end{array} \right|^2$$

$$\psi = nv_\perp/c\ [1-(v_\parallel/c)\cos\Theta]^{-1}\sin\Theta\ ; \quad \omega_n = \frac{neB}{\gamma mc}\ [1-(v_\parallel/c)\cos\Theta]^{-1}$$

where the direction of the vector quantity being squared indicates the

polarisation of the electric field. Two noteworthy features are the radiation at harmonics of the gyrofrequency, and the disparity of emission intensity into the two distinct polarisations.

The frequencies of radiation are determined by the fourier harmonics of the periodic current distribution of the electron motion, giving rise to integrals of the form:

EQ (2) $$\int_{-\infty}^{+\infty} (\sin\omega_{ce}t)\, \exp(i\tfrac{v}{c}_{\perp} \sin\omega_{ce}t - \omega t)\, dt$$

which will be non-vanishing for integer multiples of the gyrofrequency, thus accounting for the radiation at the gyroharmonics. It is this type of integral which produces the Bessel functions in eq (1). The relative intensity of emission at subsequent harmonics is approximately:

EQ (3) $$\frac{I_n}{I_{n-1}} = [J_n(\psi)/J_{n-1}(\psi)]^2 = [\frac{\psi^2}{4n^2} + \cdots] \approx [\frac{v}{c}]^2$$

so that for a non-relativistic electron most of the emitted power occurs at the fundamental, or first gyrofrequency.

The observed radiation frequencies, as indicated in eq (1), depend upon the local magnetic field, and upon the energy and projected velocity of the emitting electron. For a single particle these quantities are constants, so emission will occur at harmonics of a narrow frequency, the width being determined by radiational broadening. The relativistic factor γ can decrease the emission frequency, but only for uncharacteristically energetic particles.

The two modes of propagation are called ordinary and extraordinary, and refer to the polarisation of the electric vector. Differing amounts of radiation are emitted into each mode. For example, the ratio of emission into the two modes of nearly perpendicular propagation at any harmonic frequency is approximately:

EQ (4) $$\frac{I_n(\underline{z})}{I_n(\underline{x})} = \frac{v_\perp^2}{v_\parallel^2}\left[\frac{J_n(\psi)}{J_n'(\psi)}\right]^2 \approx \left[\frac{1}{n}\frac{v}{c}\right]^2$$

so that a non-relativistic electron is expected to emit cyclotron radiation primarily into the extraordinary mode.

SEC 1.2 PLASMA EFFECTS

Electrons will radiate at harmonics of the gyrofrequency as determined by the local value of magnetic field. The toroidal field as a function of position is:

EQ (5) $$B(r) = \frac{B_0 R}{R+r}$$

where r is the radial position along the midplane measured from the geometric axis. A large spread in radiated frequencies will result from the spatial variation of the field. This spread is much larger than broadening produced by the Doppler or relativistic terms of eq (1). For example, at the second gyroharmonic the various broadening processes acting upon a typical Alcator plasma (B_T = 60 Kg $n_e = 10^{14}$ cm^{-3}, T_e = 1 KeV) will have the following effect: $\Delta\omega/2\omega_{ce}$ = collisional - 5×10^{-8}, relativistic - 6×10^{-4}, Doppler - $5\times10^{-2}\cos\Theta$, magnetic - 5×10^{-1}. For angles Θ within 1^o of perpendicular the relativistic broadening term exceeds the Doppler width, however, both

are small compared to the width produced by the magnetic field variation. Thus the frequency extent of radiation at any particular gyroharmonic will be determined by the variation of the toroidal magnetic field, this being the larger effect.

Because of limitations imposed by construction of the toroidal magnet, optical access to the plasma is restricted to directions perpendicular to the magnetic field, hence the observed radiation must be travelling in this direction. The two polarisation states will describe propagation perpendicular to the toroidal magnetic field. The ordinary mode is polarised with electric vector oriented along the field direction, while the extraordinary polarisation has its vector perpendicular to the field. The cold-plasma dispersion relation for these two modes of perpendicular propagation is shown in fig.(2). The ordinary mode is accessible to radiation with frequency above the plasma frequency, while the extraordinary mode has a region of non-propagation between the upper-hybrid and right-hand cutoff frequencies.

Due to the spatial variation of the plasma density and magnetic field, the dispersion relations for the two modes will have positional dependence. In particular the cutoff and resonance frequencies of each mode will change for each radial position. This is shown in fig.(3), where the critical frequencies are plotted as a function of radius for a typical plasma condition. Extraordinary radiation at the first harmonic propagating outward will encounter the upper-hybrid layer before the plasma edge, and will be absorbed or reflected. For this reason no extraordinary polarisation first harmonic emission is observed. This situation would not be expected if, for example, the

detection system was located at the inner plasma edge, a situation precluded by the design and construction of the Alcator tokamak. Ordinary mode first harmonic emission can be observed, provided that $\omega_{pe}/\omega_{ce} < 1$.

When harmonic cyclotron emission is considered in the context of a magnetoactive plasma a necessary consideration becomes that of radiation absorption by the plasma. For a sufficiently dense plasma this absorption will alter the emission produced by a collection of individual electrons to the extent that a single particle treatment is inadequate.

SEC 1.3 OPTICAL DEPTH

In a plasma, radiation at any frequency must travel from a point of emission to a point of observation along a path which may allow for absorption and reemission of radiation at the same frequency. The equation of radiation transfer describing this process of absorption and emission along the ray path is[3]:

EQ (6)
$$\frac{d}{ds}\left[\frac{dI(\omega)}{d\Omega}\right] = j_\omega - \alpha_\omega\left[\frac{dI(\omega)}{d\Omega}\right]$$

where j_ω is the volume emissivity and α_ω is the spectral absorptivity governing radiation at frequency ω. Both of these quantities are integrals of the total electron distribution function, and represent the combined behaviour of individual plasma electrons. The emission becomes:

EQ (7)
$$\frac{dI(\omega)}{d\Omega} = \frac{j_\omega}{\alpha_\omega}\left[1 - \exp\left(-\int_{\text{raypath}} \alpha_\omega\, ds\right)\right]$$

For a Maxwellian electron distribution Kirchhoff's law relates the emissivity and absorptivity[4]:

$$\text{EQ (8)} \qquad \frac{j_\omega}{\alpha_\omega} = I_{bb}(\omega) = \frac{\hbar\omega^3}{8\pi^3c^2}\left[\exp\frac{\hbar\omega}{kT} - 1\right]^{-1}$$

with the result that:

$$\text{EQ (9)} \qquad \frac{dI}{d\Omega} = I_{bb}\left[1 - e^{-\tau}\right] \; ; \quad \tau = \int_{\text{raypath}} \alpha_\omega ds$$

where I_{bb} (the temperature) remains constant across the resonance. Since the radiation quantum energies are small compared to the thermal plasma energy, $\hbar\omega \ll kT$, the blackbody formula can be expressed in the Rayleigh-Jeans limit, $I_{bb} = \omega^2 kT/8\pi^3c^2$.

The optical depth τ, is a measure of the degree to which absorption affects radiation transfer. If $\tau \ll 1$, absorption can be ignored and the plasma treated as a collection of independent radiators. For $\tau \gg 1$ the radiation will approach an equilibrium with the emitting electrons, so that its intensity will characterise the thermal properties of the plasma. If the optical depth is much greater than unity for a particular frequency, the emission intensity at that frequency approaches the blackbody level, provided that the electron distribution is near equilibrium. Furthermore, if the plasma is in thermal equilibrium, it cannot radiate more than the local blackbody level, I_{bb}.

Determination of τ by eq (9) requires integration of the absorptivity along the raypath for a particular frequency. The absorption is a local process provided that the scale length of the resonance between wave and electrons is small compared to variations

in electron density, or temperature, or magnetic field, and of course, that no overlap of harmonics occur. The scale length is determined by the magnetic field variation together with the appropriate resonance width:

EQ (10)
$$L = \Delta \omega_n \left[\frac{d\omega_n}{dr}\right]^{-1} = R\,(2\pi n)^{1/2}\left[\frac{T}{mc^2}\right]$$

where the relativistic width is used for the case of perpendicular propagation. It is seen that L is much smaller than typical gradients in the plasma. The optical depth is thus a local quantity, and can be thought of as the above scale length multiplied by the local absorptivity α_ω. The absorptivity can be found through the imaginary part of the refractive index[5], or from Kirchhoff's law and the emissivity. The optical depth for the n^{th} harmonic is[6]:

EQ (11)
$$\tau_n^x(r) = \frac{\pi}{2}\frac{R}{c}\,\frac{\omega_{pe}^2(r)\; n^{2n-2}}{\omega_{ce}(r)\;(n-1)!}\left[\frac{kT(r)}{2mc^2}\right]^{n-1} \quad ; \Theta = \frac{\pi}{2}$$

$$\tau_n^o(r) = 0.15\,\frac{kT(r)}{mc^2}\;\tau_n^x(r) \quad ; \Theta = \frac{\pi}{2}$$

for the low density, $\omega_p << \omega_c$, case in the mildly relativistic limit. In the $\omega_p \approx \omega_c$ limit eq (11) is a fair approximation for harmonics $n > 1$, but is not applicable to the first harmonic.

Absorption at the first gyroharmonic requires special treatment, particularly for the extraordinary polarisation. The reason for this is that while the ordinary mode is purely electromagnetic, the extraordinary mode has an electrostatic component elliptically polarised perpendicular to the magnetic field. It has been shown[7] that with rising density the electrostatic component produces a left-hand polarisation, instead of the right-hand case normally associated with the extraordinary mode. This decouples the wave from the electron gyrations and so reduces the absorption. For Alcator conditions the theory[8] predicts an optically thick ordinary, and thin extraordinary mode at the first harmonic. For the sake of completeness it is mentioned that measurements[9] in other devices indicate an optically thick extraordinary mode, this being attributed to a mode conversion of electrostatic (Bernstein) waves[10].

The concern in this thesis is primarily with the 2^{nd} and 3^{rd} harmonic extraordinary polarisation, for perpendicular propagation in the regime $\omega_p < \omega_c$. The contribution of plasma dielectric properties[11] to the absorption at higher harmonics results from relativistic $(v_{th}/c)^2$ and finite density (ω_p/ω_c) effects. It has been argued[12] that a relativistic treatment is necessary for the 2^{nd} harmonic, even at low (1 KeV) temperature, but not for higher harmonics.

The finite density effect for $\Theta = \pi/2$ has been calculated in the non-relativistic limit for harmonic n[13]:

$$\alpha_\omega{}^X = \alpha_\omega{}^X(\text{E.C.}) \left[\frac{\beta^2 n^2 - 1}{\beta n^2 - 1}\right]^{n-3/2} \left[1 + \frac{(1-\beta)n}{\beta n^2 - 1}\right]^2 \qquad \text{EQ (12)}$$

$$\beta = 1 - \left[\frac{\omega_p}{\omega}\right]^2$$

where α_ω^X(E.C.) refers to eq (11), the Englemann, Curatolo result. For a situation of interest, $\omega_p/\omega_c = .8$, eq (12) yields the following:

EQ (13) n=2: $\alpha_\omega^X = 1.13\ \alpha_\omega^X$(E.C.) n=3: $\alpha_\omega^X = .93\ \alpha_\omega^X$(E.C.)

The absorption is enhance slightly at the 2nd harmonic, and decreased slightly at the 3rd, over the values predicted in the low density limit. The small correction to α at the 2nd harmonic does not change the essential fact that $\tau >> 1$. It is noted here that nowhere in what follows is an explicit value of τ for the second harmonic required, only that τ be large. This requirement is satisfied when the finite density are included.

Since the blackbody level scales with the square of the radiated frequency, which in turn is a linear function of the magnetic field, high field devices such as Alcator can generate higher levels of cyclotron radiation. However, the radiated power from Alcator due to cyclotron emission is inconsequential compared to other power loss mechanisms, and to the ohmic input power.

SEC 1.4 REFLECTIONS & POLARISATION

Fig.(4) shows representative submillimetre spectra of the two polarisations from a tokamak discharge, as measured with the Michelson interferometer system. Emission is recorded at the frequencies corresponding to the first three gyroharmonics, the width of each harmonic feature being determined primarily by the magnetic field variation across the plasma. As expected, emission intensities at the optically thick frequencies are limited to the blackbody level, while

intensities at higher frequencies are below this level. No first harmonic extraordinary radiation is detected, in accordance with the predicted absorption at the upper-hybrid layer. However, cursory examination shows that the intensities of emission into the two polarisations are not in the ratios predicted by the single particle description. This is particularly true at the third harmonic where the optical depth is less than unity for both modes, so that the ratio of intensity should be nearly approximated by eq (4).

The presently accepted explanation for observed ordinary mode emission at the second and third gyroharmonics requires the reflection of extraordinary mode radiation from the vacuum chamber wherein the reflected wave undergoes a change in polarisation, thus appearing to the observer as if emitted with the ordinary polarisation. Given the irregular internal construction of tokamaks such a hypothesis is not unreasonable. The relative polarisation of the second harmonic, 5:2, shown in fig.(4) is the largest value obtainable from Alcator, and is consistent with measurements from other tokamaks[14] and with the polarisation scrambling model[15,16]. According to this model, the total intensity of every reflected ray is some fraction r of the incident ray, where $r < 1$, and some portion p of the reflected ray has changed polarisation state. The polarisation ratio then becomes:

EQ (14)
$$\frac{I_O}{I_X} = \frac{p}{1+p-r}$$

Furthermore it follows that the extraordinary mode intensity is:

EQ (15)
$$I_X = \frac{1 - e^{-\tau}}{1 - \rho e^{-\tau}} \qquad \rho = r - p\left[1 - \frac{I_O}{I_X}\right]$$

For the stated polarisation ratio, and $\rho = .5$ as measured from 3rd harmonic emission [sec (4.1)] eqs (14),(15) are satisfied with $p = .24$ and $r = .64$. For Alcator A[17] this same treatment produced $p = .15$ and $r = .85$. The errors in the measurements are such that the two sets of values are considered approximately equal. The two machines have similar internal construction, so that comparable results are expected.

The presence of reflections does not disallow ignoring the doppler spread of frequencies for optically thick frequencies. The reason being that any reflected radiation must recross, and be absorbed by, the optically thick layer, and hence cannot be observed from the outside. For this reason the doppler broadening effect is ignorable.

SEC 1.5 TEMPERATURE PROFILE

For the optically thick second harmonic extraordinary mode, the spectral width is governed by the magnetic field spatial variation, with intensity at each frequency proportional to the corresponding blackbody level. A conversion of frequency to spatial position can be made by use of the magnetic field, eq (5)[18]. The blackbody level at a particular frequency can be associated with the temperature at the equivalent radial location within the plasma, this being done with eq (9). In this fashion spatial electron temperature profiles can be mapped[19]. It is only required that radiation from an optically thick frequency be used. From fig.(3) it is seen that the first harmonic ordinary and second harmonic extraordinary mode are candidates for this treatment. The second harmonic is preferred since it will have

the higher intensity, thus a better signal to noise ratio. Furthermore, emission at the first harmonic can be cutoff for sufficient plasma densities. Fig.(5) shows the case where rising plasma density during a discharge causes the plasma frequency to encroach upon the first harmonic, with the resulting attenuation of first harmonic emission.

Electrons of relativistic energy can broaden the frequency spectrum through the mass term and the doppler shift. These effects will spread the region of emission beyond the frequency domain set by the magnetic field variation. The resulting spectra will eventually become a continuum, with no distinguishable harmonic structure[20]. An example broadband spectrum is shown in fig.(6) for extraordinary mode emission. The low frequency cutoff results from the non-propagation band of the extraordinary mode. The additional feature near the plasma frequency is discussed in sec(8). A depression of the continuous spectrum in the vicinity of the 2^{nd} harmonic, apparent in fig.(6), results from absorption by the thermal electrons.

Electrons with $\gamma > 1$ will emit radiation at the same frequency as thermal electrons in a lower magnetic field. Because of the field gradient this thermal layer will always be between the point of emission and the observation point. Doppler broadened radiation from relativistic electrons must be scattered from the back wall of the vacuum chamber in order to be observed since it is not emitted perpendicular to the field. After reflection it must traverse the entire plasma cross section, being subject to absorption by any optically thick layers. Cyclotron radiation by relativistic electrons will be absorbed at the thermal layer, and the observed radiation will

be characterised by the temperature of this layer. Thus in fig.(6) the broadband emission in the frequency range of the optically thick 2nd harmonic is absorbed to the thermal level with the measured radiation corresponding to a temperature of 850 eV. It has been suggested that cyclotron emission by relativistic electrons will modify the intensity of the optically thick harmonic, and so perturb the profile. However, from the previous argument and example, it is seen that such emission will be absorbed to the appropriate thermal level.

SEC 1.6 REFERENCES & FIGURES

1.) J. D. Jackson Classical Electrodynamics
Wiley & Sons, New York (1962)

2.) W.K.H. Panofsky, M. Phillips Classical Electricity
& Magnetism Addison Wesley, Reading Mass. (1962)

3.) G. Bekefi Radiation Processes in Plasmas
Wiley & Sons, New York (1966)

4.) The integral over k-space will introduce a factor of $1/n^2$ i.e. $k^2 = \omega^2/n^2c^2$. This will be canceled by a similar term which accounts for the change in solid angle of the ray as it passes through the refractive medium.

5.) M. Bornatici, F. Engelmann, G.G. Lister
Phys. Fluids 22 1664 (1979)

6.) F. Engelmann, M. Curatolo
Nuclear Fusion 13 497 (1973)

7.) M. Bornatici, F. Engelmann
Comments Plasma Phys. Cont. Fusion 4 139 (1979)

8.) Y. Dnestrovskii, D.P. Kostomarov, N.V. Skrydlov
Zh. Tekh. Fiz. 33 922 (1962)

9.) A.E. Costley, T.F.R. Group
Phys. Rev. Lett. 38 1477 (1977)

10.) J. Hosea, V. Arunasalam, R. Cano
Phys. Rev. Lett. 39 408 (1977)

11.) C.M. Celata, D.A. Boyd
Nuclear Fusion 19 423 (1979)

12.) I.P. Shkarofsky
Phys. Fluids 9 561 (1966)

13.) K. Audenaerde
Plasma Physics 19 299 (1977)

14.) F. Stauffer Private Communication

15.) A.E.Costley, R.J.Hastie, J.W.M. Paul, J. Chamberlain
Phys. Rev. Letters 33 758 (1974)

16.) I.H. Hutchinson
Plasma Physics 21 1043 (1979)

17.) I.H. Hutchinson, D.S. Komm
Nuclear Fusion 17 1077 (1977)

18.) It is assumed that no overlap of harmonic frequencies occurs, so that any point in space can be resonant with only one harmonic at one particular frequency.

19.) R. Cano et.al.
Nuclear Fusion 19 1415 (1979)

20.) C.M. Celata, D.A. Boyd
Nuclear Fusion 17 735 (1977)

GEOMETRY OF CYCLOTRON EMISSION

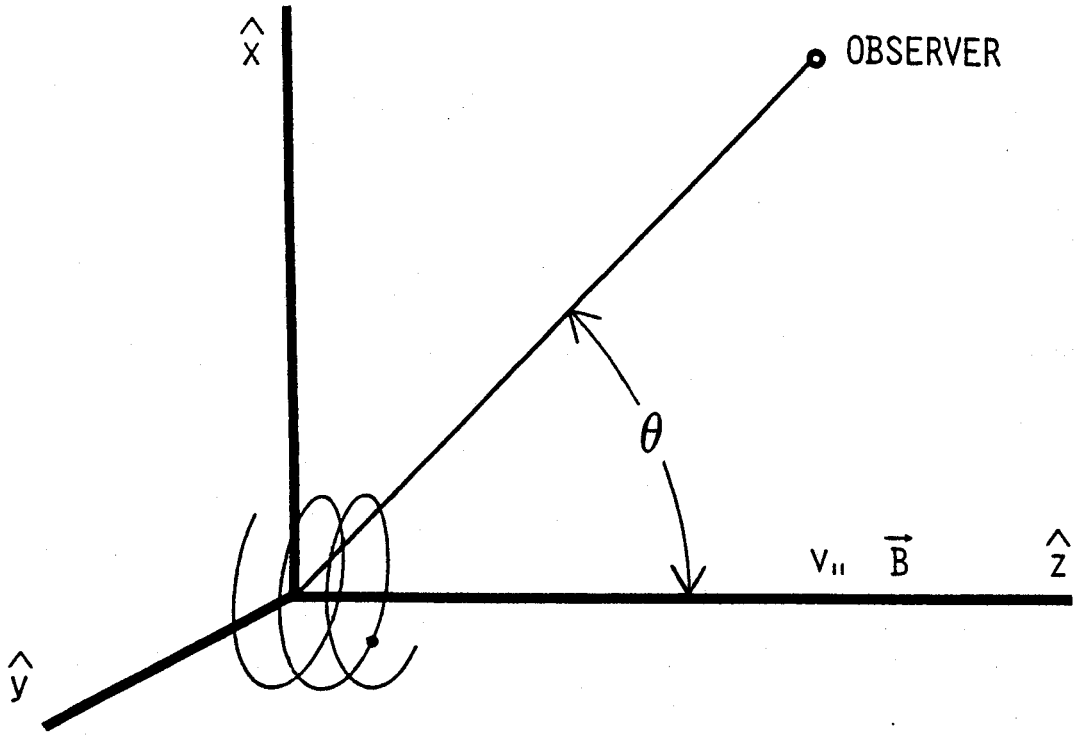

$$\underline{r} = \hat{x}\left[\frac{v_{\perp}}{\omega_o} \sin\omega_o t\right] - \hat{y}\left[\frac{v_{\perp}}{\omega_o} \cos\omega_o t\right] + v_{\parallel} t\,\hat{z}$$

ELECTRON GYROFREQUENCY $$\omega_o = \frac{-e\,B}{\gamma mc}$$

Fig.(1)
Radiation is observed perpendicular to the magnetic field; that is, along the x axis. The radiation from a single particle will be symmetric with respect to rotation about the z axis. γ is the relativistic factor. $\gamma = 1$ for thermal plasmas.

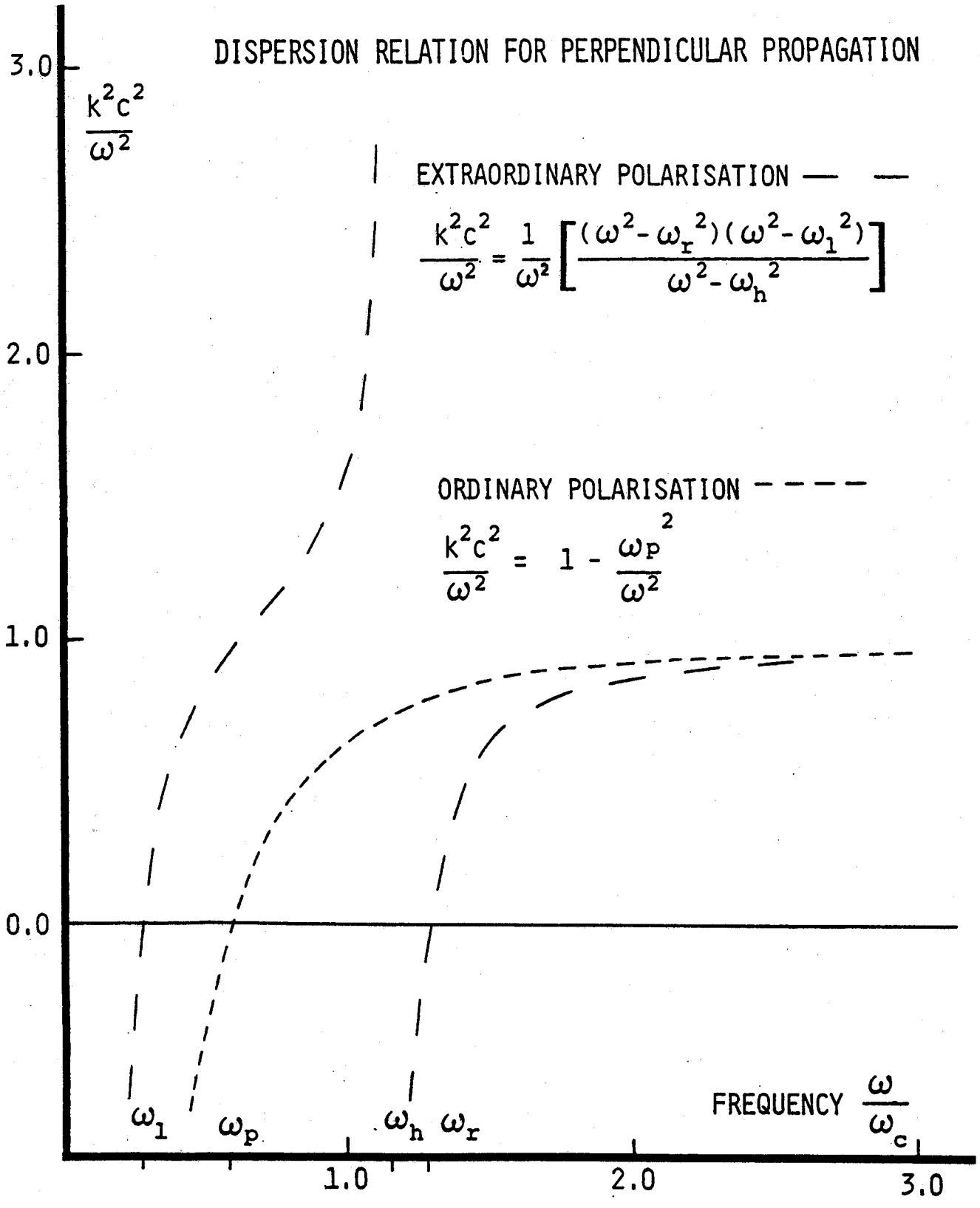

Fig.(2)
Cold plasma dispersion for $\omega_{pe}/\omega_{ce} = .57$ Low frequency branches are not shown.

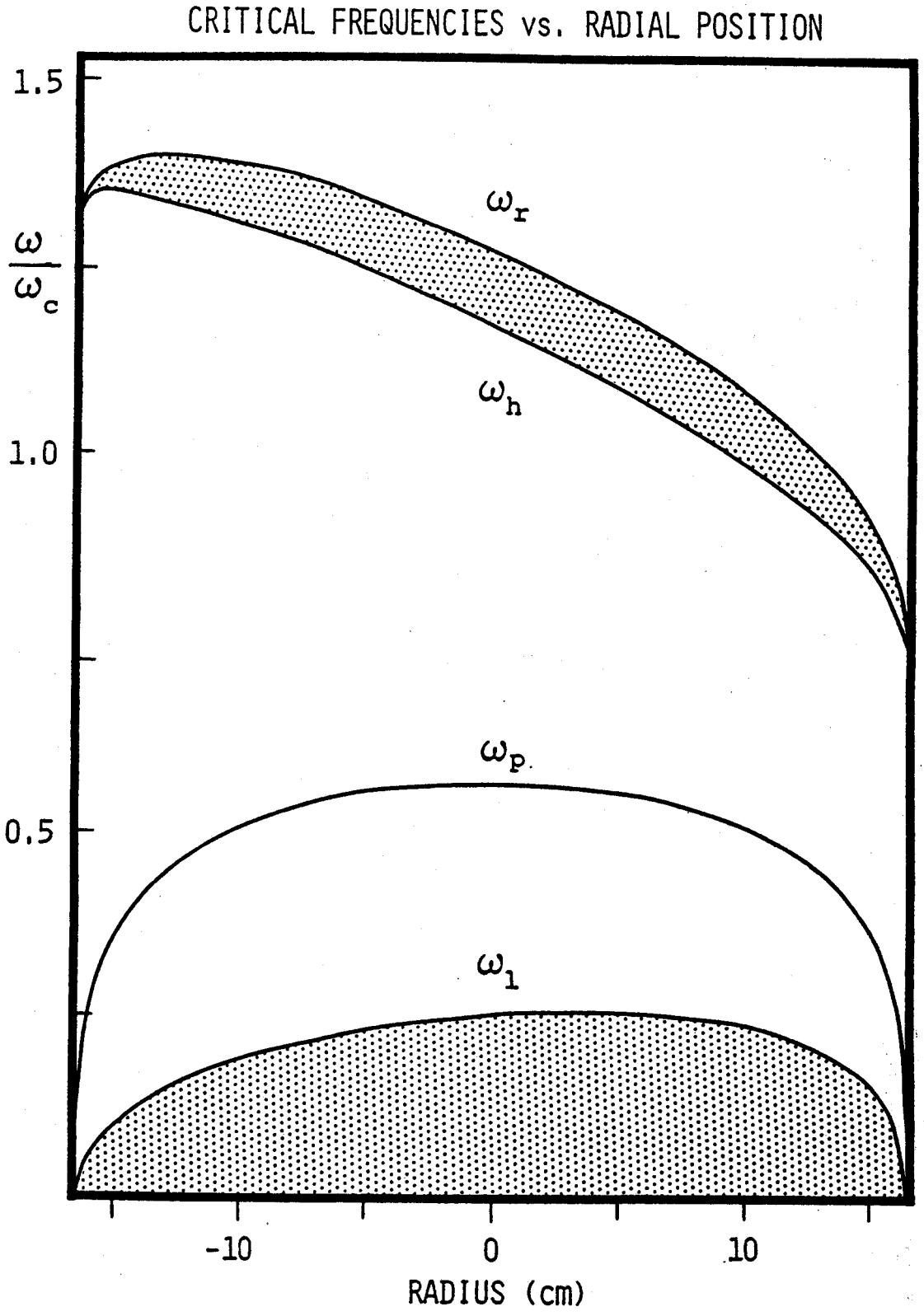

Fig.(3)
For ω_{pe}/ω_{ce} = .57 . Shaded areas are regions of non-propagation for the extraordinary mode. Ordinary mode does not propagate below the wpe curve. Radiation moves from left to right, where it is observed on the outside (low field) side of the Tokamak.

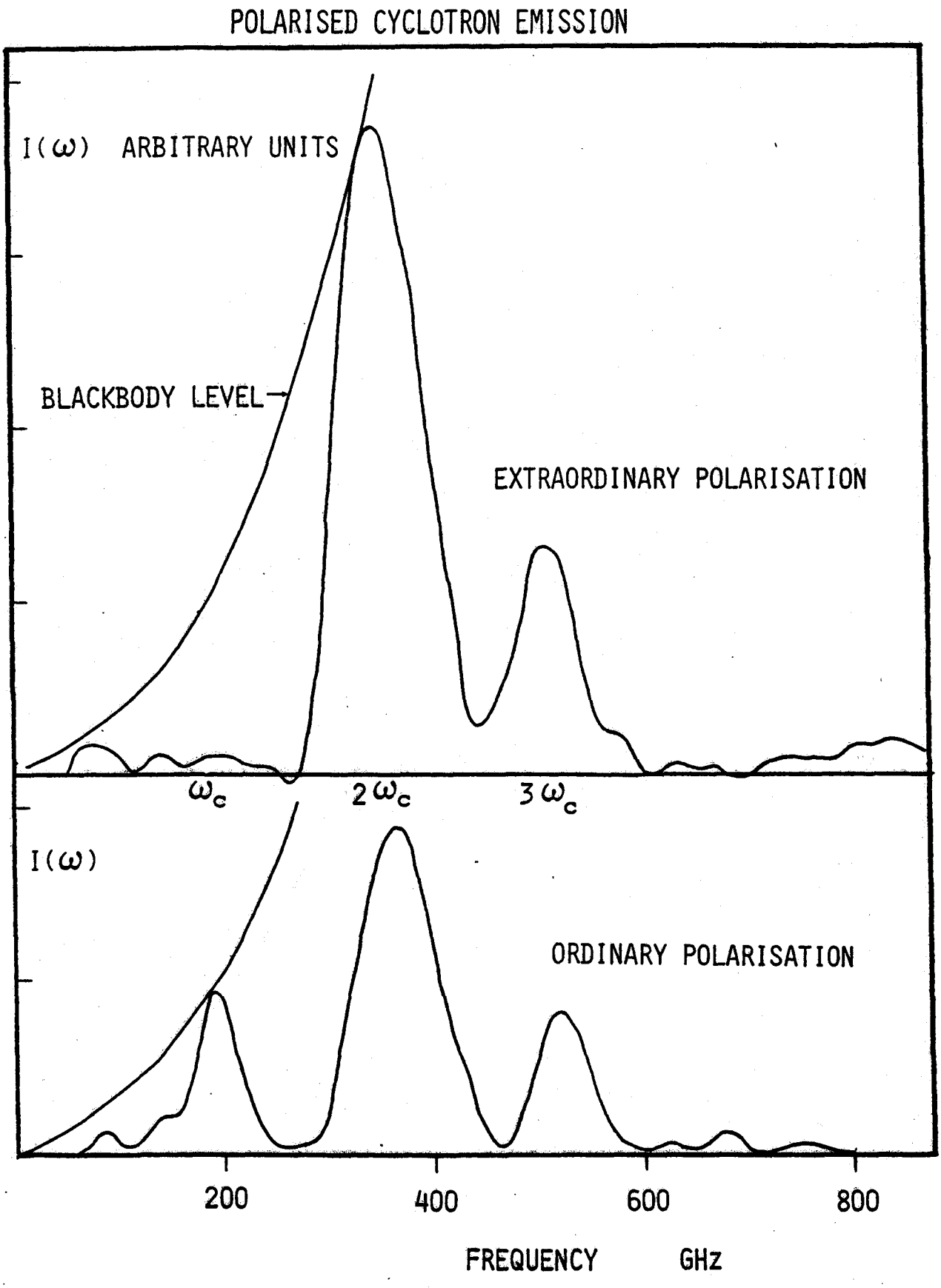

Fig.(4)
Ordinary and extraordinary mode emission from Hydrogen plasma in 60 kGauss magnetic field. Both spectra are plotted on same scale.

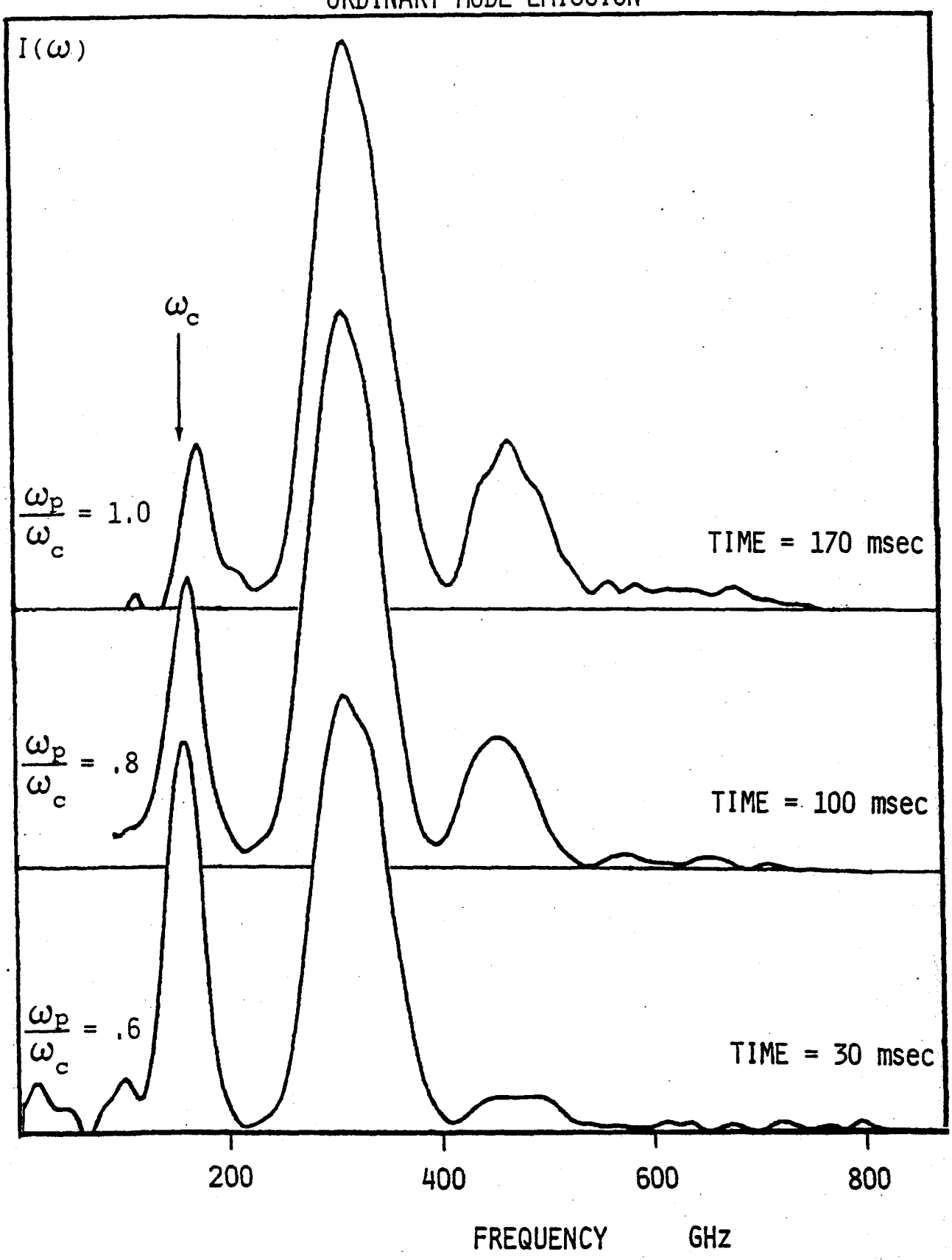

Fig.(5)

The situation $\omega_{pe} = \omega_{ce}$ is rarely encountered in Alcator C because the plasma disrupts. This case for 60 kGauss. All

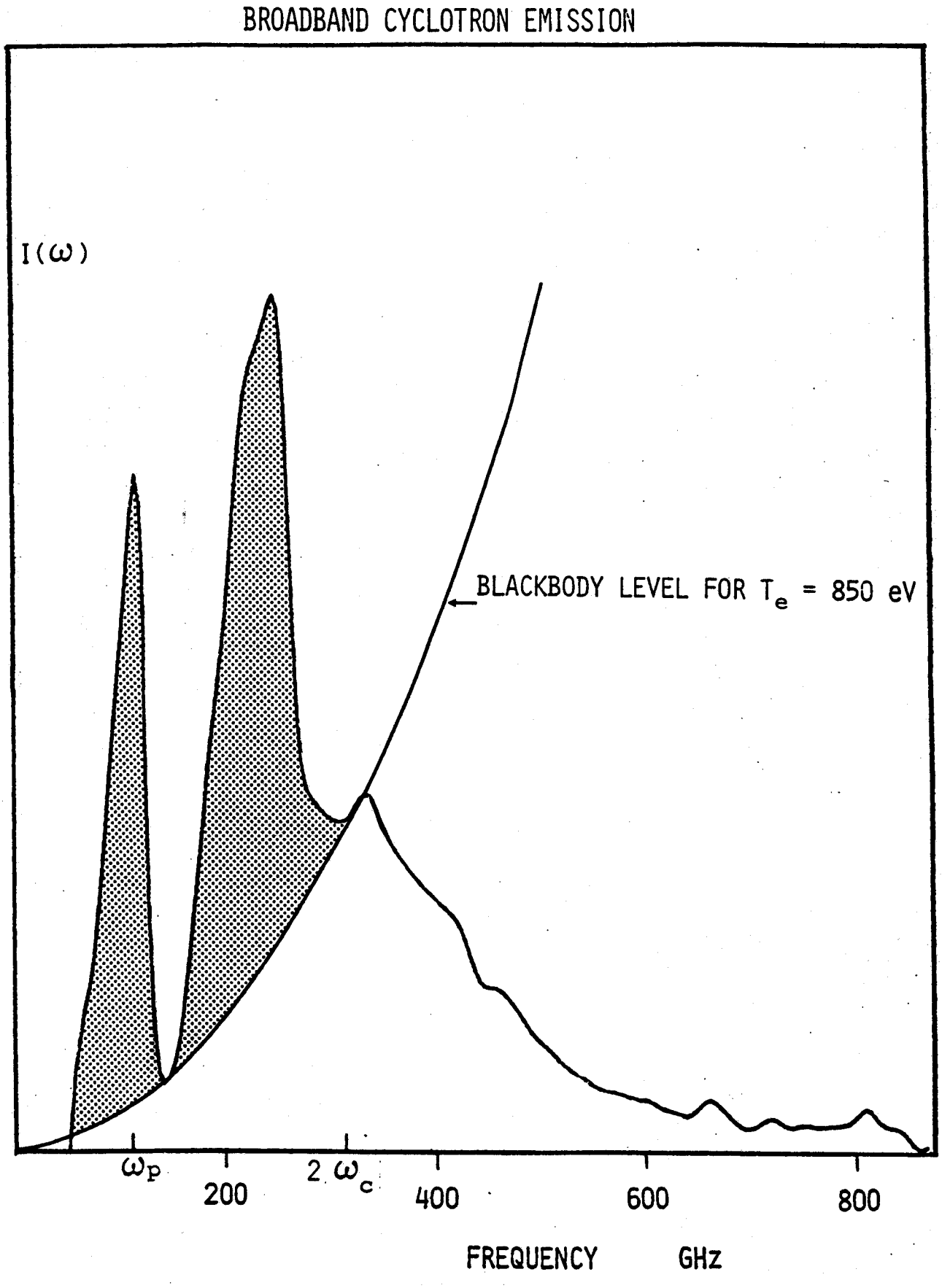

Fig.(6)
The shaded region is emission above the thermal level. The feature at ω_{pe} is discussed in sec (6). The dip at 130 GHz corresponds to absorption at the hybrid layer, this being an extraordinary mode spectrum for 60 kGauss field.

SEC 2.0 ELECTRON TEMPERATURE PROFILES

The electron temperature profiles inferred from extraordinary mode emission at twice the electron cyclotron frequency have nearly a Gaussian shape under normal circumstances. The central temperature thus measured is found to equal the predicted value based upon classical resistivity as determined by the measured voltage and spectroscopic Z_{eff}. The profile width is also in agreement with this model, and along with the central temperature indicate values of $q_o = .85$. Relative changes of the position of the profile centre agree with changes in the outer flux surface position measured during plasma positioning experiments, while the absolute value of the profile centre provides an accurate measure of the toroidal magnetic field.

SEC 2.1 GAUSSIAN PROFILE

The optical depth of the second harmonic extraordinary polarisation from the Alcator Tokamak is[1]:

EQ (1)
$$\tau = \frac{23.8\ n(10^{14}cm^{-3})\ T(KeV)}{B(Tesla)}$$

Under normal operating conditions of density and temperature, $\tau > 1$ applies over most of the plasma cross section, so that emission from any position will be at or near the blackbody level. After dividing by the square of the frequency according to eq (1.8), the second harmonic spectral feature is converted to a spatial temperature by application of eq (1.5) which converts frequency to position. The accuracy of the temperature profiles derived in this fashion is

discussed in the appendix.

The measured temperature profile can be fit to a Gaussian:

EQ (2) $$T(r) = T_o \exp\left[\frac{r - r_o}{a}\right]^2$$

where T_o, r_o, a refer to the central temperature, position and width. The choice of a Gaussian is arbitrary; a number of other analytic expressions could be used. Favourable features of the Gaussian include easy integration and the direct correspondence of the width parameter, a, with the perceived profile width. Its major drawback is its infinite extent, which fortunately introduces only small errors.

A temperature profile and corresponding fit are shown in fig.(1). The three free parameters of the Gaussian are adjusted to minimise a weighted mean square deviation. The weighting favours the region of peaked temperature and ignores the edges where the emitting layers are not expected to be optically thick. A common feature of most Alcator profiles is the slight increase towards the inside (high frequency) edge which results from an overlap of the second and third harmonics. For this reason too the edge points are not included in a fit.

SEC 2.2 COMPARISON TO CLASSICAL RESISTIVITY

Classical resistivity results from a treatment where coulomb collisions between two charged particles are the only interactions considered. Anomalous resistivity then is any deviation due to additional processes such as non-collisional phenomena or collective effects in the plasma, eg. scattering from waves. The classical

resistivity calculated by Spitzer[2] for a pure hydrogen plasma will be the basis for comparison, with any deviations contained in the ratio η/η^*. With this definition the plasma resistivity is:

EQ (3) $$\eta = 5.22 \times 10^{-3} \ln\Lambda \, T^{-3/2}(eV)[\eta/\eta^*] \quad \text{(ohm-cm)}$$

For an ohmic-heated plasma the local resistivity is determined by the ratio of the local electric field and current density. The central current density is related to the toroidal magnetic field by q_o:

EQ (4) $$J_o = \frac{2\,B}{\mu_o q_o R} \quad \text{(MKS)}$$

The presence of sawtooth oscillations indicates $q_o < 1$ which then determines the central current density[3]. The central electric field is established by assuming the measured edge loop voltage is constant across the plasma cross section, and by sampling data during periods of constant current so that inductive effects can be ignored. With these assumptions the resistive voltage and central temperature are related:

EQ (5) $$V\,T(eV)^{3/2} = 522 \ln\Lambda \frac{B}{q_o}\frac{\eta}{\eta^*} \quad \text{(MKS)}$$

The relation between the measured central temperature and resistive voltage is shown in fig.(2). The data spans the available range of the two parameters. Curves representing eq (5) are indicated. For temperatures less than 2 KeV the data are consistent with $\eta/\eta^* = 1.5$. However, above this temperature a marked discrepancy occurs. In fig.(3) the ratio of measured to predicted temperature is plotted versus density for the same discharges shown in fig.(2). The deviation from predictions based upon eq (5) occurs at lower densities as well as higher temperatures. Because these conditions favour the production of runaway electrons, and because of known distortions of the electron distribution which may occur under these conditions[4], figs.(2) and (3) suggest the involvement of some related process. For example, the presence of non-thermal electrons could enhance the cyclotron emission creating the false impression of a higher temperature, or it might be argued that a large anomalous resistivity appears at lower densities as a result of runaway driven collective modes[5]. However, the observed deviations can be explained by the enhanced impurity levels encountered during low density operation.

The presence of impurities in the plasma will increase the observed resistivity over the predicted value which is based on $Z_{eff} = 1$. This increase can be absorbed into the factor η/η^*, which is approximated by the analytic expression[6]:

EQ (6)
$$\frac{\eta}{\eta^*} = \frac{.914 \times Z_{eff}}{1.077 + Z_{eff}} + .58 \times Z_{eff}$$

The Z_{eff} is measured with continuum bremsstrahlung emission in the visible[7] and a prediction of η/η^* is made according to eq (6). A

measured value of η/η^* is obtained from the electron temperature and eq (3). A constant coulomb logarithm is used for all data, since the variations which would be produced by changing density and temperature are smaller than the intrinsic inaccuracy inherent in the approximations used to generate the logarithm to begin with.

In fig.(4) the two values of η/η^* are plotted versus one another for the same data shown in figs.(2) and (3). The agreement is reasonable considering the inherent errors in the component parameters. The measured central temperature and voltage are consistent with the classical predictions provided that the effect of impurities is consisdered. It is not necessary to include any anomalous effect in order to explain the relation between the measured electron temperatures and voltage.

It would seem then that knowledge of Z_{eff} and the loop voltage would render superfluous independent measure of electron temperature in well behaved ohmic-heated plasmas. Unfortunately these two measurements, Z_{eff} and loop voltage, are not easily made with accuracy. The loop voltage measurement is susceptible to errors introduced by changing currents in the plasma and in external coils. These inductive effects can be partially discounted if measurements are made during periods of relative steady state operation. A further complication results from the measurement being made at the plasma edge, rather than the centre. The Z_{eff} determined by continuum bremsstrahlung will depend upon an absolute intensity calibration and furthermore is a chord average measurement, so that the central value of Z_{eff} will require an inversion of several chordal measurements. These factors contribute to an overall systematic uncertainty which

does not effect the relative precision of measurements corresponding to subsequent discharges, for example, but may influence the absolute accuracy of both by the same amount.

SEC 2.3 PROFILE WIDTH

If the voltage is constant across the plasma cross section then the assumption of classical resistivity combined with the temperature profile determines the current density:

EQ (7) $$J(r) = J_o \exp \frac{-3}{2}\left[\frac{r - r_o}{a}\right]^2$$

Integration of this expression yields a quantity which should equal the total plasma current:

EQ (8) $$I = J_o \frac{2}{3}\pi a^2$$

If the central current density is fixed by sawtooth oscillations the profile width can be written:

EQ (9) $$a^2 = \frac{3}{2}\frac{q_o}{q_{lim}} r_{lim}^2$$

where r_{lim} is the limiter radius and the value of q at the limiter is determined by the plasma current and the toroidal magnetic field:

EQ (10) $$q_{lim} = \frac{2\pi B r_{lim}^2}{\mu_o I R} \qquad \text{(MKS)}$$

Because the Gaussian profile does not become zero near the limiter radius as a real profile must, this treatment will be in error by :

EQ (11) $$\exp \frac{-3\ r^2}{2\ a^2}\Big|_{im} \approx 2\%$$

Fig.(5) is a plot of the profile width versus the limiter q calculated from eq (10). The data are an average of a large number of discharges, all having sawteeth. A least square fit of a power law to the data agrees with eq (9) and indicates $q_o = .85$. This same value of q_o was used in conjunction with the previous discussion of central temperature scaling with classical resistivity. It should be noted that the q_o inferred here is not a measure of the central current density. It is a number which works best within the framework of the applied models. To date no direct measurement of q_o, or of the current distribution has been made, so that a comparison with the inferred q_o is impossible.

A good bit of scatter is present in the data of fig.(5) which because of averaging is not apparent. If the data are divided into extremes of temperature most of this scatter vanishes. This is shown in fig.(6), where the data of fig.(5) is replotted to include only the temperature extremes. The obvious separation of data does not occur if the data are sorted by density, current, or magnetic field. If this difference resulted from an unequal averaging over several sawtooth periods the variation would be noticed during a single discharge, which is not the case. It is unclear whether the difference results from an actual effect in the plasma or is the manifestation of the fourier transform that generates the profiles. Measurements of sawteeth, sec (5), indicate that q_o is relatively constant, so it seems unlikely that some discharges have a higher current density on axis. The difference may be explained by allowing

an accumulation of impurities on axis, thus producing a local increase in Z_{eff}. The increased resistivity on axis would then produce a higher temperature for the same current density. This explanation can neither be confirmed or disproved with the existing data.

SEC 2.4 PROFILE CENTRE

The central position inferred from the Gaussian fit depends upon the toroidal magnetic field value used. This value is not measured directly, but is arrived at indirectly through an inherently inexact measurement of the magnet current. Substantial errors have resulted from this technique. Other possible influences upon the magnetic field such as the ripple produced by the toroidal asymmetry produced by diagnostic ports and current penetration times in the magnet have been ignored since they are unmeasured quantities and are expected to be small. There is nothing in the data which suggests that these effects should be included.

The cyclotron emission spectrum provides the only independent direct measure of magnetic field. Given that the field is constant for a series of discharges, relative changes in profile positions reflect actual plasma motion. When compared with position measurements made with magnetic pickup loops[8], fig.(7), the two techniques reflect the same relative change in position. Since the magnetic loops are sensitive to the outer flux surfaces, while the profile fit is governed by the plasma centre, the agreement in fig.(7) indicates motion of the entire plasma cross section in response to various applied vertical control fields. Fig.(7) indicates the agreement of the relative change in position, and should not be

interpretted as measuring an absolute shift of the centre with respect to the outer flux surface. Although such a shift, approximately 1 cm outward, is expected due to toroidal effects, the observed 'shift' is just as likely due to a systematic overestimation of the magnetic field.

If, based upon evidence from the pickup loops or the soft x-ray array, the temperature profile is assumed to be centered, then the magnetic field is determined by the frequency at which the 2^{nd} harmonic profile has a maximum. If this value disagrees with the field determined by the magnet current measurements, a recalibration of the current will bring the two techniques into agreement.

SEC 2.5 REFERENCES & FIGURES

1.) Engelmann & Curatolo

2.) L. Spitzer Physics of Fully Ionized Gases
Wiley & Sons, New York (1962)

3.) S. vonGoeler, W. Stodiek, N. Sauthoff
Phys. Rev. Letters 33 1201 (1974)

4.) J. Rice Ph.D. Thesis MIT (1979)

5.) O. Buneman
Phys. Rev. 115 503 (1959)

6.) W.M. Stacey Jr. Fusion Plasma Analysis
Wiley & Sons, New York (1981) p. 264

7.) E.S. Marmar
To be published Rev. Sci. Instrument

8.) P. Pribyl S.M. Thesis MIT (1981)
also PFC/RR-81-21

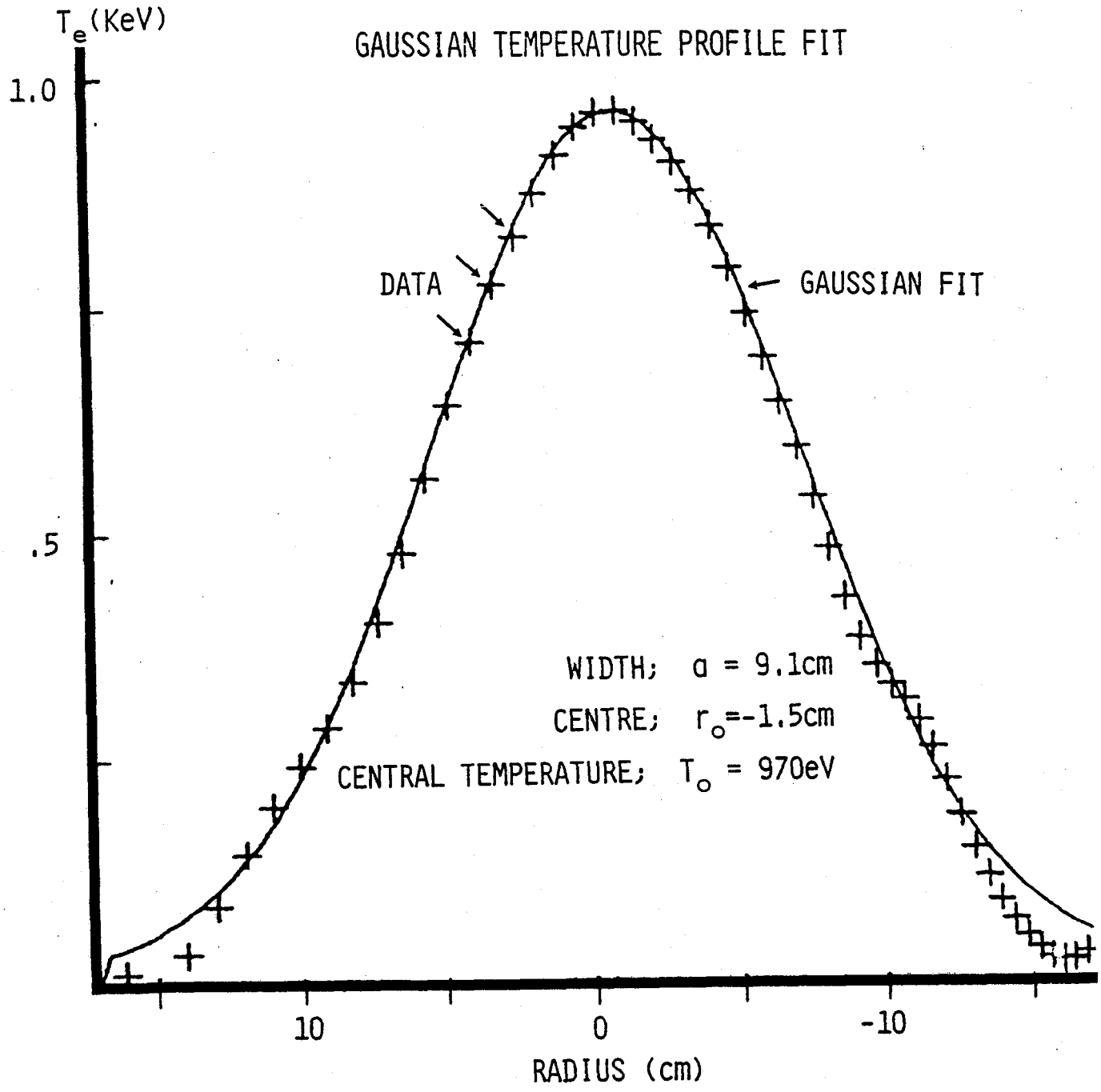

Fig.(1)
Electron temperature profile with fit. From steady state portion of Hydrogen discharge: 60 kGauss, density = 2.5×10^{14} cm^{-3} line average.

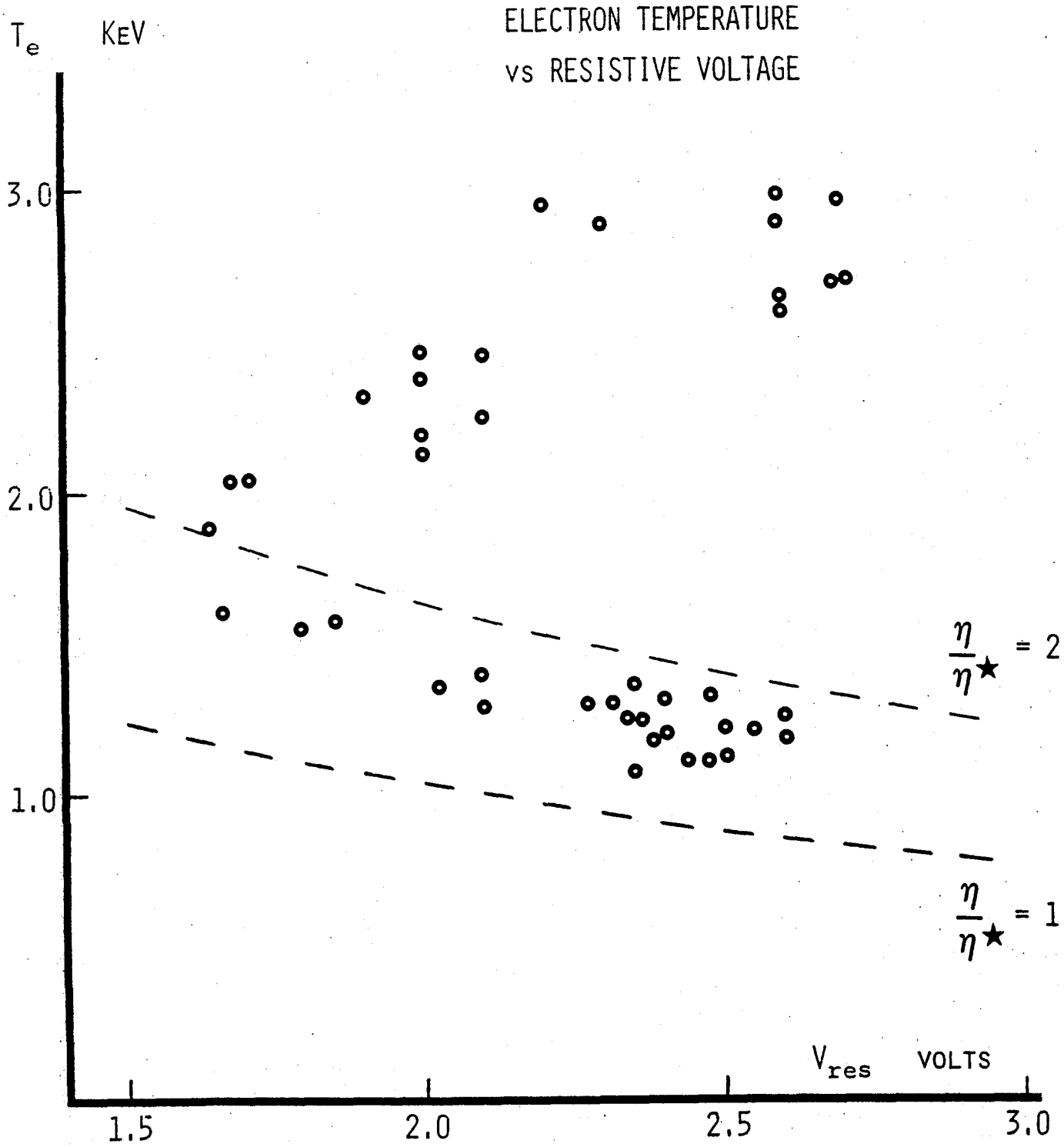

Fig.(2)
Resistive voltage incorporates inductive corrections. These data from steady state portions of sawtoothing hydrogen discharges in 80 kGauss magnetic field.

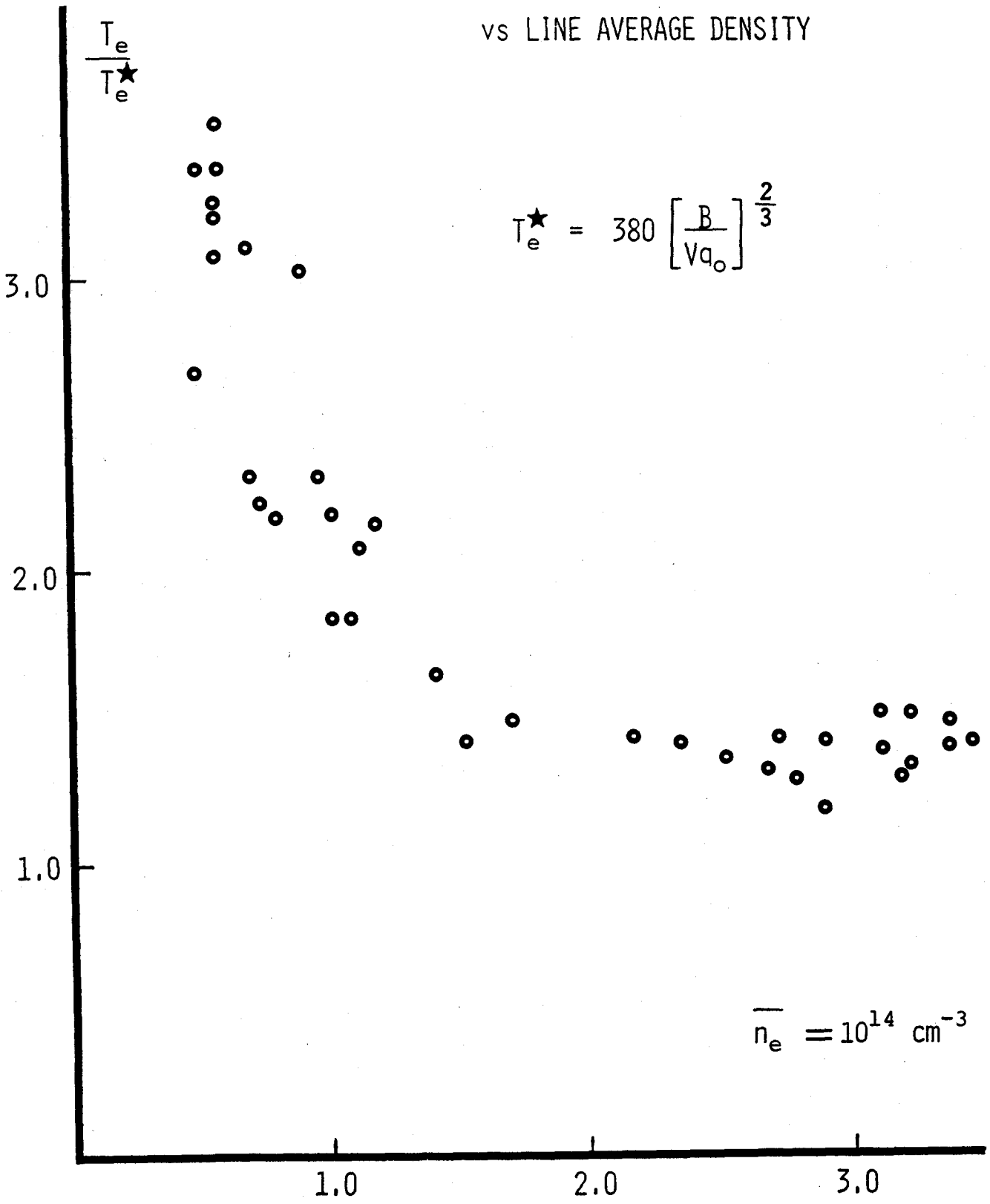

Fig.(3)
These data correspond to the same discharges as the previous figure. The predicted temperature T_e^* supposes $n/n^* = 1$.

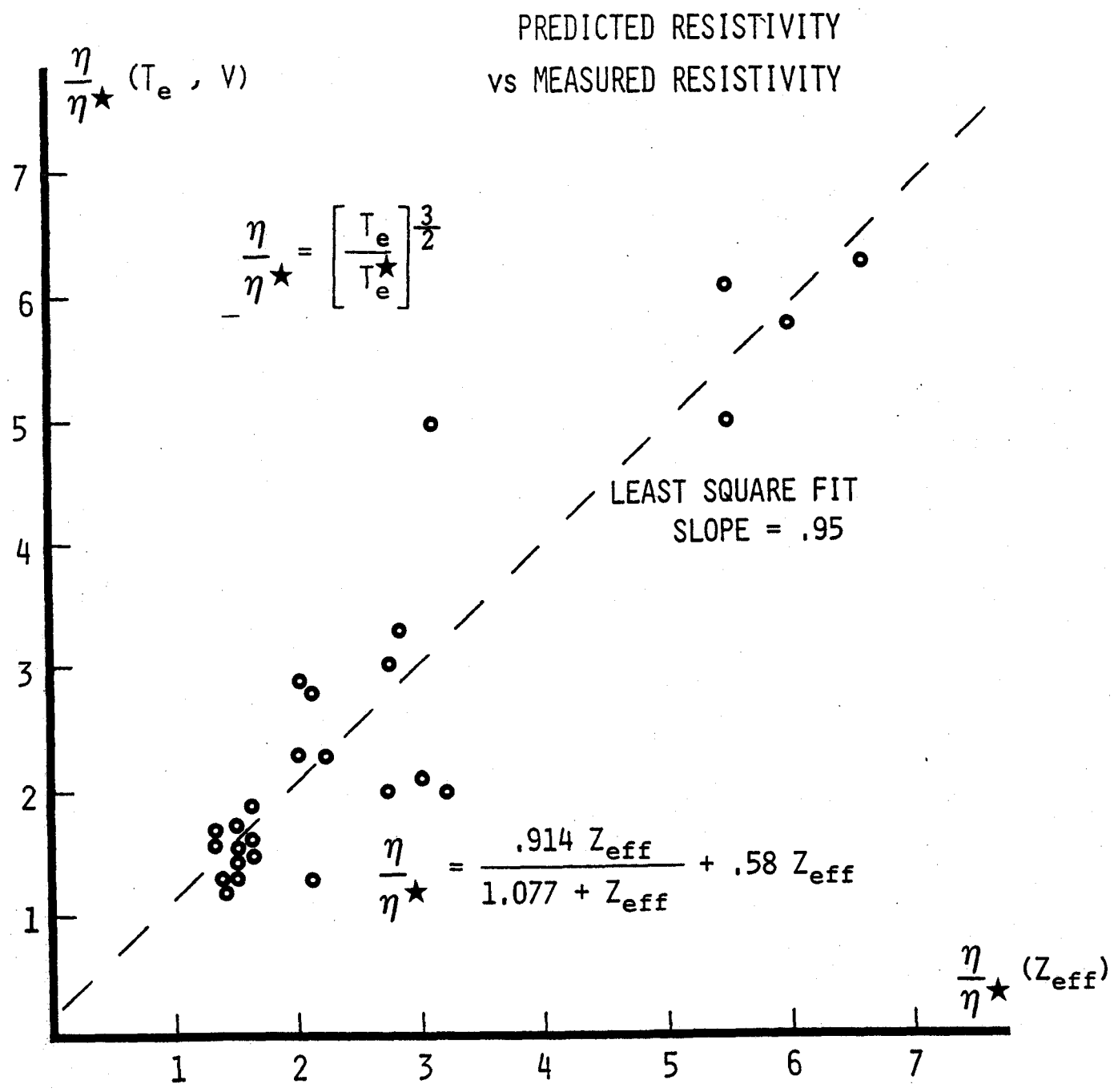

Fig.(4)

These data correspond to the previous two figures where measured Z_{eff} are available. The primary contribution to Z_{eff} comes from partially ionised Molybdenum.

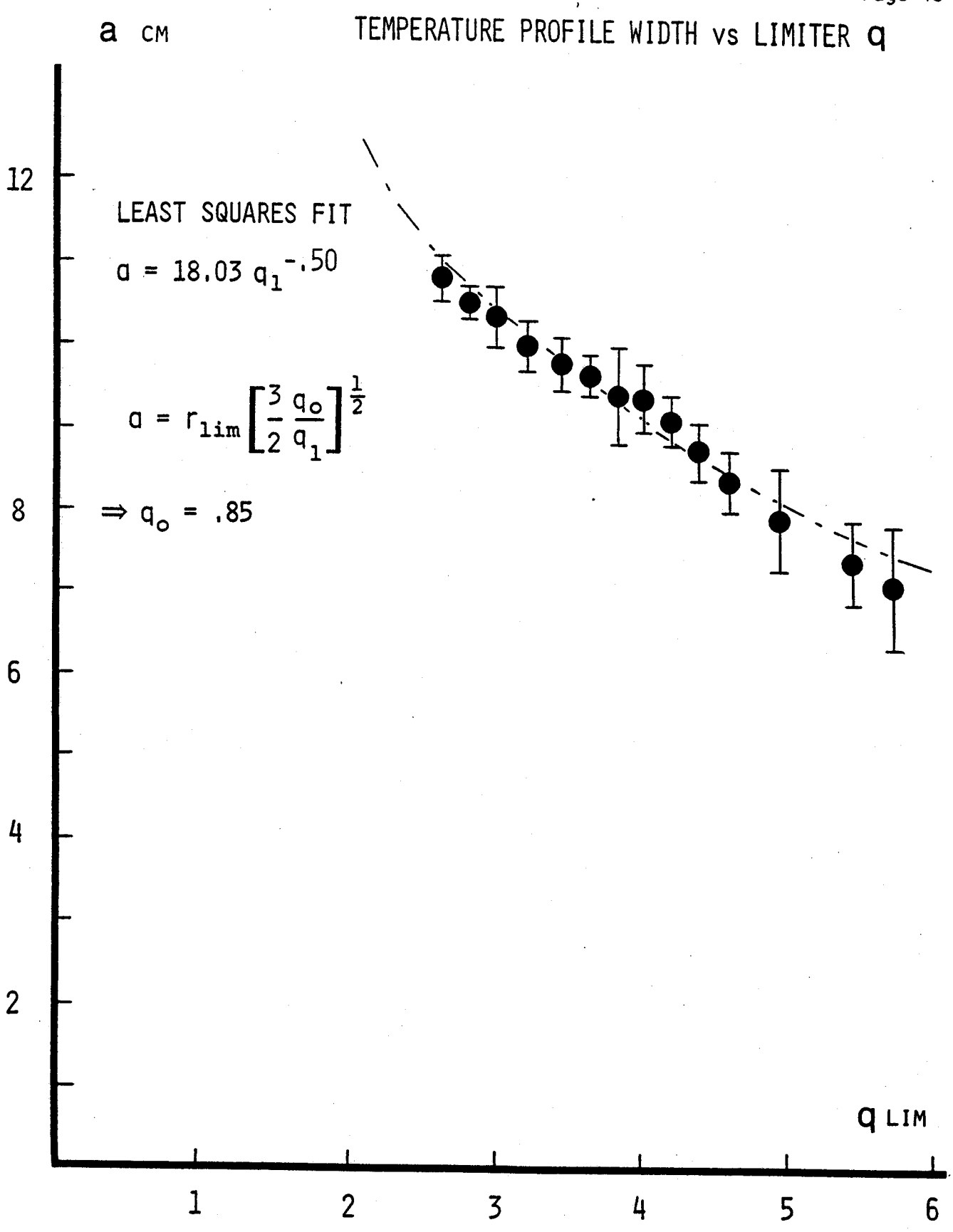

Fig.(5)
Data from discharges in Hydrogen and Deuterium; magnetic fields ranging from 50 to 100 kGauss. The error bars represent a standard deviation over an averaged set of data.

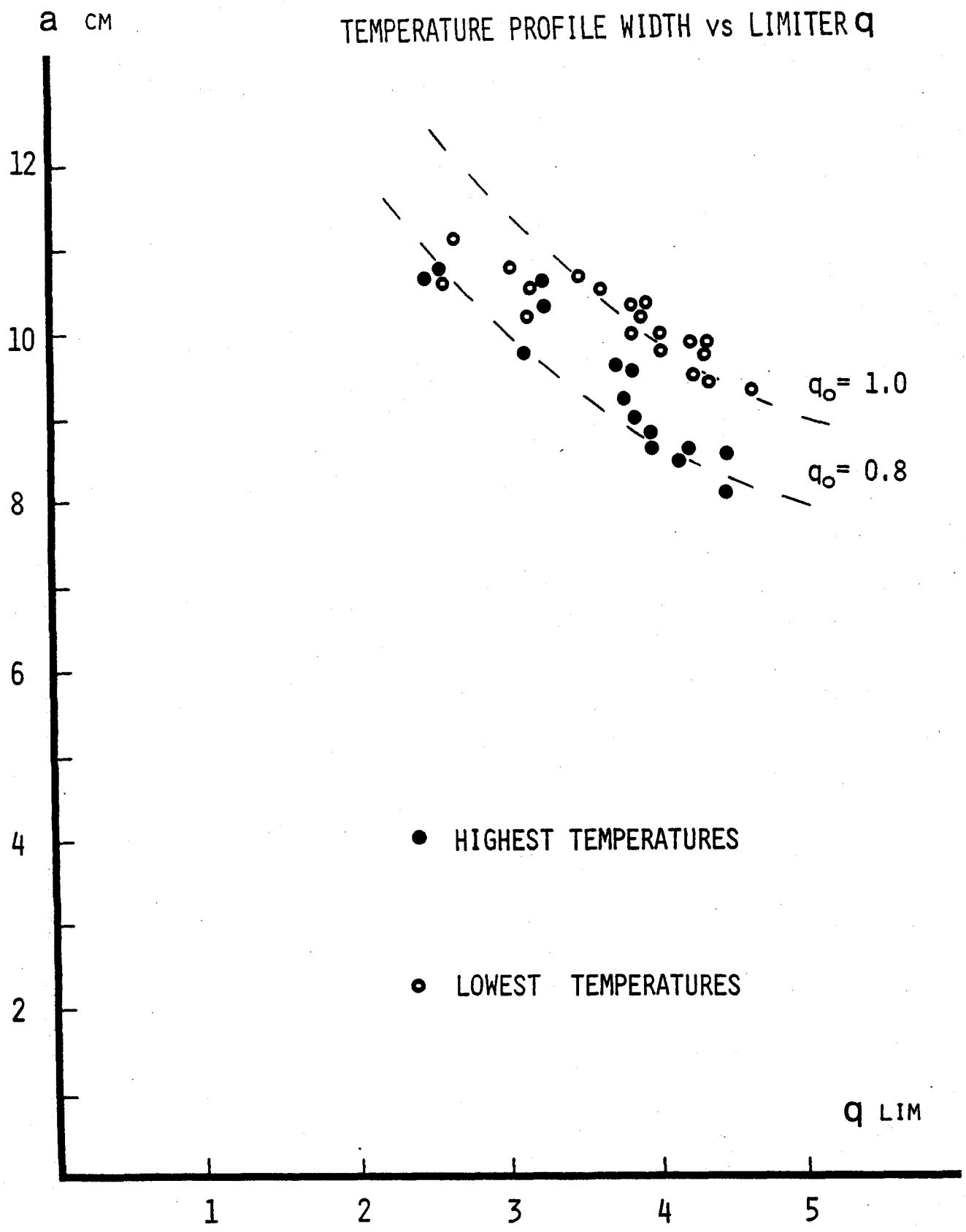

Fig.(6)

These data represent the 15% most extreme temperatures from the previous figure. This separation does not occur if data is selected according to current, density, or working gas type.

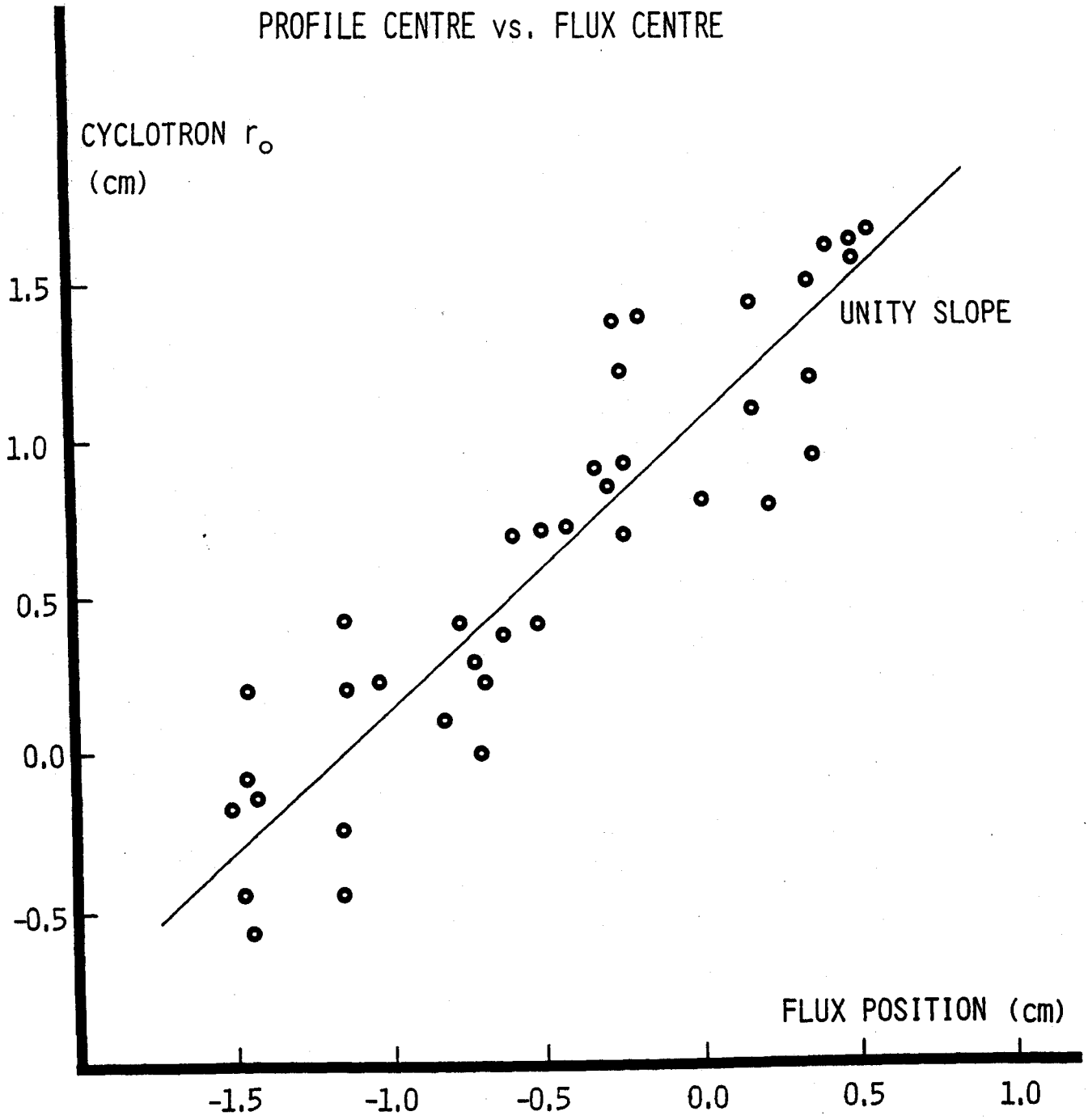

Fig.(7)

The offset in position between the profile centre and edge flux surface measurement most likely results from errors in magnetic field calibration, and should not be interpreted as resulting from a Shafranov shift. For these data the same field calibration was employed for discharges from a single day at constant field, so only a constant systematic error results.

SEC 3.0 NON-GAUSSIAN PROFILES

During the steady state portion of plasma discharges, profiles very different from Gaussian are occasionally observed. These deviations result from pathologic current distribution or from large localised radiation by impurity elements. During the current rise portion of plasma discharges, observed profile deviations are attributed to the finite diffusion time of the ohmic flux. In the most extreme cases the profiles are hollow with a depressed central temperature. While these unusual profiles may be transient, they must persist for the duration of the Michelson scan period in order to be observed.

SEC 3.1 CURRENT RISE

The plasma current is driven by an induced electric field. Because the hot plasma is a good electric conductor, magnetic flux will penetrate inward over a diffusion time:

$$\text{EQ (1)} \qquad \tau = \frac{4\pi}{c^2}\,\sigma\,L^2 = .55\,T^{3/2}\,L^2 \quad \text{(msec, KeV,cm)}$$

where σ is the plasma conductivity and L is the diffusion length. During steady state this diffusion time is about 45 msec, for Te = 1.0 keV and L = 9 cm, while the ohmic flux changes over a time scale of 400 msec. Because diffusion through the plasma is quicker than the change in ohmic flux at the edge, the induced loop voltage will be nearly constant across the plasma cross section. The assumption of constant voltage made in sec (1) is justified during steady state.

During current rise (fall) the ohmic flux is being changed over times comparable to the magnetic diffusion time, consequently flux, and hence current, will be added (removed) preferentially from the outer portion of the plasma. The corresponding current distribution will be broader (narrower) than predicted for steady state. During the initial ionisation period the diffusion time is close to zero because the plasma is a poor conductor. Once ionisation is complete the diffusion time rises as the temperature increases. Because flux cannot penetrate the plasma at the rate of the initial current rise, the additional current will flow along the outside of the plasma. In some instances a hollow current profile will be produced by a rapid current rise.

The relationship between the temperature and current profiles expressed in eq (2.7) implicitly requires a constant loop voltage across the plasma cross section. This condition does not apply during current rise when the rapidly changing flux creates a higher voltage at the plasma edge; so a hollow current profile does not necessarily require a similar temperature profile. However, a hollow temperature profile during current rise almost certainly indicates a comparable situation with the current, since the increased conductivity at the plasma edge resulting from the higher temperature together with any increased voltage can only result in an increased edge current density. Thus a measured hollow temperature profile during current rise indicates the coexistence of a skin current.

An example of this skin effect is shown in fig.(1), where the evolution of the hollow profile can be followed through the current rise. The transition from hollow to peaked profile during such a discharge is not continuous, but is accomplished by a sudden disruptive rearrangement of the current distribution. The profile shape during current rise is determined during and shortly after plasma breakdown. If the earliest measurable profile is hollow, this feature will persist during current rise. If the first measured profile is peaked, subsequent profiles will also be peaked.

The persistence of the hollow current (temperature) profiles beyond the magnetic diffusion time results from the localisation of ohmic heating power to regions of highest current (temperature). The disruptive conversion from hollow to peaked profiles undoubtedly ensues from the instability of hollow profiles to various tearing modes[1].

SEC 3.2 IMPURITY RADIATION

Localised energy loss by impurity line radiation can significantly alter the temperature profile. The energy loss rate per free electron per impurity ion is represented by the quantity L_z so that the total radiated power is:

EQ (2) $$P_{rad} = n_e\, n_z\, L_z(T)$$

where n_e, n_z are the electron and impurity ion densities. For a particular impurity element L_z will be a sensitive function of electron temperature, so that different temperature regions will have

very different radiation losses, even if they have the same impurity density. Unlike field diffusion the effect of impurity line radiation can alter profile shapes during steady state. Molybdenum is a common impurity in Alcator and an effect upon the temperature profile can be attributed to this element. A similar effect has been observed from PLT resulting from tungsten radiation[2].

Calculations[3] show that molybdenum radiated power is maximum for coronal temperatures slightly under 1 KeV and decreases sharply for temperatures above or below 1 KeV. At low densities [$n_e < 10^{14}$ cm^{-3}] when Alcator molybdenum densities are typically large, two distinct profile shapes are observed; either a peaked profile with central value of several KeV, or a hollow profile with a central temperature of 1 KeV or less. Examples of such profiles are shown in fig.(2). In the case of the hollow profile, bolometrically measured radiated power is greatly increased over the peaked case, and accounts for 70% of the ohmic input power. The hollow profile endures throughout the discharge with the central temperature never exceeding 1 KeV. The central soft x-ray emission is reduced and shows no sawtooth oscillations. In the other case the central temperature exceeds 1 KeV early in the discharge, and rises to values of 2.5 - 3.0 KeV. The central soft x-ray emission is large and shows normal sawtooth oscillations. For both cases the ohmic input power is about the same, although the spatial distribution of the ohmic power may be different.

If this input power can be converted only to plasma energy or to line radiation, for each case a balance of power requires:

$$\text{EQ (3)} \quad P_{OH} \rightarrow \text{Plasma} + \text{Radiation} = \frac{n_e T_e + n_i T_i}{\tau} + P_{rad}$$

where the confinement time τ is that expected for the condition of no line radiation, and is assumed to be equal for both cases. Furthermore, if the impurity density is assumed constant for both cases, the difference in measured plasma energy for the two situations depends upon the difference in radiation rates ΔL_z as follows:

EQ (4) $$\{\Delta T_e + \Delta T_i\} = n_z \tau \Delta L_z$$

Based upon the calculations for molybdenum and the measured temperature differentials:

EQ (5) $$\Delta T_e = 2.2 \text{ KeV} \quad ; \quad \Delta T_i = .7 \text{ KeV}$$
$$\rightarrow \Delta L_z = 1.75 \times 10^{-25} \text{ watts-cm}^3$$

assuming a confinement time of 10 msec the inferred impurity density is $n_z = 2.5\ 10^{11}\ cm^{-3}$ with a $Z_{eff} = 5$. These values for impurity density and resulting Z_{eff} are consistent with spectroscopic measurements of molybdenum line radiation and spectroscopically measured Z_{eff}.

Because the radiated power increases with temperature for values below 0.7 KeV any increase in temperature will be balanced by an increase in radiation loss. If the temperature exceeds 1 KeV the radiation term decreases with temperature so that the temperature is free to rise to higher values. Which of the two profiles will develop is determined quite early in the discharge as no transition between profile types has been observed. In fig.(3) the hollow temperature profile can be seen throughout the discharge.

It is not clear that the hollow temperature profiles of fig.(3) are associated with hollow current profiles. The lack of visible sawteeth under these conditions requires only a reduced central current density so that $q_o < 0$. That no disruptions occur suggests that the profiles are not hollow, or if so, are somehow stable against disruption. Figs.(2) and (3) refer to a particular reproducible phenomenon resulting from impurity radiation, and do not represent the plasma response to the presence of impurities in all cases. Situations have been observed where a sudden influx of high Z matter results in heating, cooling, disruption etc. These, however, are non-reproducible events which may occur randomly at any operating condition.

SEC 3.3 REFERENCES & FIGURES

1.) B. Carreras, H.R. Hicks, B.V. Waddell
Oak Ridge Report ORNL/TM-6570 (1979)
also:
Nuclear Fusion 19 1423 (1979)

2.) Plasma Physics and Controlled Nuclear Fusion
I.A.E.A. Vol.III 10 (1978)

3.) D.E. Post, R.V. Jensen
At. Data Nucl. Tables 20 597 (1977)

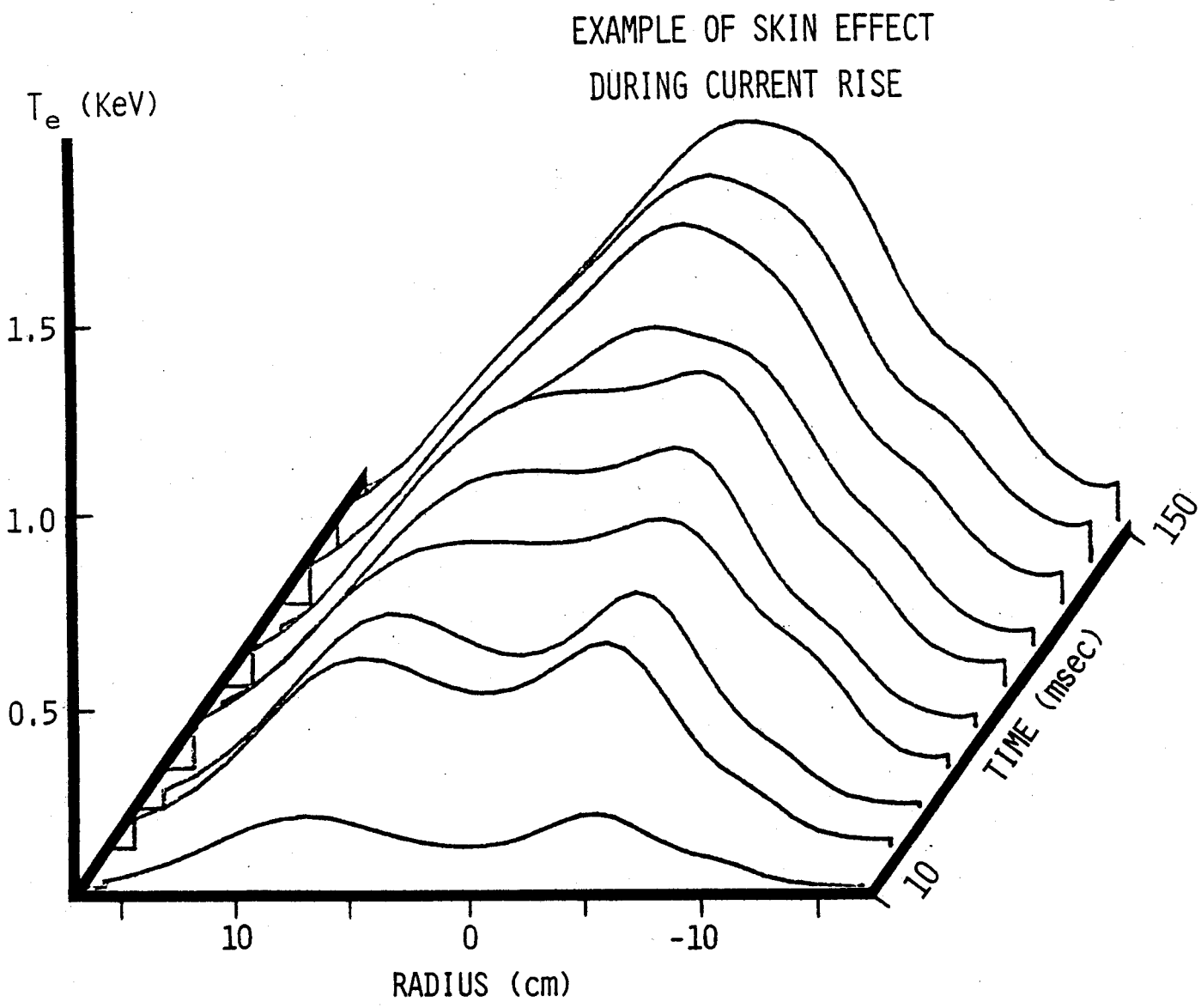

Fig.(1)
Temperature profiles measured during current rise from 0 to 400 kAmperes. 60 kGauss field; density = 1.6×10^{14} cm^{-3} line average.

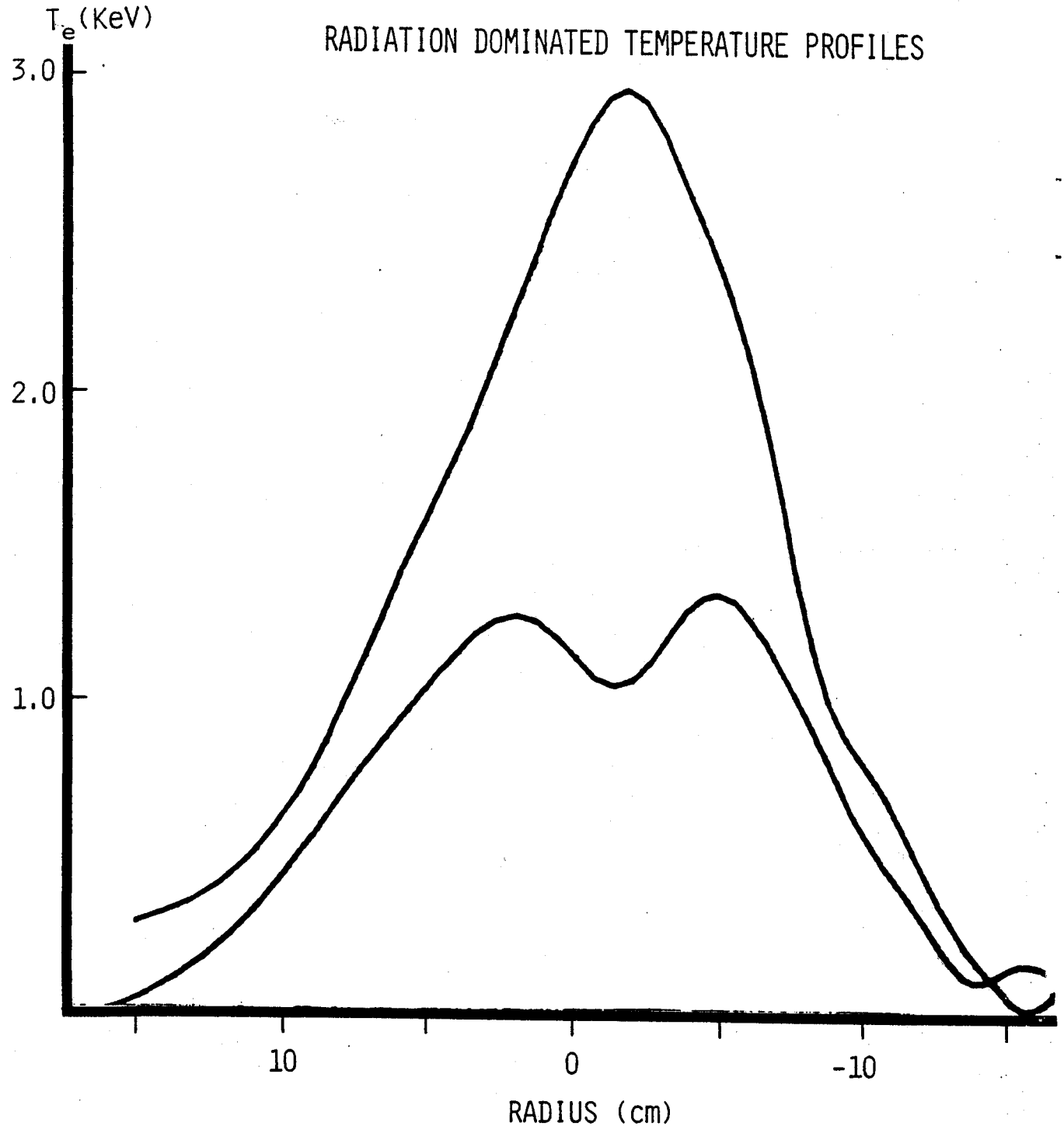

Fig.(2)
Profiles from steady state portion of consecutive Hydrogen discharges at 80 kGauss. Hollowness results from Molybdenum radiation. In both cases the plasma current = 350 kAmperes; density = 8.5×10^{13} cm^{-3} line average.

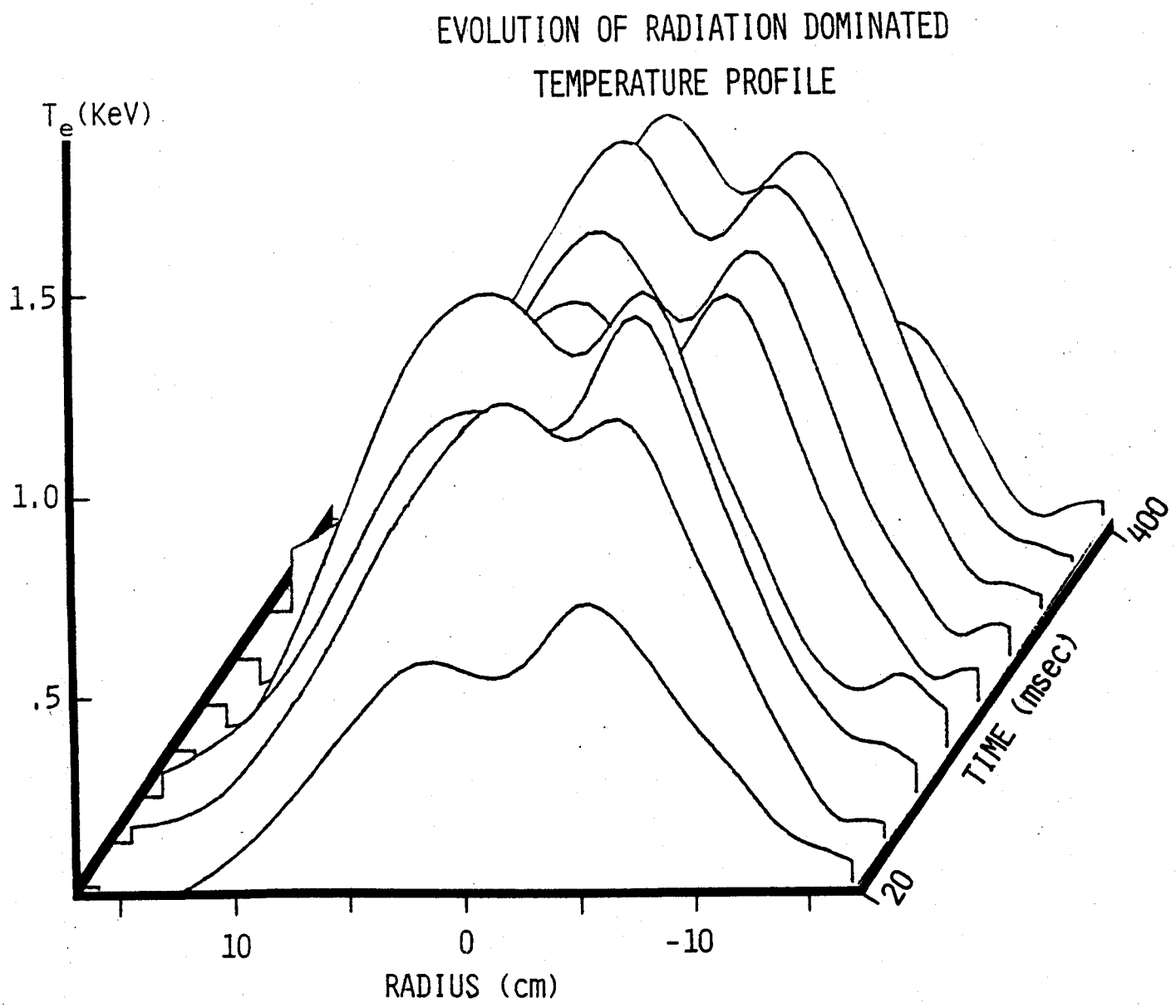

Fig.(3)
Discharge in Hydrogen at 80 kGauss. Density never exceeds 1.0×10^{14} cm^{-3} line average. No sawtooth activity is observed for the entire discharge. Hollowness results from Molybdenum radiation.

SEC 4.0 THIRD HARMONIC EMISSION

Radiation at the third gyroharmonic rivals the second harmonic in intensity, and is the highest order of cyclotron emission detected from thermal Alcator plasmas by the Michelson interferometer. At these frequencies the plasma is not optically thick to the extraordinary mode, but in a gray region where $\tau < 1$. Because of this the emission will not be at the blackbody level and will depend upon electron density as well as temperature. This in contrast to the case of the second harmonic where values of $\tau > 1$ allowed the assumption of blackbody emission. While the treatment of sec (2) when applied to the third harmonic can not provide temperature profiles, it does provide information regarding the plasma density. Conceptually, analysis of the second and third harmonic emissions together allows for an absolute calibration of the diagnostic system, freeing it from dependence on other sources of temperature measurement.

SEC 4.1 REFLECTIONS & OPTICAL DEPTH

The optical depth for the extraordinary polarisation of the third harmonic is[1]:

EQ (1) $$\tau_3 = .236 \frac{n_e T_e^2}{B} \qquad (10^{14}\ cm^{-3},\ KeV,\ Tesla)$$

The expected intensity from a thermal plasma is:

EQ (2) $$I_3 = I_{bb} \{1 - e^{-\tau_3}\} + I_o\, e^{-\tau_3}$$

where I_{bb} is the black body level. Because the optical depth is not

large the I_o term must be included to account for additional radiation reflected into the viewing angle from the vacuum chamber walls. If a fraction ρ of each ray is reflected when encountering the wall, summation over all reflections results in the following expression[2]:

EQ (3) $$I_3 = I_{bb} \frac{1 - e^{-\tau}}{1 - \rho e^{-\tau}}$$

The effective reflection coefficient ρ must account for radiation loss to the vacuum chamber, port extensions and windows. It must also deal with polarisation scrambling. Because the ordinary polarisation is not absorbed by the plasma, scrambling will reduce the effective reflectivity by increasing the likelihood of loss to the walls or rejection by the interferometer. (See sec (1.3))

In fig.(1) the third harmonic intensity relative to the blackbody level is plotted versus the calculated optical depth from eq (1). These data come from the steady state portion of discharges during a single run. Any systematic errors due to alignment or calibration may be assumed constant for these data. The scatter in this plot is reasonable when the strong dependence of τ upon density and temperature is considered. Inherent errors in these measured plasma parameters limit the accuracy of computed t to about 20%. The data can be described by eq (1) if an effective reflectivity of 0.5 is chosen. When operating with various toroidal fields or different optical alignments, the value of ρ inferred from plots such as fig.(1) changes. Systematic errors in calibration will be absorbed by ρ making it a measure of more than reflectivity.

In fig.(2) the measured electron temperature is plotted versus the product of the line average density and the ratio of second and third harmonic intensities. In this format the potential usefulness of the third harmonic as a diagnostic is illustrated. Provided that a curve such as fig.(2) has been previously generated it can be used to infer the density from the measured temperature, or temperature from the known density. In the latter case a temperature calibration of the second harmonic can be achieved. In practice this technique provides a check of the calibration currently being used, but does not free the system from independent temperature measurements. Every new alignment requires a new curve like fig.(2). Ideally, a situation can be realised where the systematic error remains constant, or can be computed. A single curve such as fig.(2) would then be a useful tool for measuring temperature.

SEC 4.2 PROFILE SHAPE

Given that its intensity is proportional to the optical depth, the third harmonic spatial profile becomes a function of the density and temperature profiles:

EQ (4)
$$I_3(r) \propto n_e(r) \exp -3\left[\frac{r - r_o}{a}\right]^2$$

where the Gaussian temperature profile is invoked. Fig.(3) is an example third harmonic profile, plotted in the fashion of sec (3) where the frequency squared coefficient is removed. The shape, as in the case of the second harmonic, is approximately Gaussian as shown. The narrowness of the profile in fig.(3) results from the cubic dependence upon the temperature profile. Because of this the density

profile contributes nothing to the shape of the third harmonic profile. In fig.(4) the third harmonic width is plotted against the corresponding second harmonic width for a number of discharges. The ratio of widths is nearly $\sqrt{3}$, which reflects the fact that the intensity is proportional to the cube of the temperature. This plot only confirms that the density profile is broad, and can not be used to empirically describe the shape. For example, the difference between a parabolic and square root parabolic density profile would not be discernible in the third harmonic width.

SEC 4.3 REFERENCES & FIGURES

1.) Engelmann & Curatolo
Any finite density effects will be incorporated into the factor ρ so that only the nT^2 dependence of the optical depth is important.

2.) D.A. Boyd
Int. J. Infrared & MM. Waves 1 45 (1980)

This reference contains a general description of the process by which density profiles can be extracted from the third harmonic emission.

RELATIVE INTENSITY vs OPTICAL DEPTH
FOR THIRD HARMONIC

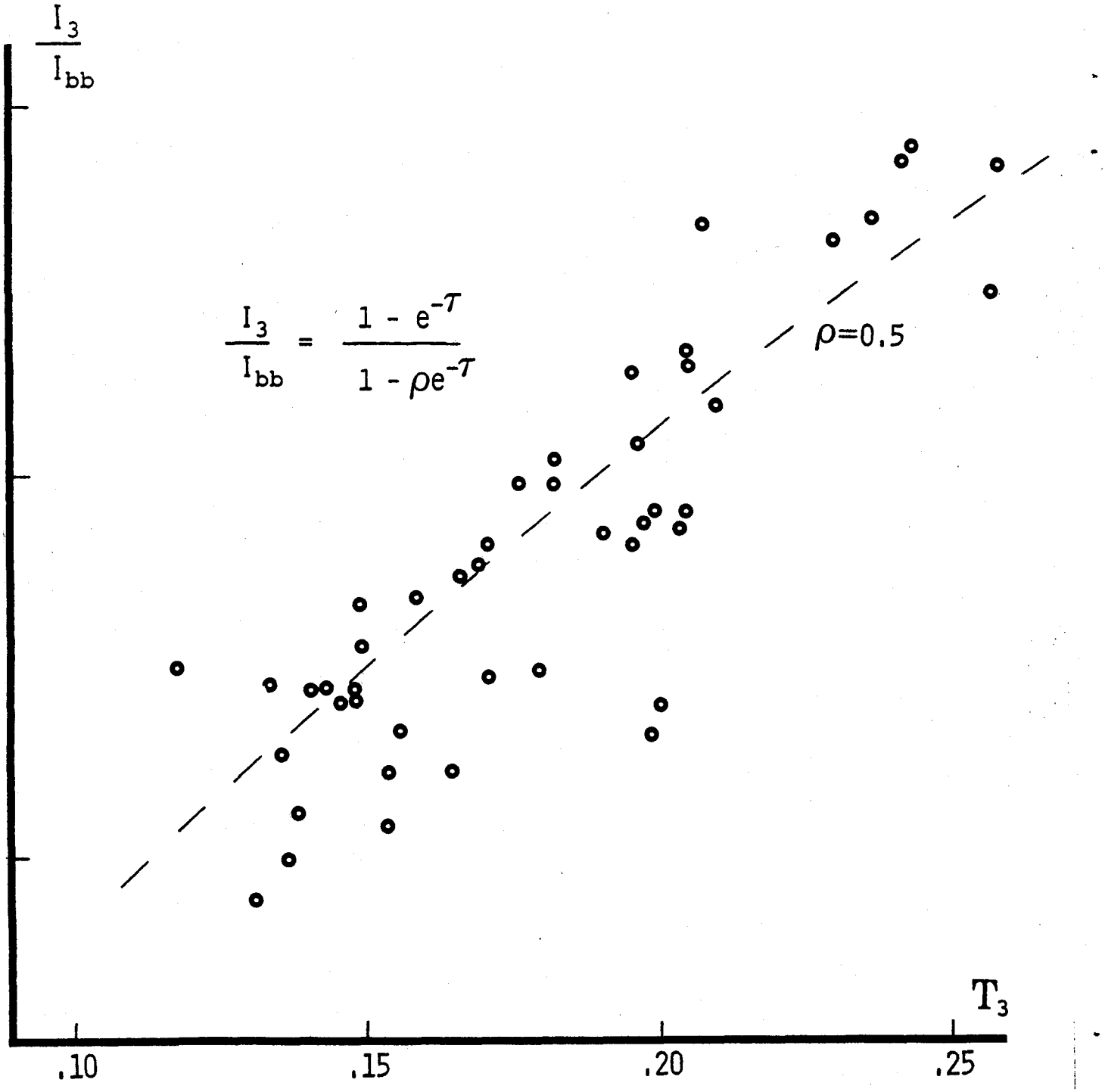

Fig.(1)
Third harmonic intensities from Hydrogen discharges at 80 kGauss. The optical depth is calculated from measured temperatures and densities.

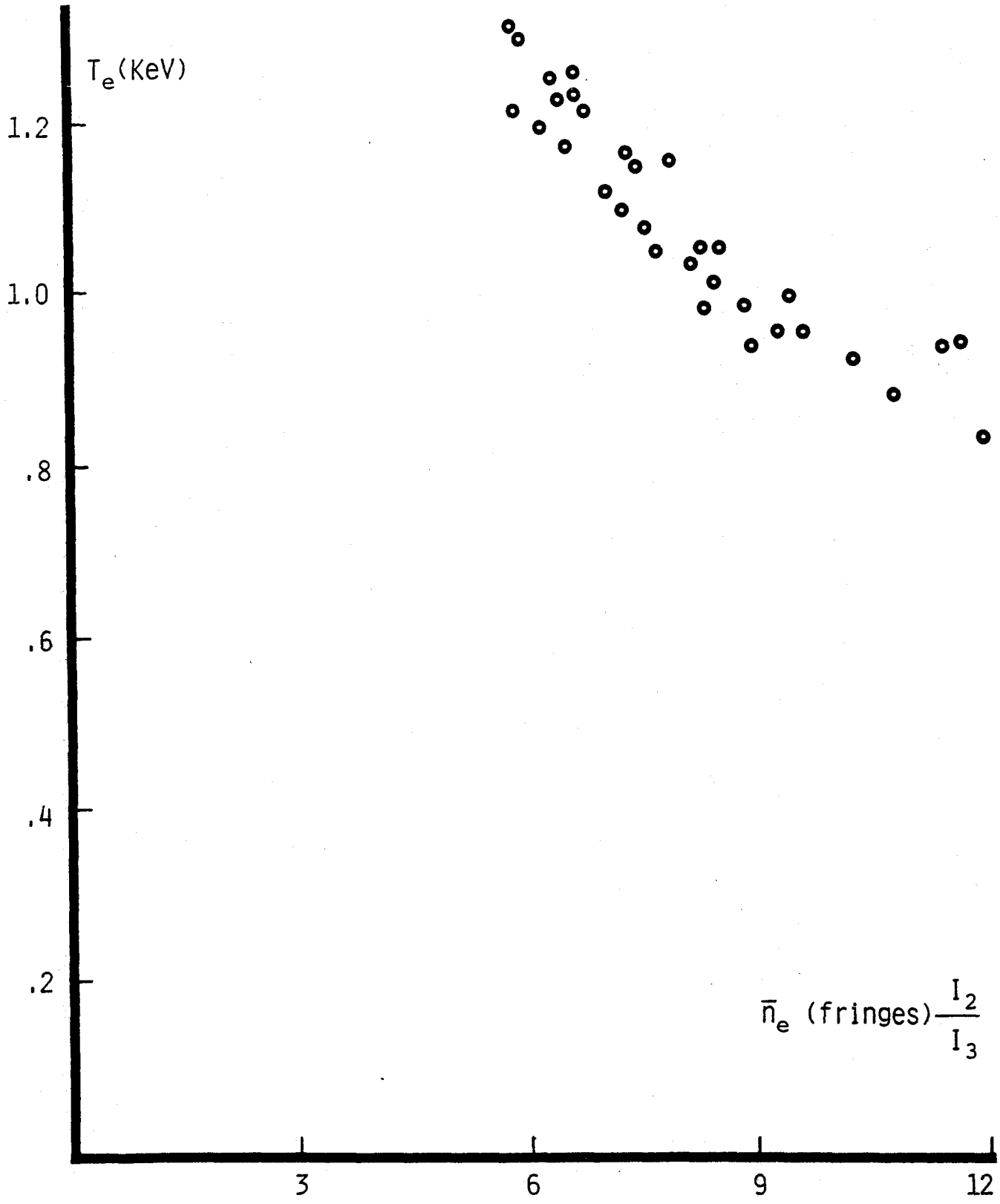

Fig.(2)
Data from Hydrogen discharges at 80 kGauss. The 'fringe' is the experimental unit of density, 1 fringe = 5.6×10^{13} cm^{-3} line average.

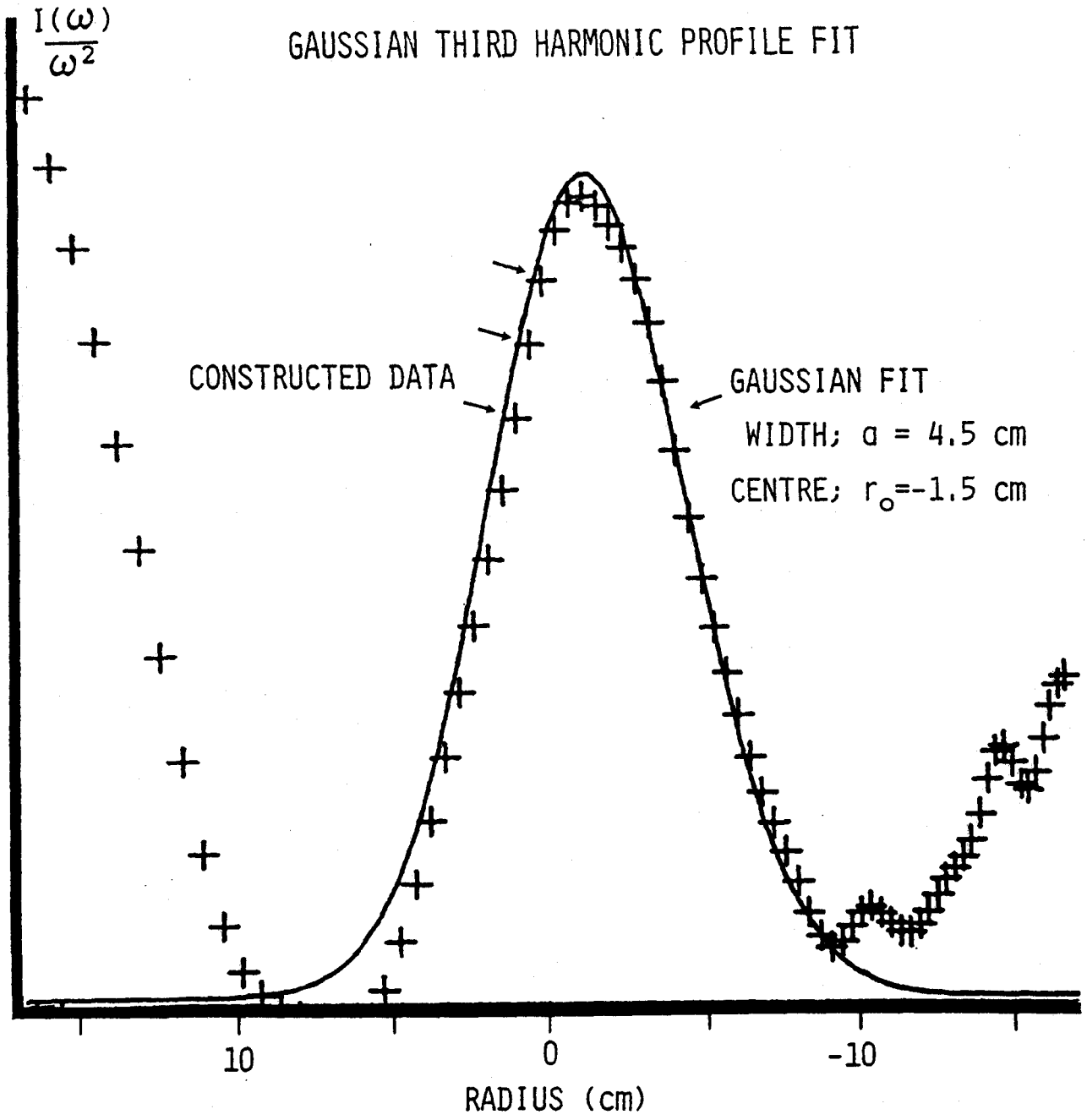

Fig.(3)
Third harmonic profile from the steady state portion of discharge at 80 kGauss. Density = 2.6×10^{14} cm^{-3} line average. The steep increasing signal on the outer edge is due to overlap of the second harmonic.

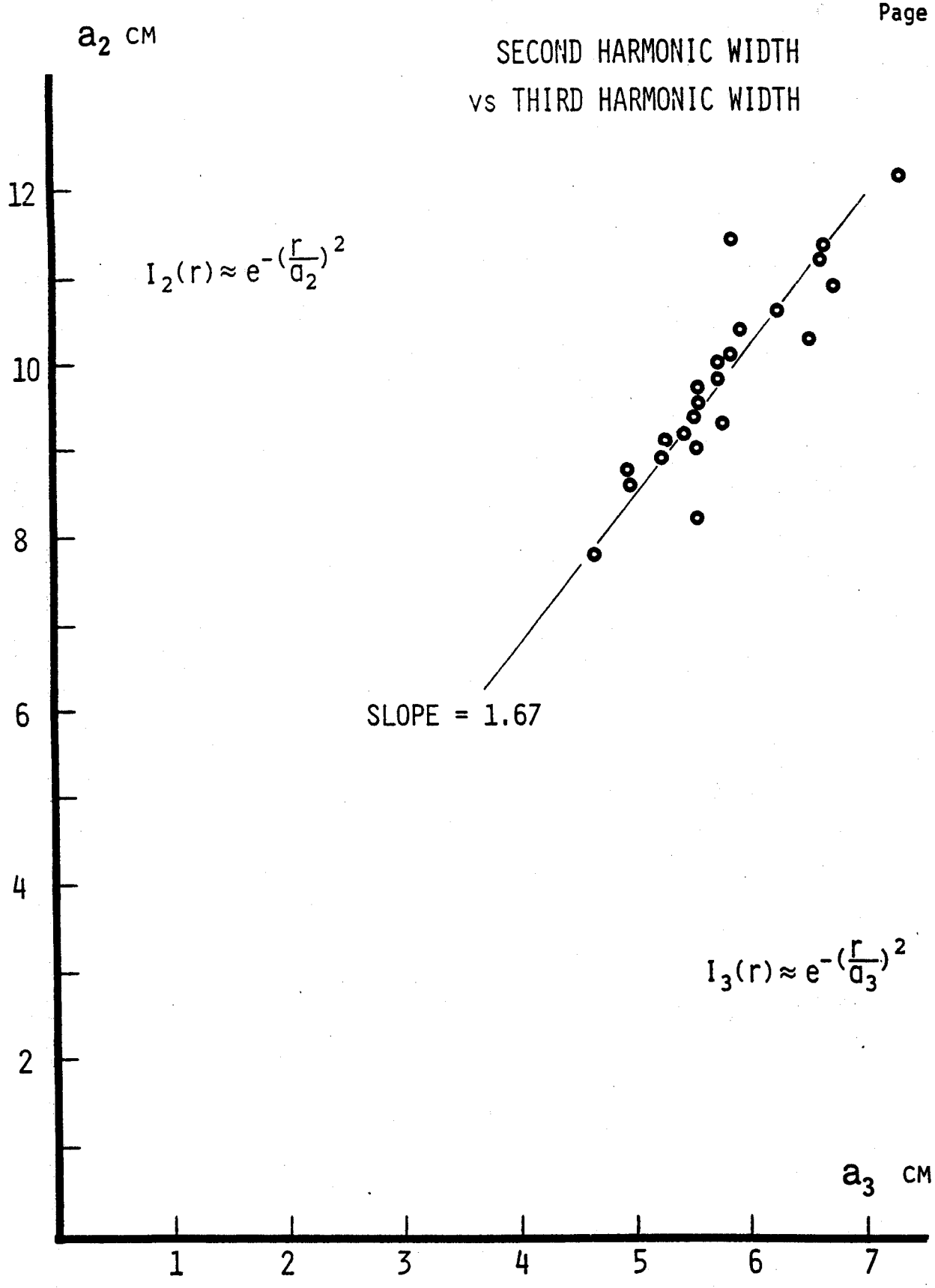

Fig.(4)
Data from sawtoothing discharges at 80 kGauss. Widths are determined by Gaussian fits to corresponding harmonic emissions.

SEC 5.0 TEMPERATURE FLUCTUATIONS

The Michelson interferometer requires an oscillation period to generate a single interferogram. The resulting spectrum is not measured at one time but is representative of this entire period. Nor is the spectrum swept in time, with each frequency corresponding to a different time during the sweep. If the emission intensity changes during the scan period, this change appears in the interferogram, and consequently in the spectrum through the fourier transform. The problem with temporal fluctuations is that there is no way the fourier transform process can separate features in the interferogram resulting from temporal variation from features which are produced by the action of the interferometer. For example, a single narrow spike of emission will produce a sinusoidal perturbation on the spectrum. Because data is sampled at irregular time intervals, periodic fluctuations in emission intensity will not produce periodic fluctuations in the interferogram, hence no sharp spectral features will result.

The study of emission fluctuation is best performed with a monochromator, such as the Fabry-Perot interferometer which provides adequate time resolution, while relying upon discharge reproducibility to measure separate frequencies one at a time. Two common fluctuations in cyclotron emission are due to the sawtooth instability and to plasma motion.

SEC 5.1 FABRY-PEROT INTERFEROMETER

The Fabry-Perot interferometer is an etalon of two parallel reflective metal meshes. The separation between meshes is adjustable. Radiation will be transmitted through the device if its wavelength is an half integer times the mesh separation. Thus the device will transmit a fundamental frequency and higher orders of this frequency. So, for example, when viewing the second gyroharmonic as the fundamental frequency, radiation at the fourth harmonic will be transmitted in the second order. This effect must be considered when using the Fabry-Perot. The device is non-polarising so that a separate polarising grid must be used if only one polarisation is desired.

The resolution, or finesse, in the first order of transmission is determined by the wavelength viewed and by the mesh spacing[1]:

EQ (1) $$F = \pi\{2g \ln(g/2\pi a)\}^{-2} \lambda^2$$

where g is the mesh spacing (lines per inch) and a the wire width. While a large finesse allows high resolution it reflects a large amount of available incident signal. In practice a modest finesse is more desirable so that a reasonable signal to noise ratio can be maintained.

SEC 5.2 SAWTOOTH INSTABILITY

The sawtooth instability has been modelled[2] by a growing perturbation of the q = 1 surface resulting in an internal disruption which flattens the central temperature and densities to the values at the q = 1 surface. The redistribution of energy extends beyond this

surface, so that the density and temperature will increase after the disruption for regions just outside the q = 1 surface. Inside this surface the sawteeth are 'normal', outside, 'inverted'. The q = 1 surface is identified with the point of inversion where sawteeth change from normal to inverted. This is the model which will be used as a basis for comparison of measured quantities.

When observing sawteeth in the optically thick extraordinary polarisation of the second electron gyrofrequency, the amplitude of the sawtooth is a direct measure of the temperature variation. A plot of this change relative to the time average local temperature is plotted as a function of position in fig.(1). Rather than absolute magnitude a ratio of temperature change to average temperature is used to characterise the sawtooth. This eliminates the need for precise calibration and corrects for any shot to shot variation.

The model used to describe sawtooth temperature fluctuations is outlined in fig.(2). Before the disruption the profile is assumed Gaussian, though not necessarily the same as the 'average' profile of sec (2). For example, the pre-disruption profile may be more peaked and narrower, reflecting a slightly smaller value of q_0. The post-disruption profile is taken to be flat in the central region such that q = 1 throughout this area. Using this model, the predicted fractional sawtooth amplitude as a function of position is:

EQ (2)
$$\frac{\Delta T(r)}{T(r)} = 1 - \exp\left[\frac{r^2 - x^2}{a^2}\right]$$

where x is the 'inversion point' of the sawtooth. This position depends upon the temperature profile width a, and the q value on axis,

q_o. The inversion point and the pre-disruption q = 1 surface are related, but not equal. For a peaked current profile the pre-disruption q = 1 radius will always occur slightly outside of the inversion point, according to this model. The radial extent of the sawtooth perturbation is restricted by requiring conservation of plasma density, and is approximated by $r_{max} = \sqrt{2}\, x$. For reasonable values of q_o and a, as inferred from measured temperature profiles, the inversion point occurs at radii varying from x = 2 cm to x = 5 cm. The corresponding central sawtooth amplitude is expected to vary from 7% to 20% according to the model.

A further consideration is the spatial resolution of the measuring instrument, which is not negligible compared to the size of the feature being measured. The Fabry-Perot is used in conjunction with the same optical path described in the appendix. The resolution along the viewing axis is governed by the finesse at the frequency being observed, while perpendicular resolution is determined by the optics employed. The measured fluctuation will be a weighted spatial average of the actual fluctuation amplitudes:

EQ (3)
$$\frac{\Delta T(r)}{T(r)}\ \text{measured} = \int_{-\infty}^{\infty} g(r,r')\, \frac{\Delta T(r')}{T(r')}\ \text{actual}\ dr'$$

where g(r,r') is a normalised response function incorporating the resolution limits of the apparatus. The appropriate choice of g(r,r') for the Fabry-Perot interferometer is:

EQ (4)
$$g(r,r') = \frac{\left[1 + \frac{2F}{\pi}^2\right]^{1/2}}{R\left[1 + \frac{2F}{\pi}^2 \sin^2 \pi \frac{R+r}{R+r'}\right]}$$

where F is the finesse. With an expected finesse of 18 for the Fabry-Perot at 420 GHz (B = 75 KG), the spot size (<2 cm diameter) and diffraction width (.3 cm) are not limiting factors in the instrumental resolution.

As shown in fig.(1) the measured central sawtooth amplitudes are insensitive to changes in q_{lim}, whether these changes result from variations in plasma current or in magnetic field. The inversion point does change with decreasing q_{lim} as expected, but the profile width also changes, leaving the ratio x^2/a^2 constant. Since:

EQ (5) $$q_o = \exp \frac{-x^2}{a^2} \qquad : \frac{\Delta T}{T}(r=0) = 1 - \exp \frac{-x^2}{a^2}$$

the constancy of central sawtooth amplitude indicates an invariance of q_o.

Within the context of the model of fig.(2) the central sawtooth amplitude is determined by x and a, while the arguments of sec (2) relate a with q_o and q_{lim}. Finally, eq (5) identifies x with q_o and a. It is unlikely that a single value of q_o will satisfy all these relations, however, by invoking the uncertainties in the measured quantities it is possible to nearly satisfy them all. The data shown in fig.(1) can be made consistent with the model if a pre-disruption value of q_o = .80 is chosen. The variation of q_o between .8 and 1.0 during a sawtooth compares favourably with the 'average' q_o = .85 of sec (2), since the observed linear temperature change with time between sawteeth suggests a 3/2 power current density, or q_o,

variation.

Fig.(3) shows the sawtooth amplitude for discharges in helium under otherwise identical conditions as those for fig.(1). The inversion point is the same in the two figures, but the amplitude in helium is doubled what it is in hydrogen or deuterium. While doubling the amplitude, the sawtooth frequency is halved, indicating that the heating of the electrons occurs at approximately the same rate in both cases. The amplitude difference can not be related to an ion mass difference since no dissimilarity was detected between hydrogen and deuterium. There is insufficient data to make a similar claim regarding Z_{eff}. If the same sawtooth model is to apply to helium as well as hydrogen it is necessary to require a smaller pre-disruption q_o (i.e. higher current density) in helium.

SEC 5.3 SYMPATHETIC PLASMA OSCILLATION

Another source of emission fluctuation results from plasma motion produced by oscillations of the controlling fields. These fields are powered by a solid state rectifier which imparts a 360 Hz ripple. In addition to noise pickup, the ripple produces a genuine effect upon the plasma position, presumably through the vertical field. When viewing a portion of the second harmonic extraordinary polarisation where the emission profile has a non-zero spatial derivative, plasma motion will produce the following fluctuation:

EQ (6)
$$\frac{\Delta T(r)}{T(r)} = \frac{-2\ r\ \Delta r}{a^2}$$

where Δr is the amplitude of plasma motion. Fig.(4) shows these

fluctuations for radial positions of -10 cm from two consecutive discharges, and compares them to the loop voltage oscillations. The two signals are out of phase with respect to each other as expected and both indicate a plasma motion of ±3 mm, this in agreement with x-ray centroid measurements[3]. The loop voltage oscillation is proportional to the positive time derivative of the vertical field ripple, so fig.(4) indicates that plasma motion lags the vertical field by about $\pi/2$ rads. This lag is attributed to a 4 msec flux penetration time through the edge plasma[4]. No motion is observed when viewing the plasma centre because the profile gradient is zero. Sudden changes in this oscillation amplitude result from rapid alterations of the temperature gradient. Fig.(5) shows this effect in conjunction with a 'marfe'[5] while viewing the -10 cm radial position. During the marfe the fluctuation level is 1% . When the marfe ceases abruptly, the average temperature increases 20% and the fluctuation level returns to 3% , as in the previous examples. If the amplitude of plasma motion is constant, the discontinuity in measured fluctuation amplitude represents a drastic change in profile width; from a = 15 cm to a = 10 cm.

These oscillations are an example where an apparent temperature fluctuation in fact results from changes in position alone. It would be incorrect to assume that the fluctuations of fig.(4) resulted, for example, from ohmic heating variation produced by the voltage fluctuation. Furthermore such fluctuations will complicate any search for small scale temperature profile variance, such as those suggested to occur in conjunction with the onset of certain MHD activity[6].

SEC 5.4 REFERENCES & FIGURES

1.) K.F. Renk, L. Genzel
Applied Optics 1 643 (1962)

2.) G.L. Jahns et.al.
Nuclear Fusion 18 609 (1978)

3.) R.S. Granetz Private Communication

4.) P. Pribyl Private Communication

5.) The marfe is an episode of enhanced Hα emission that often occurs during high density operation. It is localised to the inside plasma edge, and is accompanied by sudden increases of plasma density at the inner edge. The cause is unknown. The name 'marfe' results from the modesty of its two principle investigators; E.S. Marmar & S.M. Wolfe.

6.) R.S. Granetz
Submitted to Phys. Rev. Letters (1982)

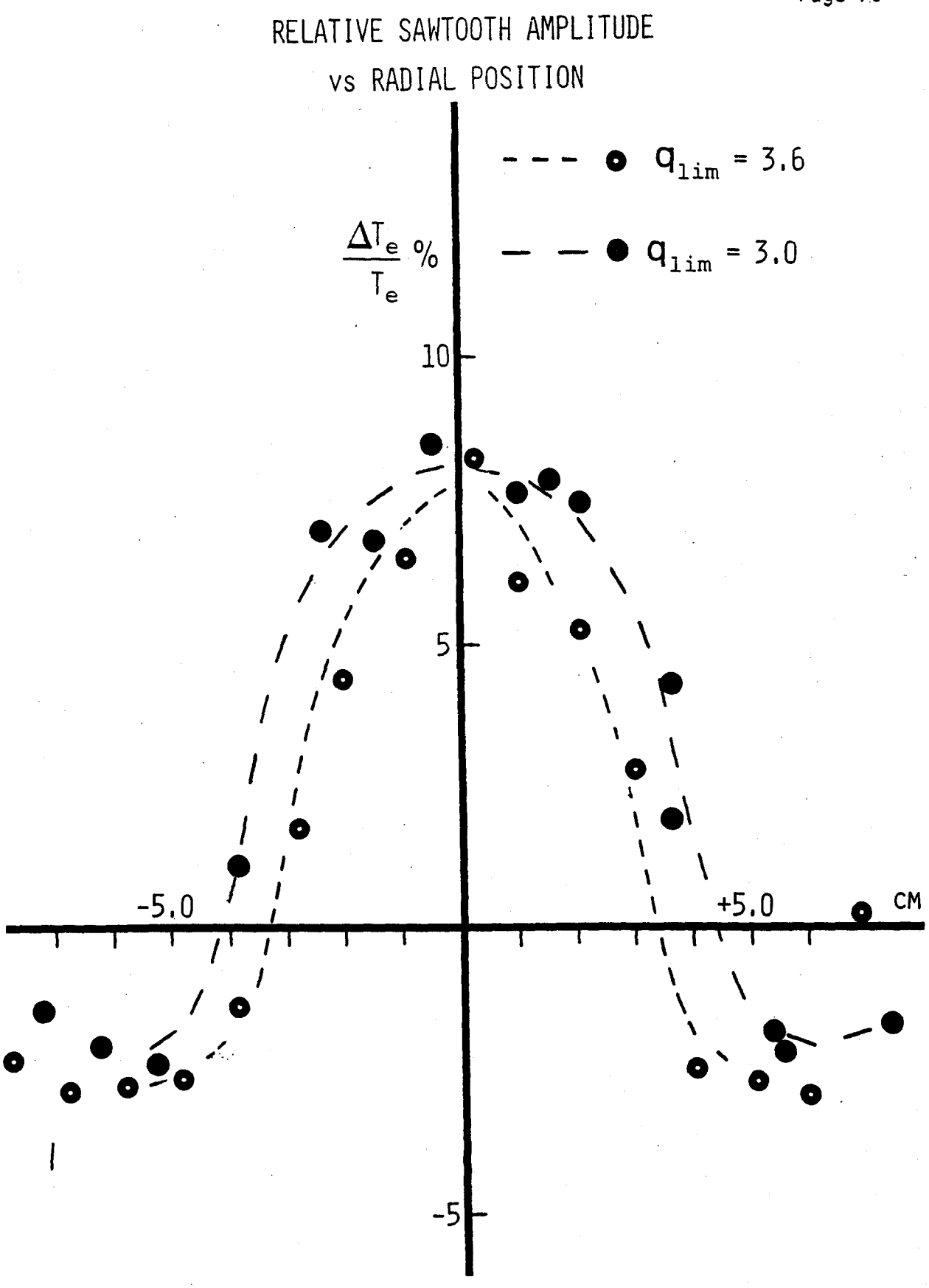

Fig.(1)
Data from discharges in Hydrogen at 80 kGauss. Densities = $3.0\text{-}4.0\times10^{14}$ cm^{-3} line average. No difference in amplitude results from changes in density, current, or magnetic field.

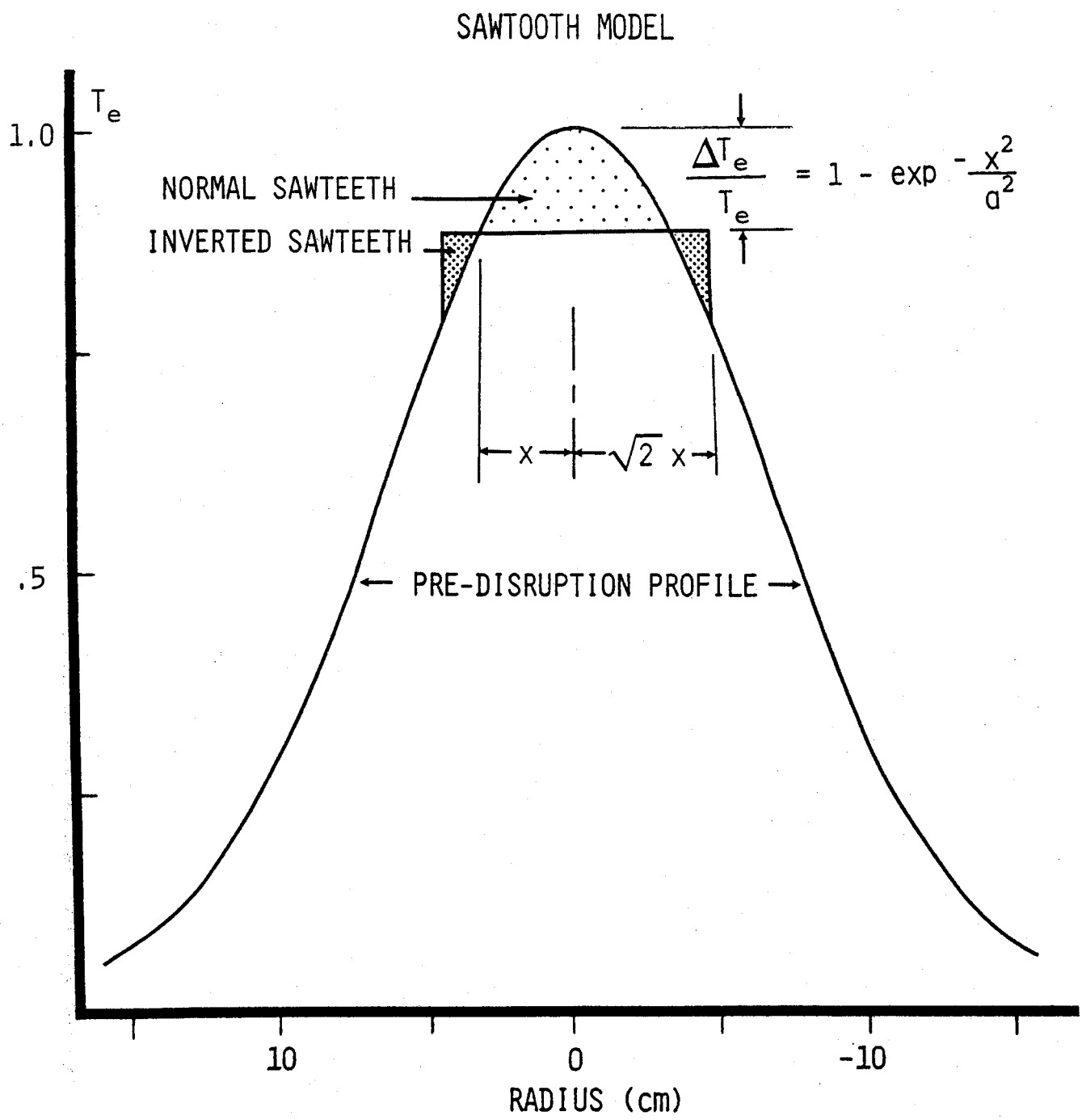

Fig.(2)

A positive $\Delta T_e/T_e$ implies a reduction in temperature - normal sawteeth. Negative $\Delta T_e/T_e$ implies an increase in temperature - inverted sawteeth.

RELATIVE SAWTOOTH AMPLITUDE
vs RADIAL POSITION IN HELIUM

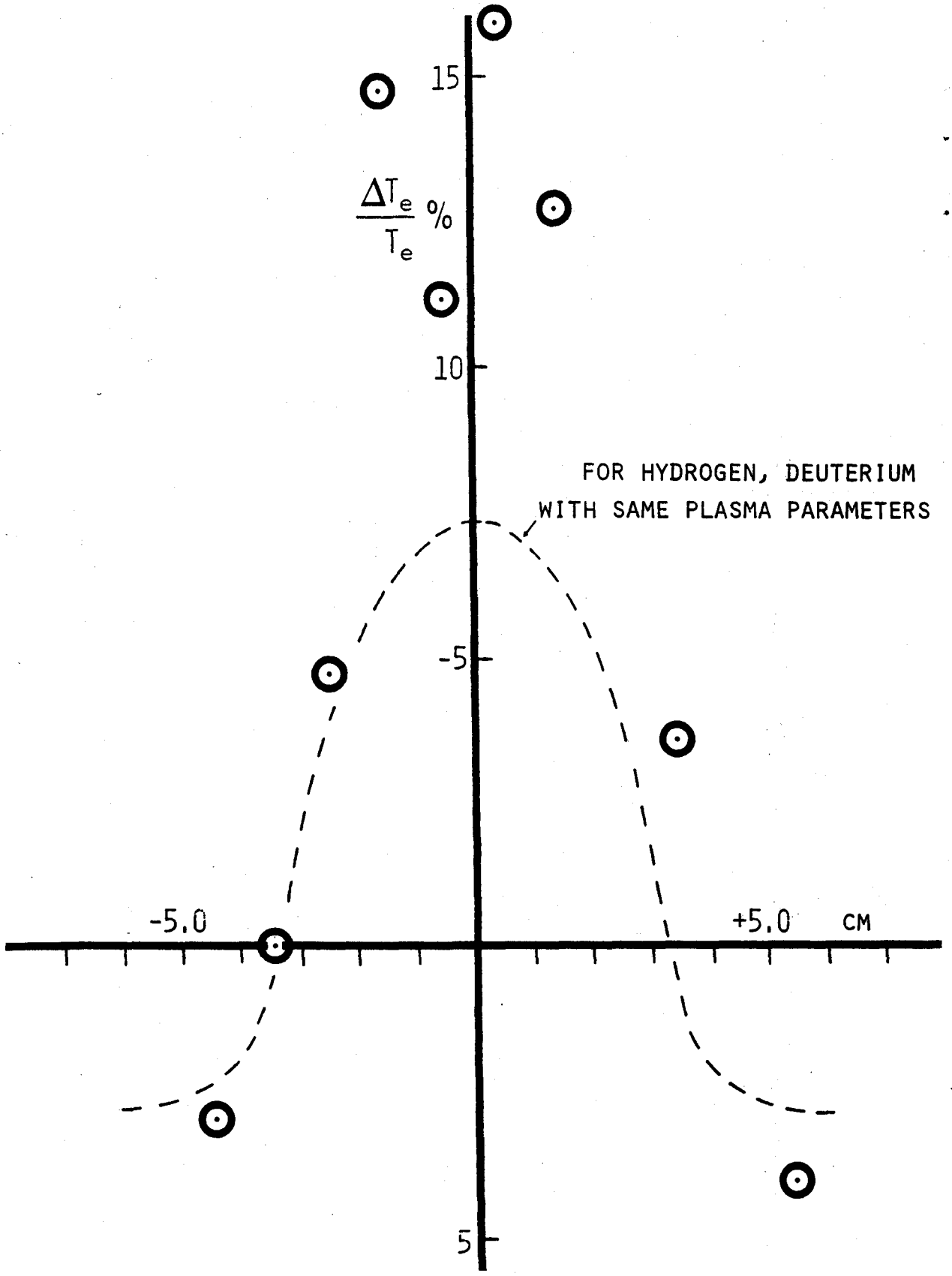

Fig.(3)
Data from discharges at 80 kGauss. Change between Hydrogen and Helium was executed during single run (day) with immediate doubling of sawtooth amplitude in Helium observed.

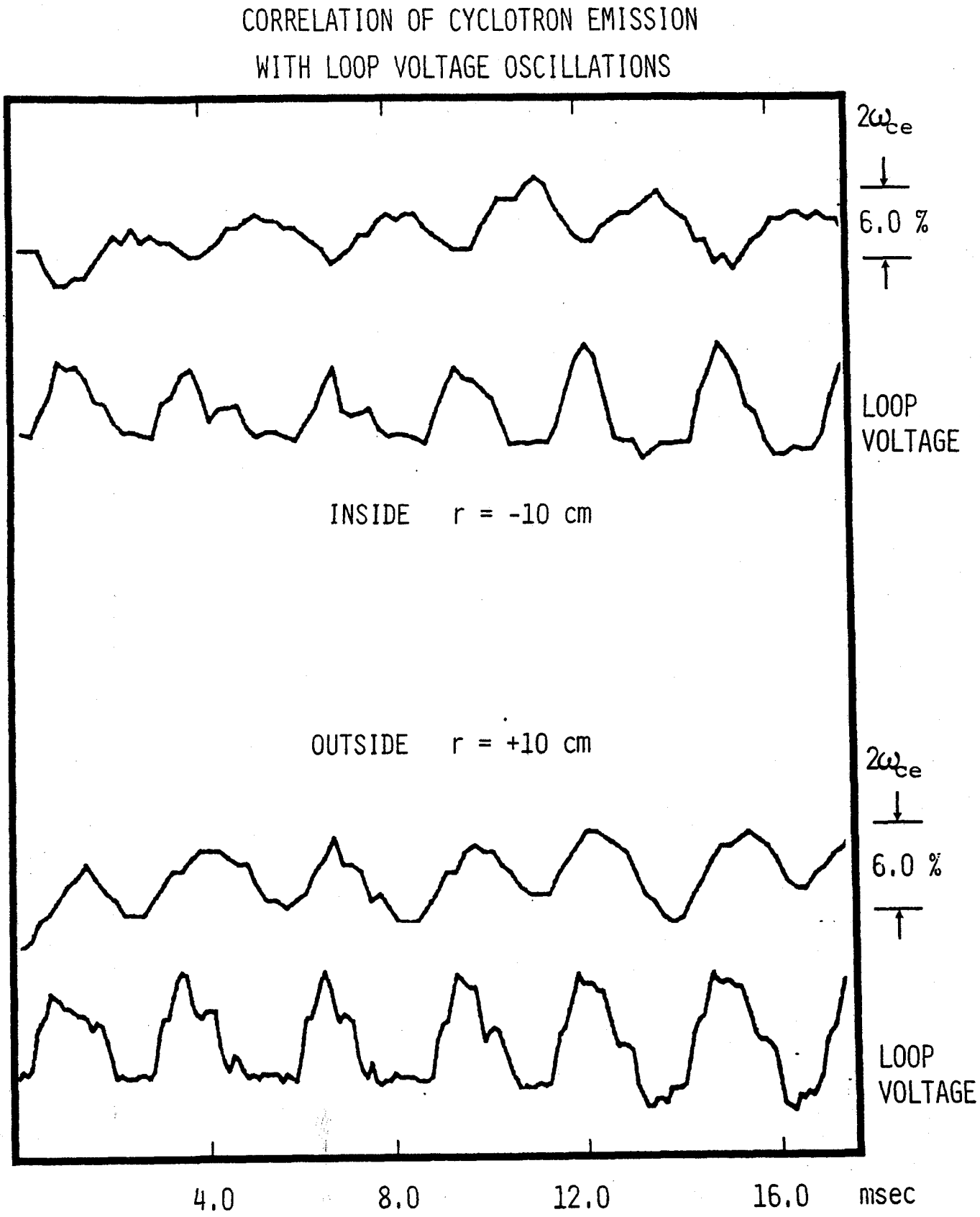

Fig.(4)
Data from consecutive discharges in Hydrogen at 80 kGauss. Density = 3.3×10^{14} cm^{-3} line average.

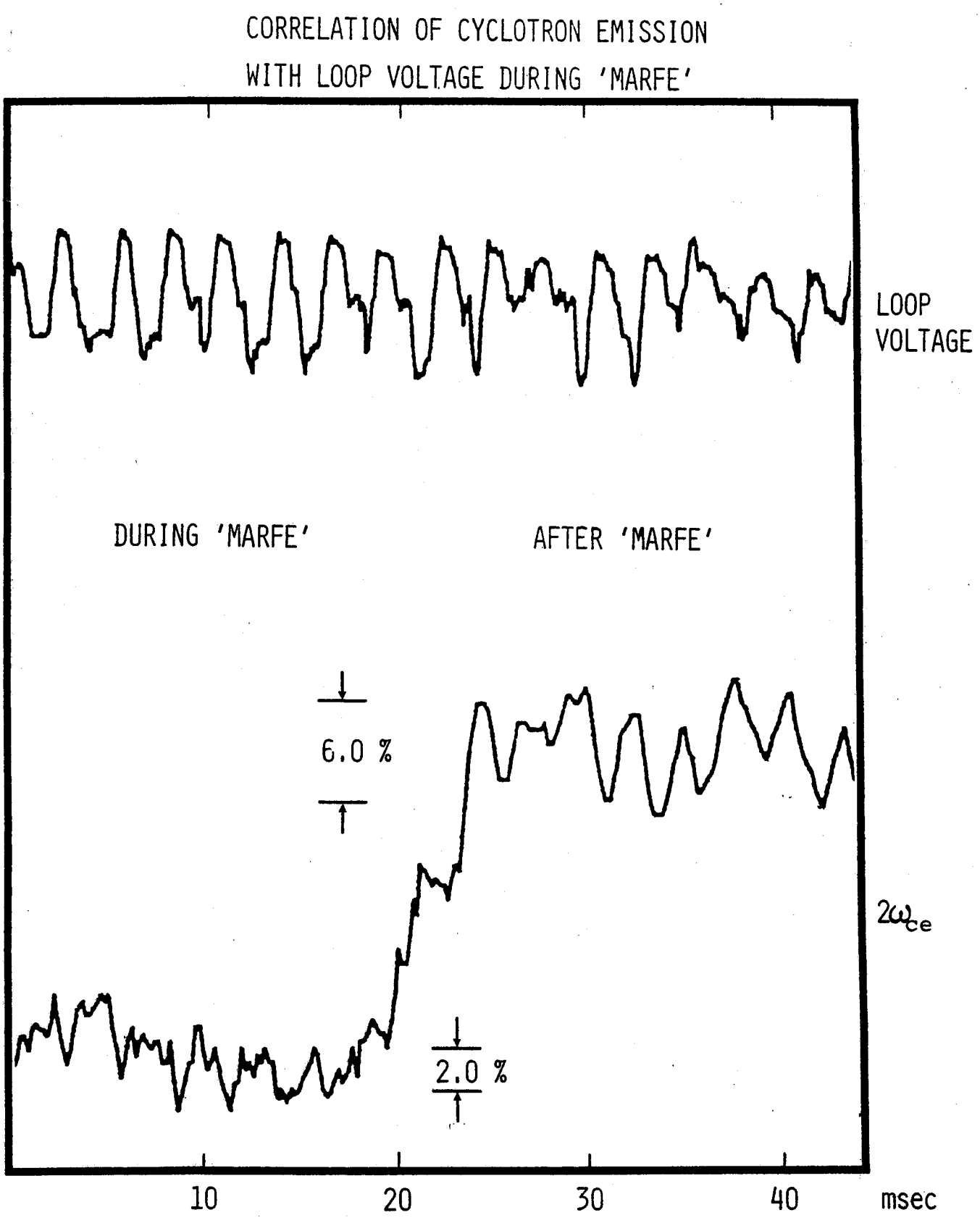

Fig.(5)

Data from current rise portion of Hydrogen discharge at 80 kGauss. Density = $2.5\times10^{14}cm^{-3}$ line average; current = 250 kAmperes at time of marfe.

SEC 6.0 DOMINANT PLASMA FREQUENCY EMISSION

'Dominant ω_{pe} emission' refers to a characteristic spontaneous radiation near the electron plasma frequency. It is usually a few times the thermal level in intensity and has spectral extent from the central plasma to the edge cyclotron frequency. Dominant emission has been observed from the Alcator Tokamak as well as other devices, and is most noticeable when $\omega_{pe}/\omega_{ce} = .6$ and a non-thermal component of the electron distribution is present. The emission intensity is nearly constant in time and can easily be measured with the Michelson interferometer. Because the trend in Tokamak operation is to achieve the highest density possible for a given magnetic field; i.e., to maximise β, the condition $\omega_{pe}/\omega_{ce} = .6$ is not a usual situation. For this reason the appearance of dominant ω_{pe} emission is not expected, except perhaps early in a discharge while the density is rising to its steady state value. The most successful explanation of this radiation involves the Cerenkov resonance with runaway electrons, with the result that the emission intensity is proportional to the current carried by these electrons.

SEC 6.1 SPECTRAL CHARACTER

Example spectra of dominant ω_{pe} emission are shown in fig.(1). In each case an intense feature at lower frequency rivals emission at the second gyroharmonic in intensity. Otherwise the spectra are completely normal, with second and third harmonic intensities equal to the values expected from a usual discharge. That the emission feature in fact occurs at the central plasma frequency is shown in fig.(2), where the frequency of maximum emitted intensity is plotted as a

function of line averaged density for many cases such as those of fig.(1). If a peak to averaged density ratio of 1.3 is assumed, the measured frequencies are in excellent agreement with the expected central plasma frequencies. This ratio of 1.3 is representative of values inferred from spectroscopic measurements[1] and from fits to multi-chord interferometric measurements[2] of the plasma density.

Although apparently narrow in comparison to emission at the second gyroharmonic, the plasma frequency feature is just barely resolved by the Michelson. The spectral width is equal to the separation of the central plasma and edge cyclotron frequencies. This is shown in fig.(3) where the half-width of the feature is plotted as a function of frequency. As the edge cyclotron frequency is approached the feature width becomes progressively narrower. At the same time the emission amplitude progressively decreases. In fig.(4) the intensity relative to the thermal blackbody level is plotted versus frequency, and this decrease can be seen. When the central plasma frequency exceeds the edge cyclotron value no emission is observed.

Dominant emission usually occurs early in discharges which would otherwise be considered normal with regard to macroscopic parameters such as current, density, and temperature. However, episodes of dominant emission are generally preceded by periods of broadband cyclotron radiation, indicating the presence of relativistic electrons, sec (1.4). The emission intensity usually decays away over a period of about 100 msec, but if the plasma density is sufficiently low, so that ω_{pe}/ω_{ce} is less than unity, the emission may persist for the duration of the discharge with nearly constant intensity.

When present, the emission is most intense for $\omega_{pe}/\omega_{ce} = .6$. For higher frequencies the intensity decreases, as shown in fig.(4), while for lower frequencies the emission , if observed at all, is much less intense. Fig.(5) is an example of dominant emission for the case $\omega_{pe}/\omega_{ce} = .4$. While the intensity is small, the feature now exhibits a double humped structure which was not apparent in the previous examples.

The dominant emission feature occurs in both polarisations with no noticeable difference in spectral shape between ordinary and extraordinary modes. The extraordinary mode emission is more intense than the ordinary, but the actual degree of polarisation is not well measured.

SEC 6.2 REVIEW OF PREVIOUS EXPERIMENTS

Measurements on TFR[3] show that the dominant emission occurs early in certain types of discharges, and decays with a time constant of 100 msec. These discharges are characterised by low densities and high temperatures with $\omega_{pe}/\omega_{ce} = .6$. The emission occurs at about the central plasma frequency and extends to the edge cyclotron frequency. In this respect the results are identical to those presented in the previous section. The intensity of emission, while greater than the thermal level, is not as intense as the examples shown in fig.(1). This situation also reflects the dominant emission seen on the JIPP T-II Tokamak[4].

The Alcator A[5] results are similar to those from TFR, the emission intensity again being less than the Alcator C case. An important difference is that the Alcator A measurements clearly show the double humped feature which is only just noticeable in fig.(5). This difference probably reflects the disparity in aspect ratios between the two machines. Alcator A has an aspect ratio $R/r_{lim} = 5.4$, while for Alcator C $R/r_{lim} = 3.9$. For $\omega_{pe}/\omega_{ce} = .6$ the separation of the central plasma and edge cyclotron frequencies will be 20% greater in Alcator A. It is reasonable to assume that this larger spectral region increases the likelihood of resolving any emission structure.

The Alcator A results also conclusively show the emission to be polarised, with more radiation coming in the extraordinary mode. The degree of polarisation, about 3:2, is consistent with the polarisation scrambling model used to explain observed ordinary mode emission at the second gyroharmonic.

SEC 6.3 CERENKOV EMISSION

Cerenkov emission occurs when the particle velocity can exceed the local electromagnetic phase velocity, that is, when the refractive index is greater than unity. For a magnetoactive plasma this situation can only be realised by the extraordinary polarisation in the vicinity of the electron plasma frequency. The plasma is optically thin in this region, so the emission can be considered by summing over all runaway electrons. Because of this summation, and the relative constancy of the emissivity for large electron velocities, under certain conditions the emission intensity will be proportional to the number of runaway electrons.

The plasma is described in the cold plasma approximation by the Appleton-Hartree dispersion relation. This requires ignoring effects by both thermal and relativistic electrons upon the dielectric properties of the background plasma. Effects caused by runaways can be ignored since the density of these electrons is assumed much less than that of the thermal plasma. In the frequency region $\omega_{pe} < \omega < \omega_{ce}$ the phase velocity of radiation will always exceed the thermal electron velocity, so warm plasma effects may be ignored.

The emitted wave is required to be in phase with the emitting electron:

EQ (1) $$\frac{\omega}{k} = v \cos\Theta$$

where v is the particle velocity, which is assumed to lie in the direction of the ambient magnetic field. Combined with the dispersion relation this coherence condition relates the frequency and angle of emission with the electron velocity. The dispersion relation for a particular choice of frequency is shown in fig.(6). The refractive index is always less than unity for the ordinary mode. The coherence condition can never be satisfied, so no emission in this mode is expected. For the extraordinary mode the refractive index is greater than unity everywhere, particularly for small angles with respect to the magnetic field.

It has been shown[6,7] that for reasonable estimates of the runaway density and energy ($n_r/n_e = 10^{-5}$, E = 200 keV) the emissivity will be strongly peaked near the plasma frequency, with intensity equal to or greater than the expected second harmonic emission from

the 1 keV background plasma. This result depends upon the exact distribution used to describe the runaway population, but is shown to be insensitive to the perpendicular component of the runaway velocity.

SEC 6.4 RAY TRAPPING

Although a sufficient emissivity exists, the radiation must exit the plasma in order to account for the observations. While the phase velocity of Cerenkov radiation will typically be within 15 degrees of the magnetic field, the group velocity will be at 70 degrees or more, that is, closer to the perpendicular direction. This can be seen in fig.(6), where the direction of the group velocity is indicated by the normal to the dispersion curve. That the group velocity of the emitted radiation is close to perpendicular does not mean that the radiation can be directly observed from the outside. Because the refractive index for the extraordinary mode decreases moving from the inside to the plasma edge, radiation may be reflected back toward the centre.

The plasma is homogenous in the direction of the magnetic field, so that the refractive index component in this direction is constant along a ray path. In cylindrical coordinates (infinite aspect ratio):

EQ (2)
$$n(r_1)\cos\Theta(r_1) = n(r_2)\cos\Theta(r_2) = \text{constant}$$
$$n(r) = \text{refractive index at } r$$

At the point of emission this constant is determined by the coherence condition:

EQ (3)
$$\{n\cos\Theta\}_{\text{emission point}} = \left[\frac{v}{c}\right]^{-1} > 1$$

At the plasma edge the refractive index approaches unity, so that total internal reflection occurs. The situation is less severe in toroidal coordinates, where the requirement for radiation to escape is[8]:

EQ (4) $$\{n \cos\Theta\}_{\text{emission point}} < 1 + \frac{r_{lim}}{R}$$

This condition is less restrictive on Alcator C than on Alcator A and TFR, which may in part explain the larger intensities observed from Alcator C. For example, spectra similar to fig.(1) have been measured from DITE[9], which has $R/r_{lim} = 4.5$. If observed Cerenkov emission in the ordinary polarisation results from multiple reflections within the vacuum chamber, the escape condition should be applied at the chamber wall, if that is the source of 'emission.' Since the refractive index is unity at this point, from eq (4) it is seen that the radiation is capable of escaping.

The most recent treatment[10] of Cerenkov emission has included the effect of multiple reflections by isotropising the reflected emission over a 2π solid angle, that is, by integrating over all angles of emission. This work is particularly successful in explaining the double humped spectra such as fig.(5). The spectral shape is a consequence of vacuum wall reflections, which necessitate some type of average over all angles of emission. Additionally a lower limit to the considered runaway electron velocities is set by the escape condition as determined from eq (4). The chosen lower limit of .8 c restricts the velocity range of emitting electrons such that only the total number of electrons in this region has any

significant effect upon the emission intensity. Hence the average intensity and the current carried by these runaways are related. Using the result from ref(10) with the reflectivities of sec (1), the runaway current is approximated by:

$$I_{run}(KAmp) \cong 4 \frac{I_x}{I_{bb}} \left[n_e \, 10^{14} \, cm^{-3} \right]^{-1/2} T_e(KeV)$$

EQ (5)

$\frac{I_x}{I_{bb}}$ = average intensity of extraordinary mode Cerenkov emission averaged over a small frequency interval.

This equation is meant to apply only to cases such as fig.(5) where the emissivity is nearly constant over some small frequency interval, and a good spectral fit can be obtained. Application of eq (5) to this particular example predicts a runaway current of 5 Kamps, which amounts to 2% the total current. This result is nearly identical to the original treatment of Alcator A data.

As the plasma frequency approaches the cyclotron frequency, two competing effects occur. The Cerenkov emissivity increases[11], which enhances the emission intensity; and the edge cyclotron frequency encroaches upon the spectral region of emission, which decreases the intensity by absorption. Thus the radiation resulting from a fixed runaway current will depend upon the particular values of the plasma and cyclotron frequencies. Fig.(5), for example, deals with the situation $\omega_{pe}/\omega_{ce} = .4$. Under this condition there is a frequency interval over which the emissivity is nearly constant, and average intensity has meaning, and eq (5) applies. This is not the situation in fig.(1) where eq (5) would predict a runaway current of 50 Kamps, or 15% the total. Certainly it would be a mistake to apply eq (5) to

fig.(4) and interpret the decreasing emission intensity as a consequence of a diminishing runaway current.

SEC 6.5 REFERENCES & FIGURES

1.) E. Marmar Private Communication

2.) S. Wolfe Private Communication

3.) A.E. Costley et.al.
Phys. Rev. Lett. 38 1477 (1977)

4.) K. Sakai et.al.
Int. J. Infrared MM Waves &1 77 (1980)

5.) I.H. Hutchinson, D.S. Komm
Nuclear Fusion 17 1077 (1977)

6.) H.P. Freund, L.C. Lee, C.S. Wu
Phys. Rev. Lett. 40 1563 (1978)

7.) H.P. Freund et.al.
Phys. Fluids 21 1502 (1978)

8.) M. Bornatici, F. Engelmann
Phys. Fluids 22 1409 (1979)

9.) A.E. Costley Private Communication

10.) K. Swartz, I.H. Hutchinson, Kim Molvig
Phys. Fluids 24 1689 (1981)

11.) A.G. Sitenko, A.A. Kolomenskii
Zh. Eksp. Teor. Fiz. 30 511 (1956)

'DOMINANT ω_{pe} EMISSION'

EXAMPLE SPECTRA

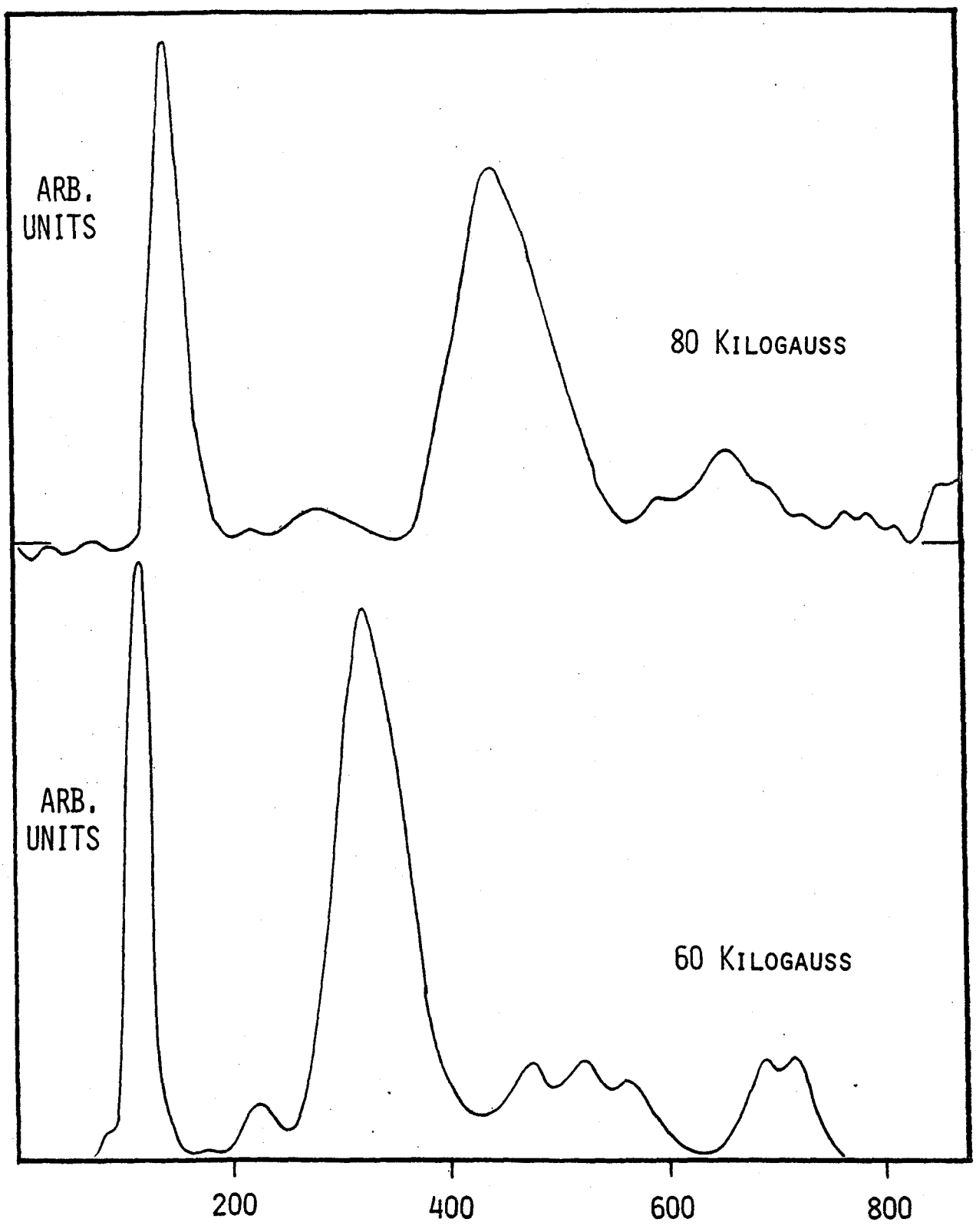

Fig.(1)

Extraordinary mode emission from times early in discharges when:

central density = 1.1×10^{14} cm^{-3} (60 kGauss)

central density = 1.5×10^{14} cm^{-3} (80 kGauss)

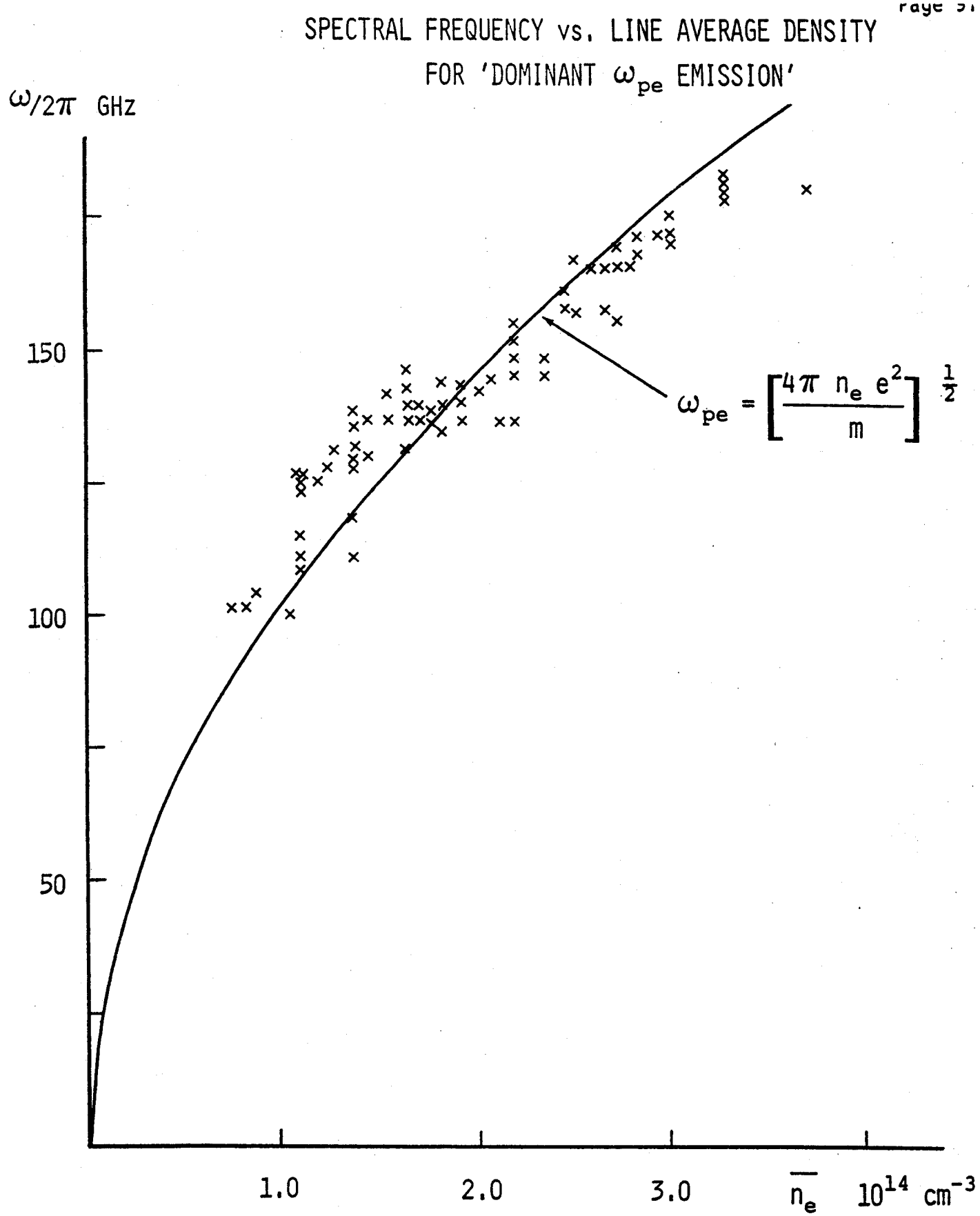

Fig.(2)

Data from ordinary and extraordinary mode emission; magnetic fields from 60-100 kGauss. The drawn curve assumes a peak to line average density ratio of 1.3

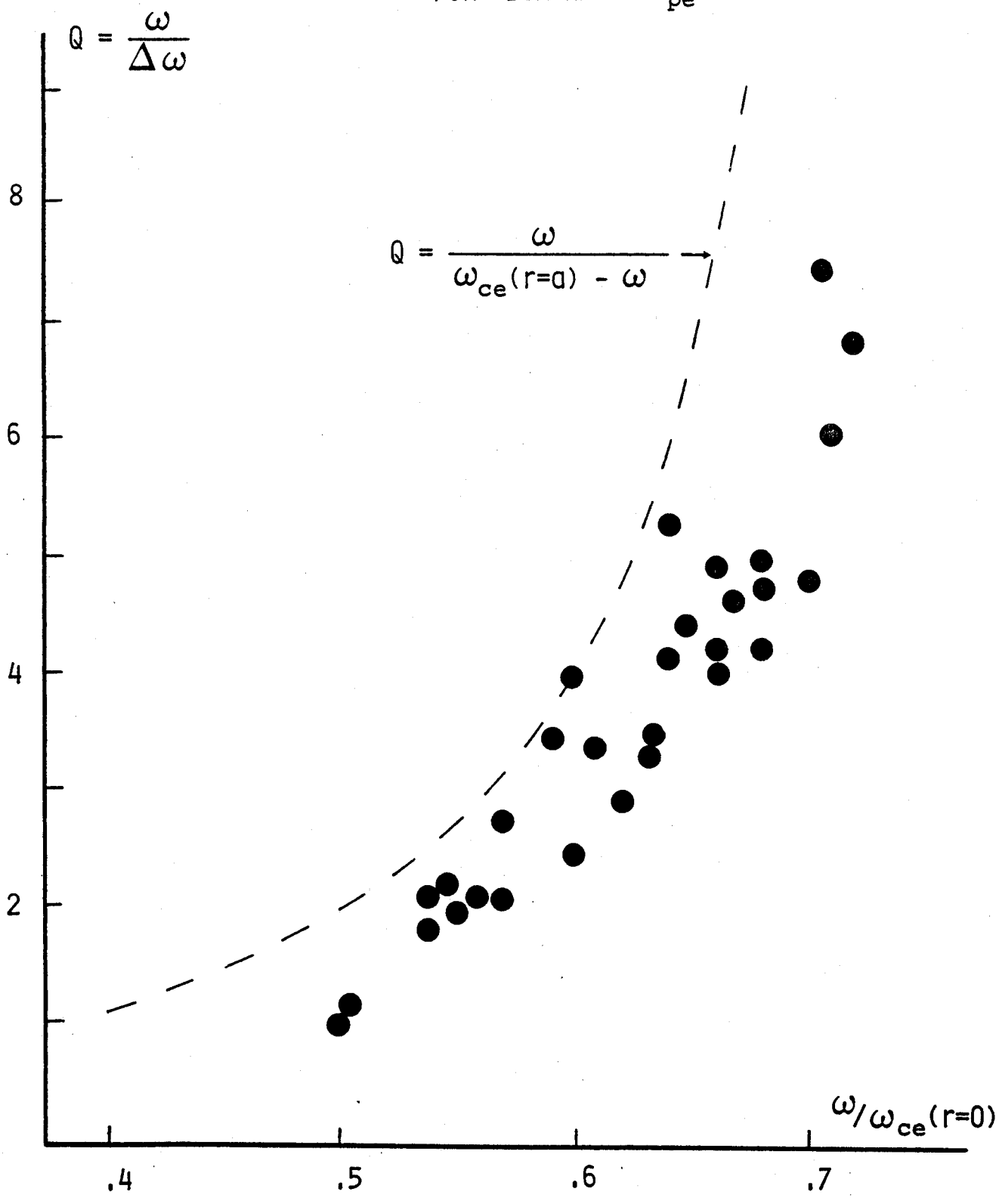

Fig.(3)
Spectral width is the FWHM of the plasma frequency line. Because of finite instrument resolution, Q in excess of 8 is not achieved.

INTENSITY RELATIVE TO THERMAL LEVEL vs. FREQUENCY
FOR 'DOMINANT ω_{pe} EMISSION'

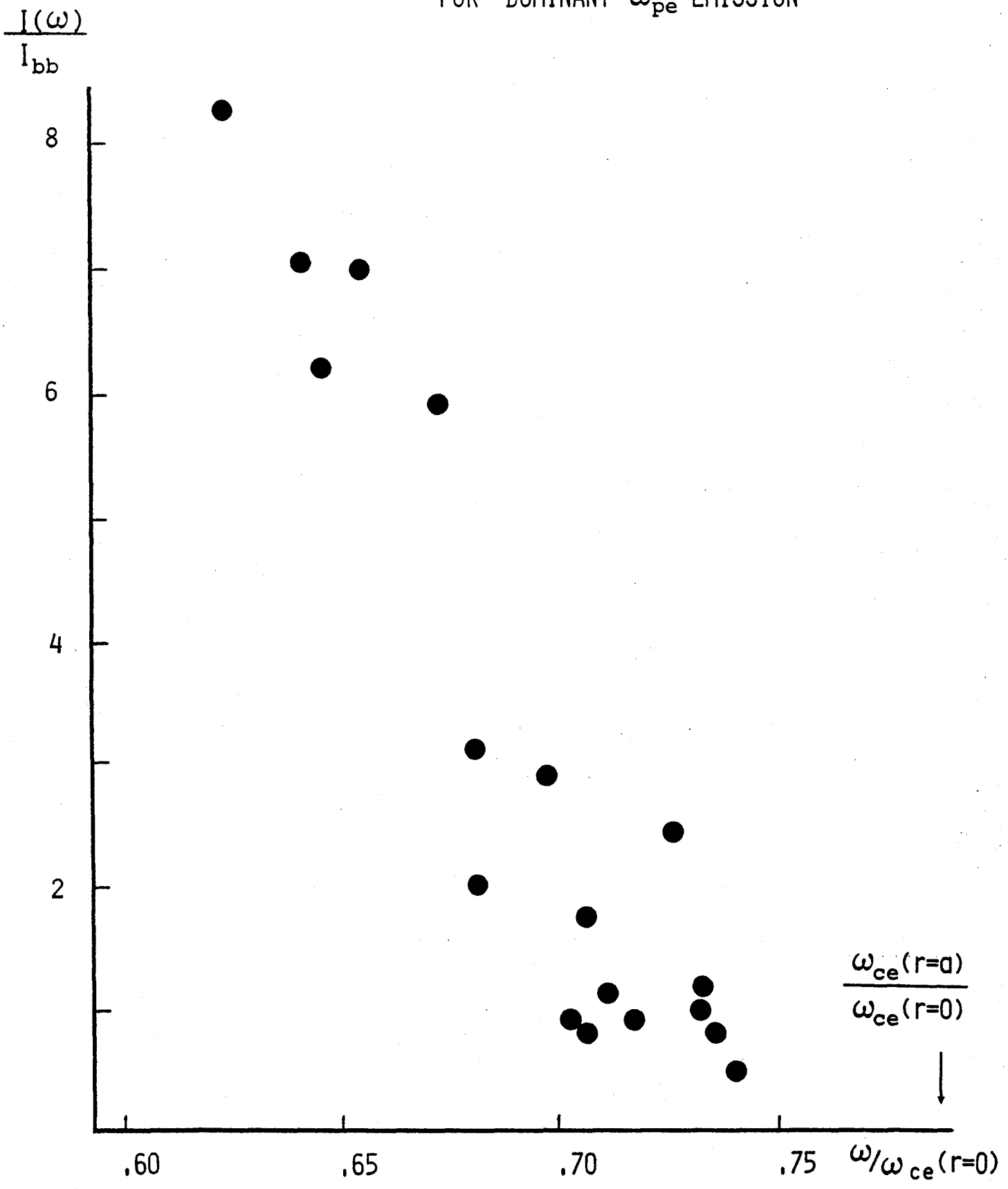

Fig.(4)
Data from repeatable discharges at 80 kGauss.

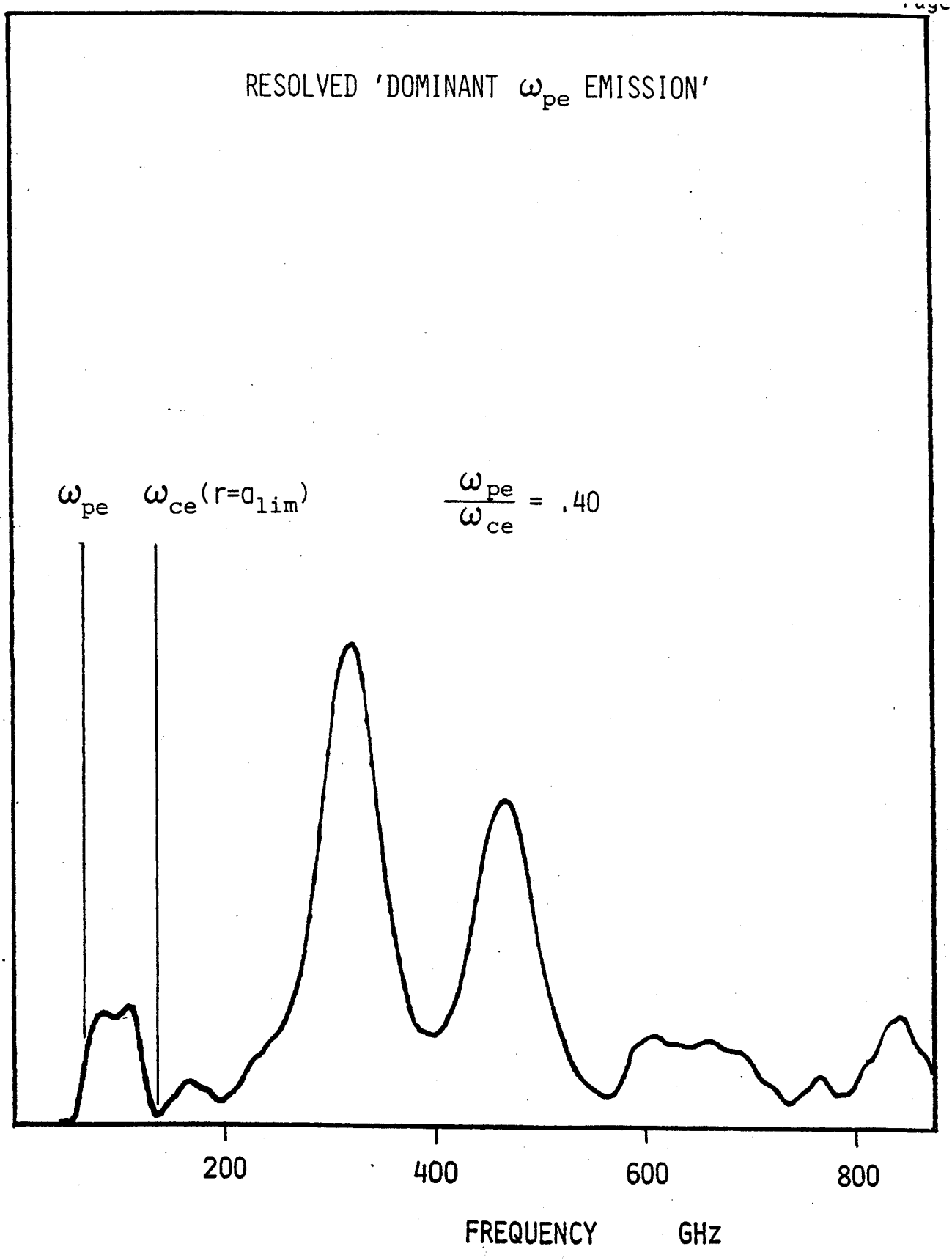

Fig.(5)
Extraordinary mode emission at 60 kGauss. The double humped feature of dominant emission is just being resolved. In these cases the intensity is reduced in comparison to previous examples.

REFRACTIVE INDEX vs. ANGLE
FOR FREQUENCIES NEAR ω_{pe}

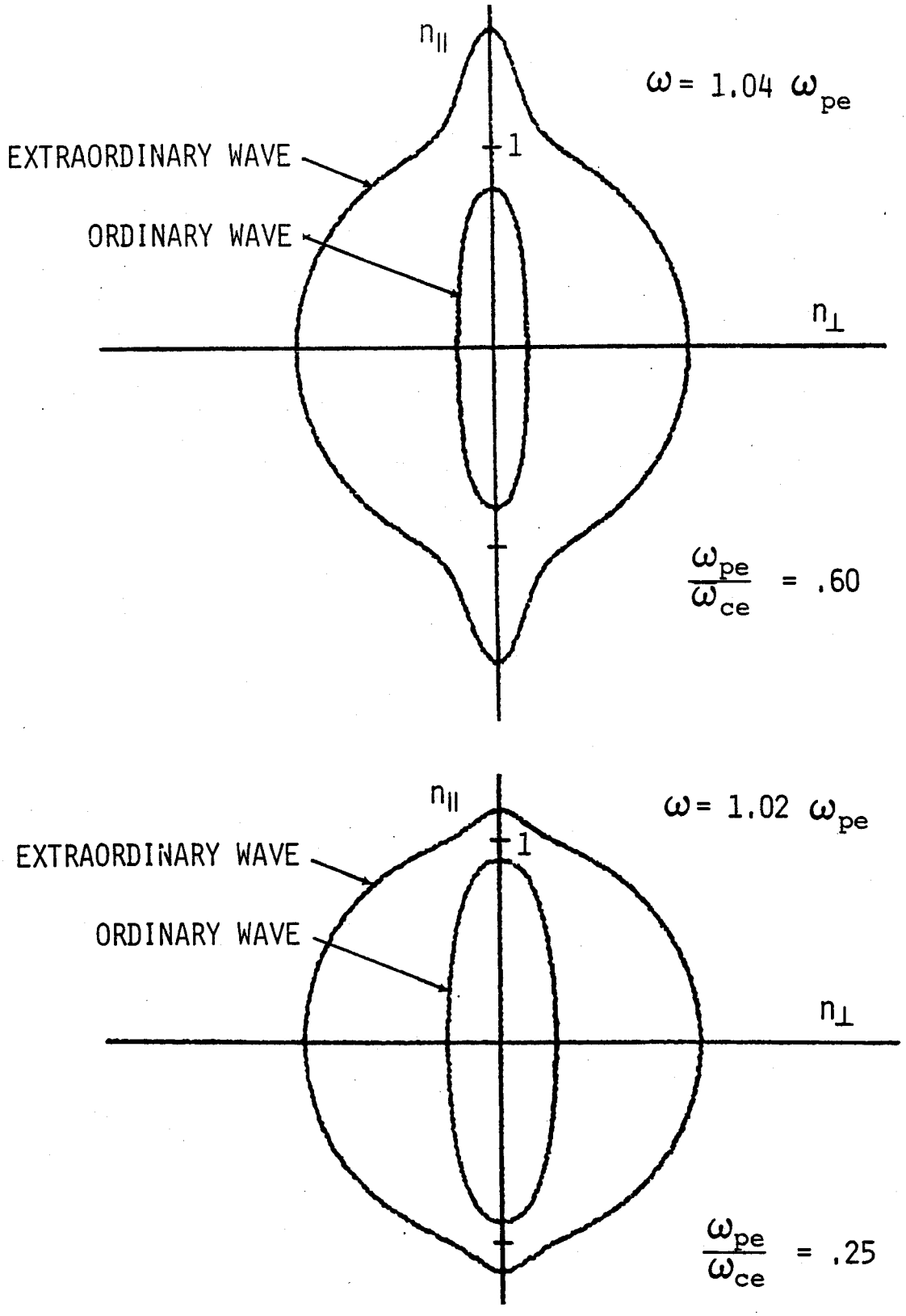

Fig.(6)
Only the extraordinary mode has phase velocity greater than the speed of light, particularly for propagation near to the field direction. Direction of group velocity is given by a normal

SEC 7.0 FLUCTUATING PLASMA FREQUENCY EMISSION

Another type of radiation observed from Alcator which is associated with non-thermal processes is termed 'fluctuating ω_{pe} emission.' It is characterised by an extremely narrow spectral feature, near the electron plasma frequency, which undergoes rapid temporal fluctuations. The intensity may exceed the combined radiation at the cyclotron harmonics by factors of ten or more. While sharing similarities with various experimental phenomenon and theories, the results from Alcator differ in some way from all of these. In this sense fluctuating wpe emission is a novel result not previously documented.

The fluctuating emission is present to some degree in nearly one half of all Alcator discharges. It has been observed from hydrogen, deuterium, and helium plasmas in toroidal fields from 40 to 100 KGauss. The emission usually occurs during the early portions of the discharge when conditions favour the production of runaway electrons. However, the fluctuation may reoccur during plasma termination or may persist throughout the discharge. The emission is usually not related with fluctuations of other diagnostic signals, such as current or density, however, occasional correlation with MHD activity suggests that such activity may be involved in the emission process.

The temporal behaviour of the fluctuating emission is best studied with a detector operating as a broadband monitor of submillimetre radiation. The large intensity of the feature makes it easily recognisable against the background level. While the Michelson

interferometer as previously discussed is not suited for the study of rapidly varying radiation, is does provide a limited amount of spectral information. A scanning Fabry-Perot interferometer is used to generate high-resolution spectra of the fluctuating feature.

SEC 7.1 TEMPORAL BEHAVIOUR

Examples of fluctuating ω_{pe} emission are shown in fig.(1), where the detector is operating in conjunction with the Michelson interferometer. The resulting interference structure is evident on the analog signal. Superposed upon this background the fluctuating emission appears as a series of high frequency bursts. The bursting begins shortly after ionisation and persists for about 50 msec. Comparison of these examples from consecutive discharges shows that varying levels of emission occur while macroscopic plasma parameters such as temperature, density, and current remain unchanged. As shown, the intensity of fluctuating emission can be associated with the flux of hard x-rays. This suggests participation of non-thermal electrons in the emission process, since hard x-ray emission requires the presence of non-thermal electrons and their collision with the limiter. The absence of hard x-rays alone does not guarantee lack of non-thermal electrons, however, during the first milliseconds of plasma discharge confinement of fast electrons will be poor, so that the presence of these particles and the subsequent hard x-ray activity can be related. The early portion of a discharge is shown in fig.(2). Fluctuating emission begins immediately after ionisation is completed and precedes the first intimations of x-ray flux by 1 msec. The loop voltage is a nearly constant 50 Volts and is capable of generating relativistic electrons in .5 msec.

A notable feature of fluctuating ω_{pe} emission is the regular periodicity with which the bursts of emission often occur. Fig.(3) show examples of such cases. Typically these fluctuations occur at rates of 5 - 20 kHz with a total duration of several dozen cycles. The fluctuation may cease at this time, or may continue with a new series of bursts. The fluctuations are best described as a series of narrow spikes spaced at regular time intervals, rather than by sinusoidal oscillations. The fluctuation spectrum produced by a frequency analyser[1] will incorporate the non-sinusoidal nature of the fluctuations by including overtones of the repetition rate. Harmonic structure on such a spectrum will reflect the structure of the bursts and not necessarily the periodicity with which the bursts occur. To measure just this periodicity, the time interval between spikes is averaged over a small number of cycles. A plot of this frequency during the time of emission is shown in fig.(4). As seen, the fluctuation frequency gradually decreases through the duration of emission. This property can only be observed when the emission persists for many oscillation periods and when the fluctuations are a series of periodic spikes.

Often the spikes occur at irregular intervals in which case there is no definite fluctuation frequency. Such cases may be explained by a superposition of several periodic fluctuations of differing frequencies. The justification of this supposition must await discussion of spectral measurements of the radiation frequencies.

SEC 7.2 CORRELATED BEHAVIOUR

If the plasma density is sufficiently low so that $\omega_{pe} < \omega_{ce}$, the fluctuating emission may be observed throughout the discharge, if it in fact happens at these times. When this occurs the temporal behaviour changes dramatically, and a correlation between emission and sawtooth disruptions becomes manifest. This correlation is shown in fig.(5) where the time surrounding several sawteeth is expanded. Whenever fluctuating emission is observed during the portion of discharges when sawteeth are present, it always appears in phase with the sawteeth. Like the previous examples the emission is a series of periodic spikes. However, they are fewer in number and are confined to a small time region surrounding the falling edge of the sawtooth. The number of spikes during a sawtooth cycle remains a constant over many sawtooth periods during a single discharge, but is observed to vary from one discharge to another. The fluctuation frequencies for sawtooth correlated emission are faster than the previous example. The highest fluctuation frequencies are associated with the the largest number of emission spikes. This is seen in fig.(6) where the fluctuation frequency is plotted against the number of spikes during one sawtooth period for a number of discharges. This may be interpreted as meaning the total time of emission is nearly constant so that higher rates will produce more spikes. However the faster rates are also associated with higher plasma density, suggesting that the frequency is somehow dependent on this or some associated plasma parameter.

A closer examination of the sawtooth correlations reveals that the onset of emission corresponds to periods of large m = 1 MHD oscillations which either precede or follow the sawtooth falling edge. The emission is also seen to occur during periods of m = 1 activity in the absence of sawteeth. This is shown in fig.(7), where it is evident that the radiation occurs in phase with the oscillations of the mode. These oscillations in the soft x-ray signals are thought to result from rotation, either poloidal or toroidal, of the perturbed q = 1 flux surface. The correlation of fig.(7) suggests that this phenomenon is also related to the emission process. Fig.(8) shows the time history of fluctuating emission from a single discharge, and displays a large variety of correlated emission behaviour. The first bits of emission are correlated with the small disruptions associated with the current rise phase. After this the emission continues at a fairly steady rate until m = 1 oscillations become evident on the soft x-ray trace. At this time the bursts of emission come in phase with these oscillations. Finally, once sawteeth become established the emission is confined to times near the falling edge when m = 1 is largest. Sawteeth and m = 1 activity are confined to the plasma region near the q = 1 surface. Because of the correlation with this activity the region of emission is probably also localised to the plasma centre.

SEC 7.3 COMPARISON WITH OTHER EXPERIMENTS

Fluctuating emission has also been observed from Alcator A. Although less carefully studied, the emission shows the same temporal behaviour as the Alcator C results, including correlations with sawteeth. Intense bursts of submillimetre emission have also been

observed from DITE[2] and Microtor[3], although it is unknown if these radiation events have the same character as the Alcator results. A consequence of the fluctuating emission is the rendering of interferograms useless, since the Fourier transform technique cannot deal with a rapidly fluctuating signal. Since the fluctuations usually occur briefly during the early phase of discharges, they do not ruin the more important (from a confinement study point of view) interferograms from the steady state portion. For this reason, measurements with Michelson interferometers may regard this fluctuating signal as a nuisance, or as 'noise' associated with ionisation, and ignored. A submillimetre experiment based upon a heterodyne detector, or monochromator, concerned with radiation at the second gyroharmonic will necessarily fail to detect plasma frequency emission. Furthermore, even if measured by a broadband detector, the fluctuating signal may not be noticed due to the format of data display and storage. For example, Alcator data is digitised for archival purposes at an effective rate of 3 kHz, making it useless for the study of the much faster fluctuating emission.

SEC 7.4 REFERENCES & FIGURES

1.) I.H. Hutchinson, S.E. Kissel
Phys. Fluids 23 1698 (1980)

2.) A.E. Costley Private Communication

3.) R.J. Taylor Private Communication

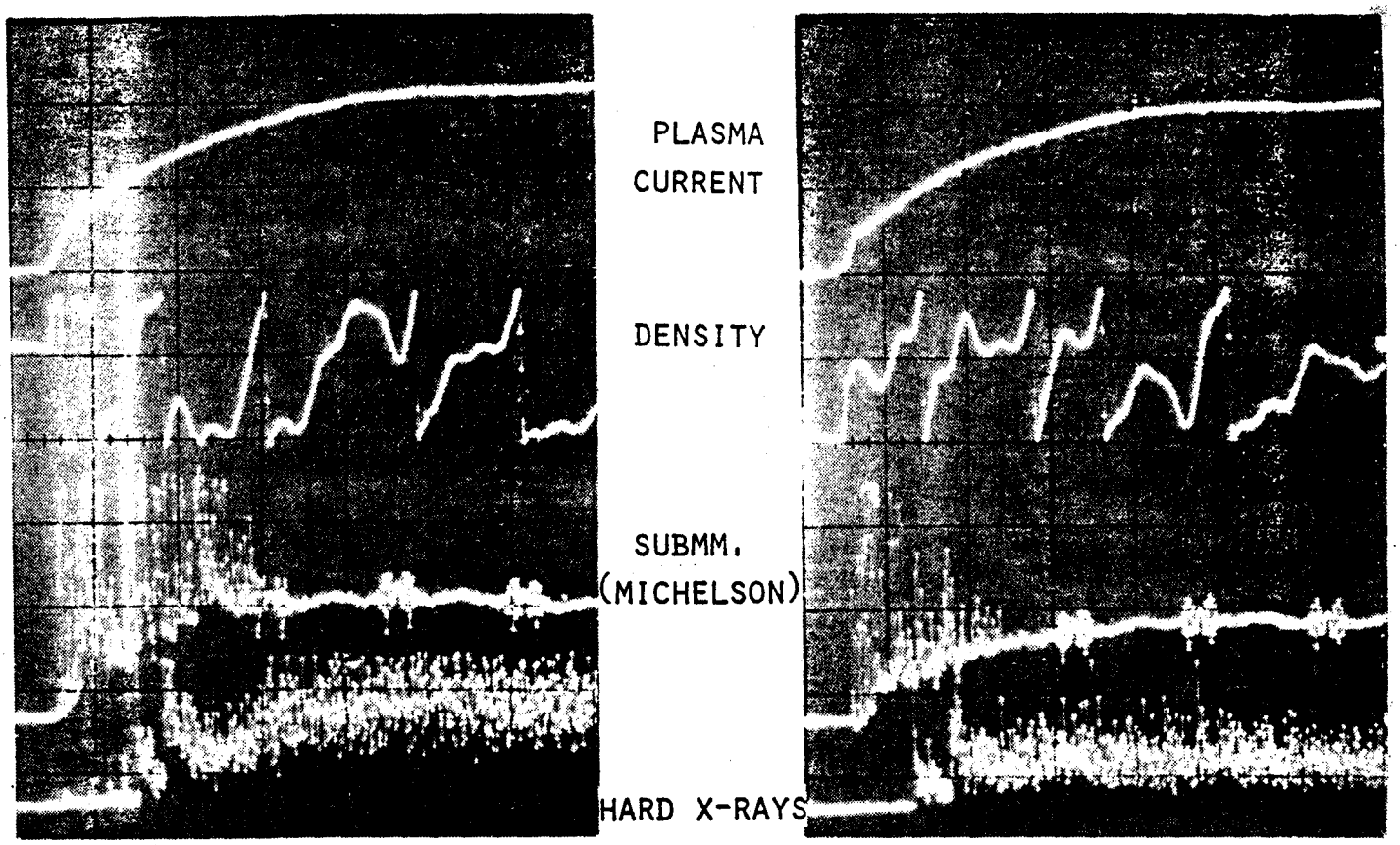

20 MSEC/DIV.

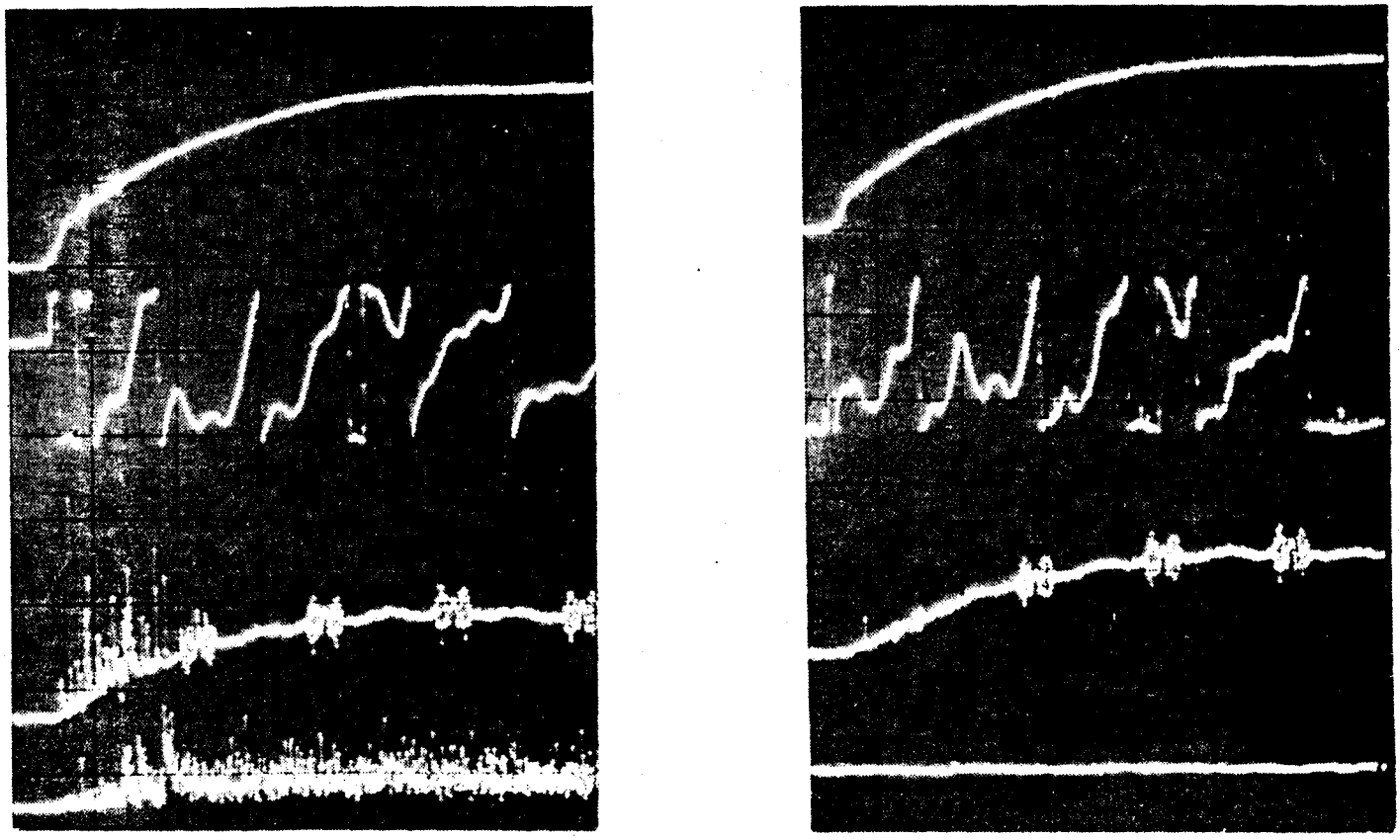

Fig.(1)
Discharges in Hydrogen at 60 kGauss from same run.
All pictures have the same scale.

ONSET OF 'FLUCTUATING ω_{pe} EMISSION'

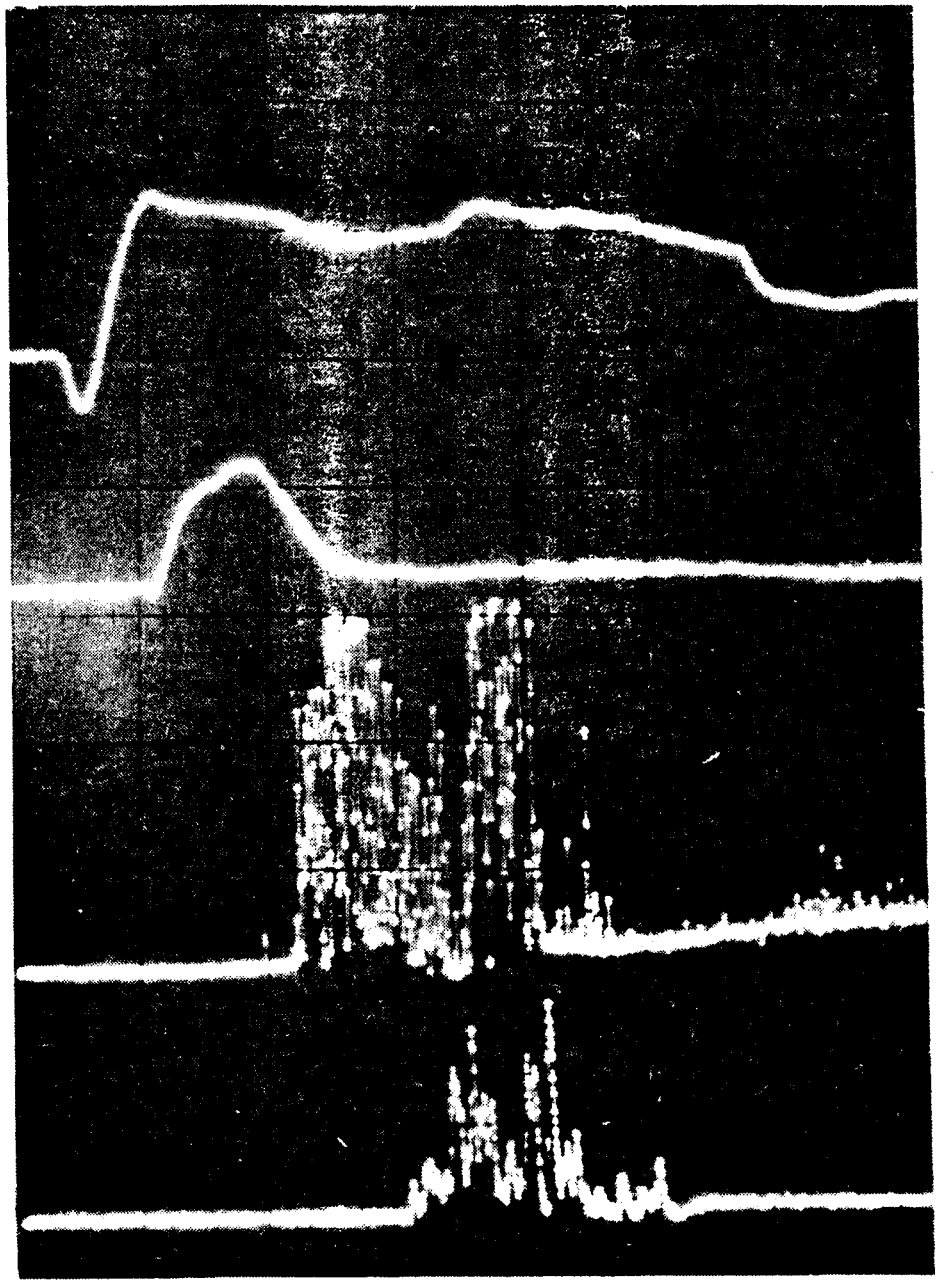

Fig.(2)
Ionisation begins 1 msec from the left edge. Visible light results from molecular and hydrogen line emission. Decrease in visible light signal indicates complete ionisation.

PERIODIC BURSTS OF 'FLUCTUATING ω_{pe} EMISSION'

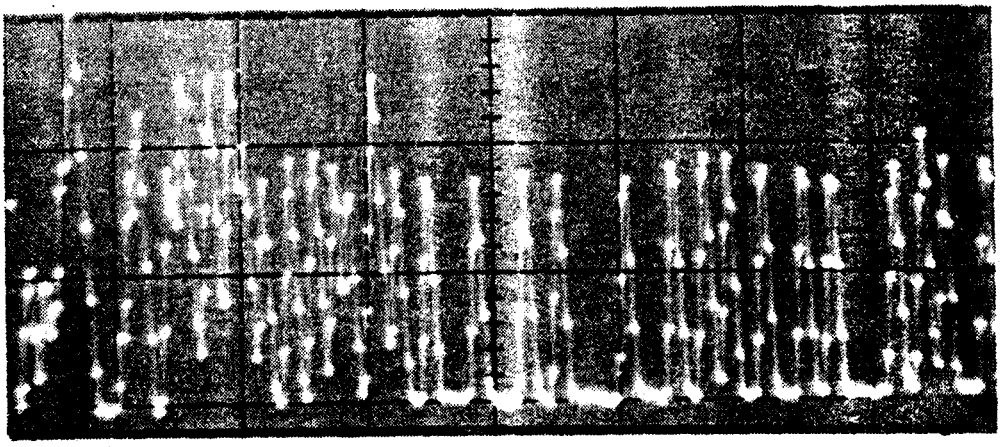

.1 msec/div Ave. fluctuation rate = 40 kHz

central density = 3.0 10^{13} cm^{-3}

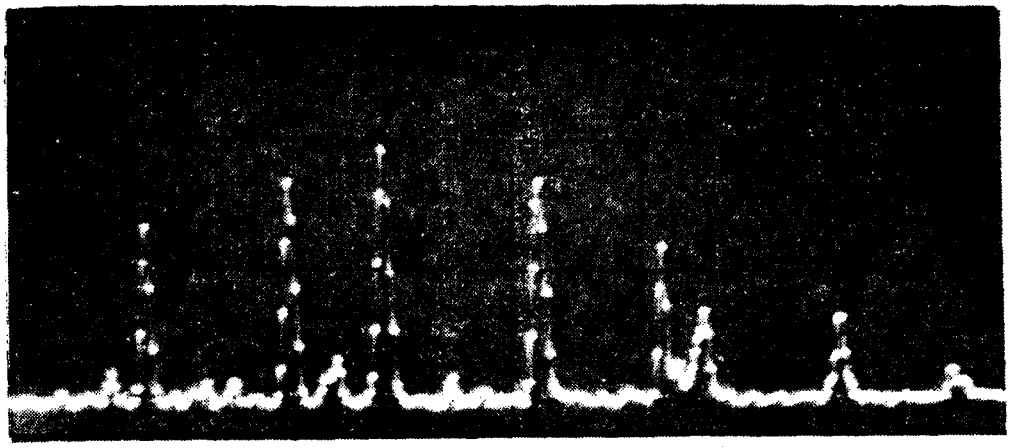

.1 msec/div Ave. fluctuation rate = 10 kHz

central density = 1.9 10^{13} cm^{-3}

Fig.(3)

A general trend is that higher average fluctuations occur with increased density. However, the rate tends to decrease in time for a sequence of bursts. This is noticeable in the top example.

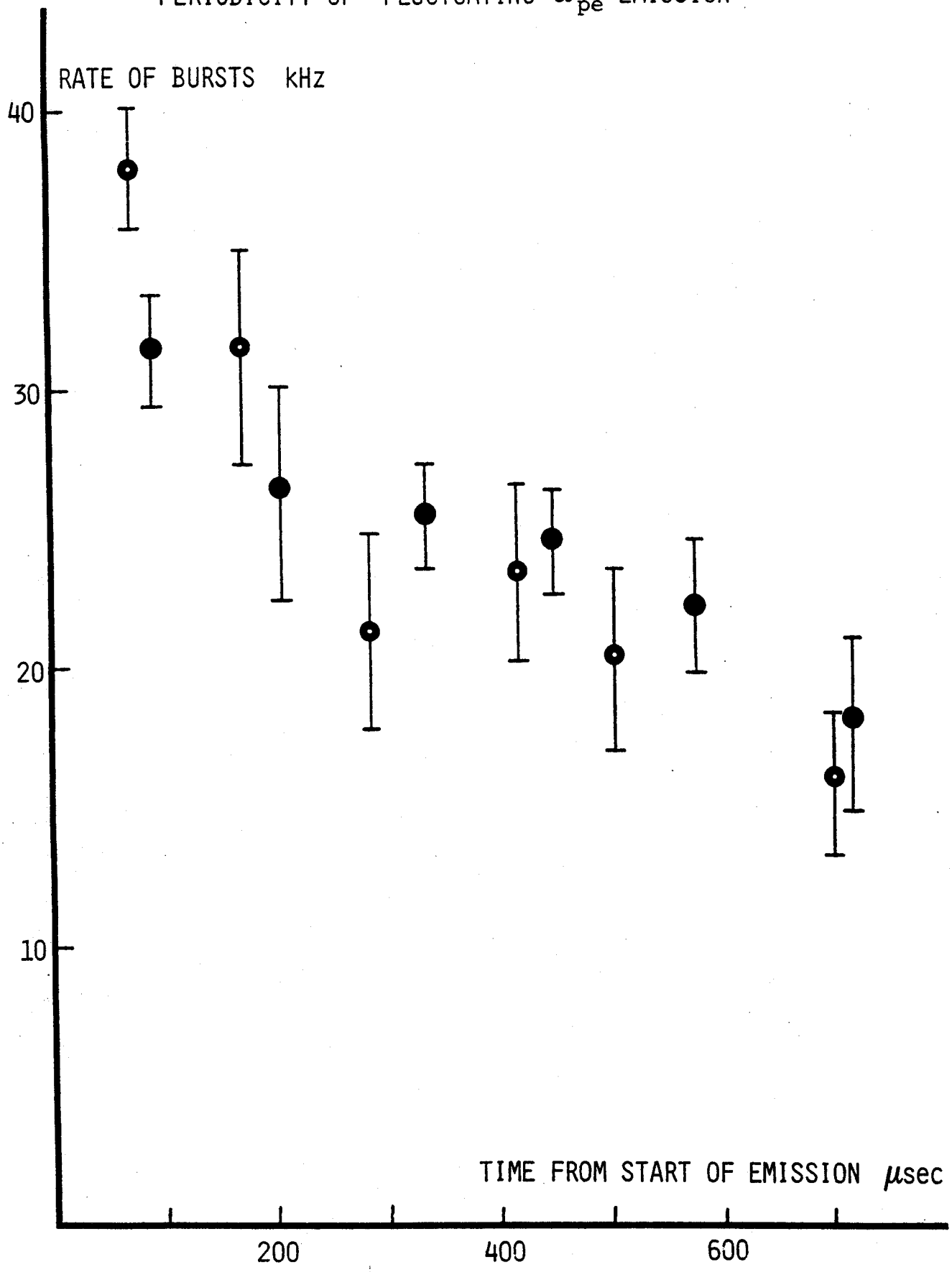

Fig.(4)
Data from two sequences of periodic bursting emission from single discharge in Deuterium at

EXAMPLES OF 'FLUCTUATING ω_{pe} EMISSION'
CORRELATION WITH SAWTEETH

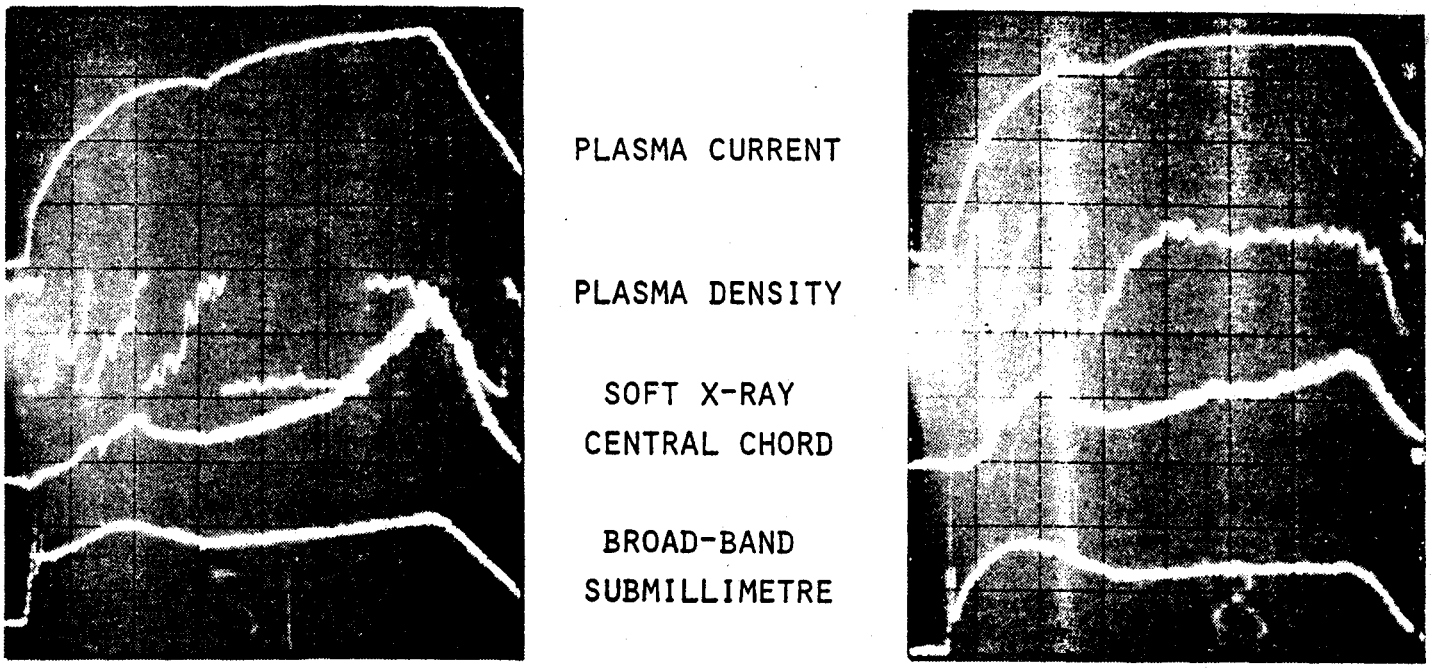

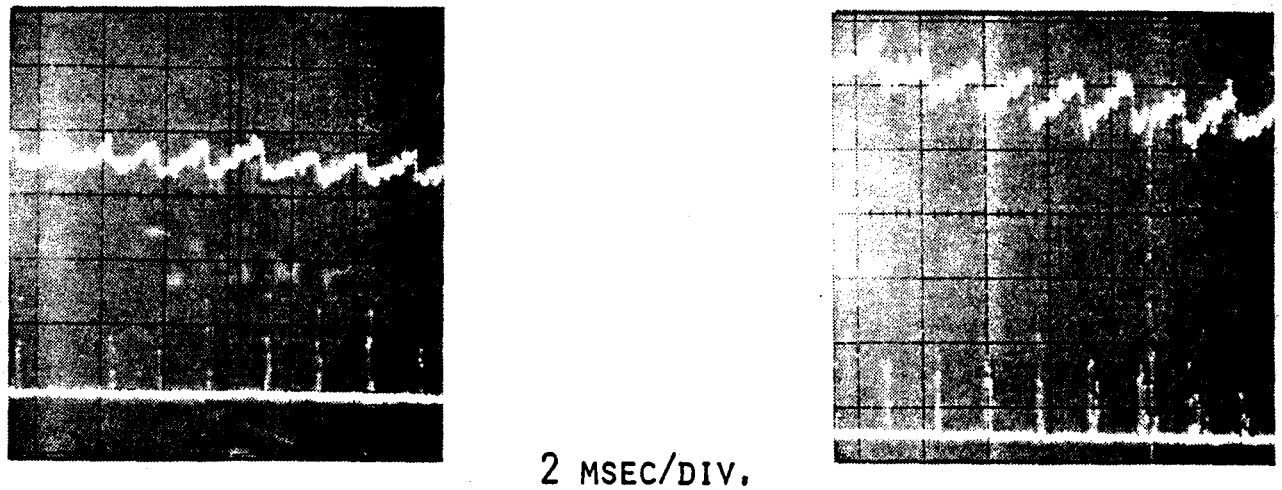

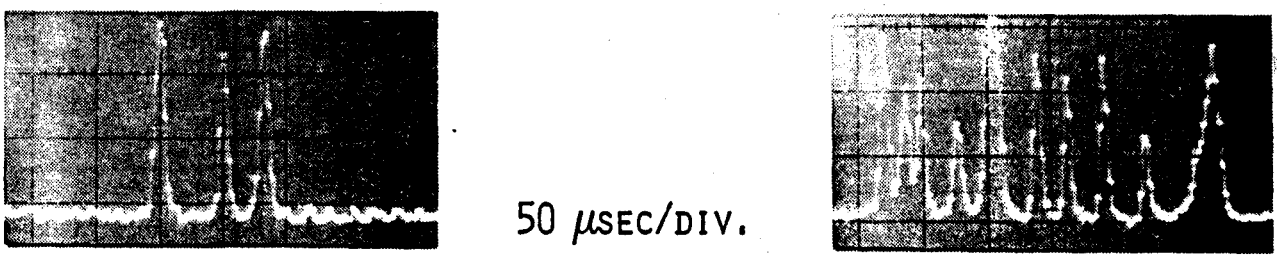

Fig.(5)
Successive expansions of two discharges in Hydrogen at 60 kGauss; left $n_e = 7.3\times10^{13}$ cm^{-3}, right $n_e = 1.5\times10^{14}$ cm^{-3}

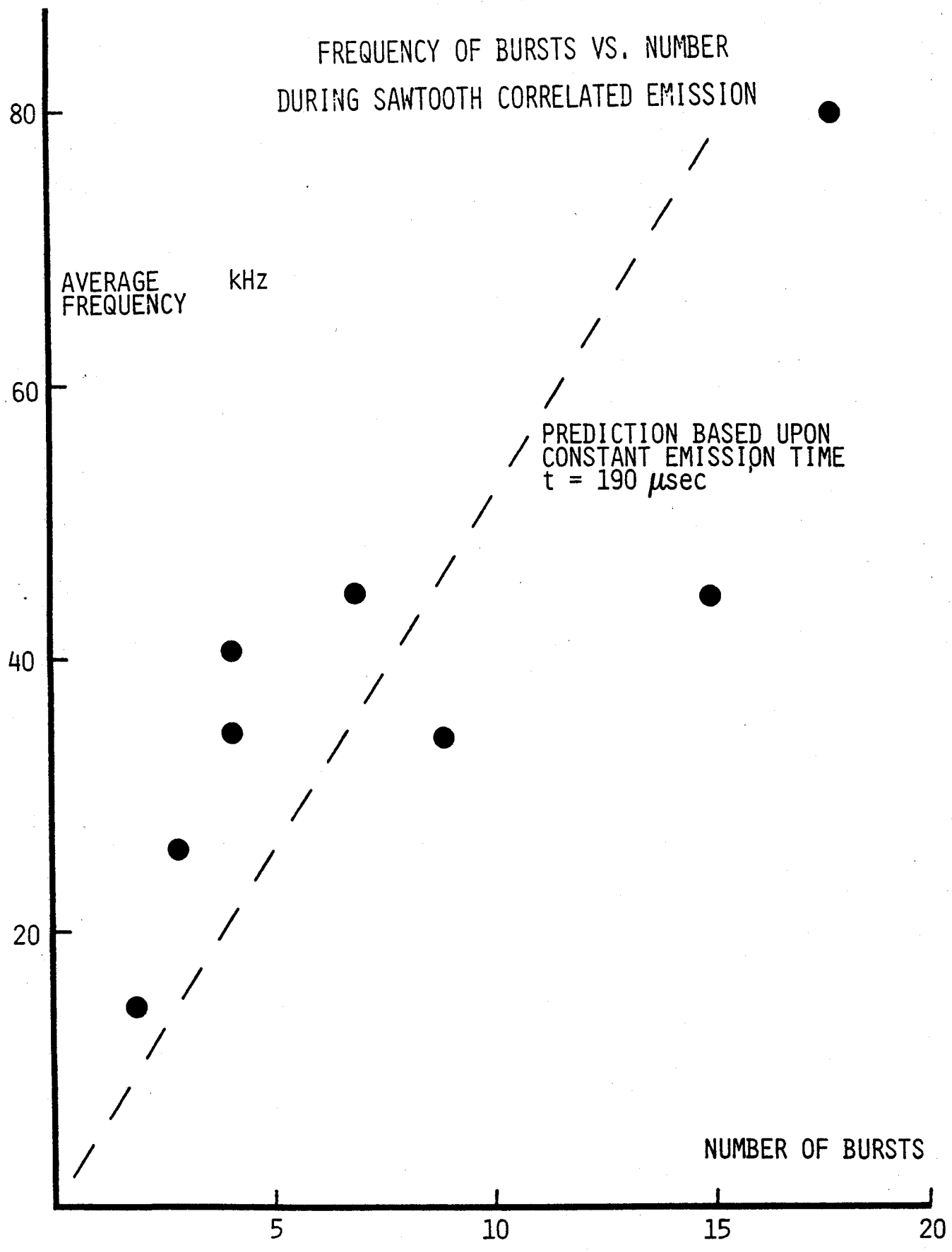

Fig.(6)
Data from cases such as previous figure. Line is least square fit with forced zero intercept.

CORRELATION OF 'FLUCTUATING ω_{pe} EMISSION'
WITH m=1 OSCILLATIONS

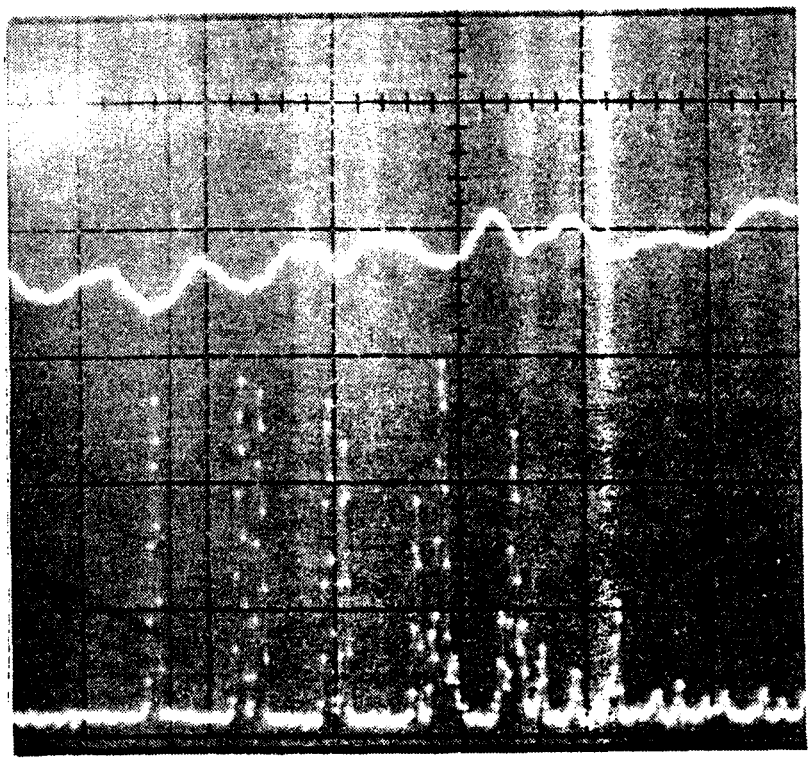

Fig.(7)
The oscillations in the x-ray signal correspond to rotation of the m=1 mode. Bursts of wpe emission occur in phase with this rotation.

EVOLUTION OF 'FLUCTUATING ω_{pe} EMISSION'
CORRELATION WITH MHD ACTIVITY

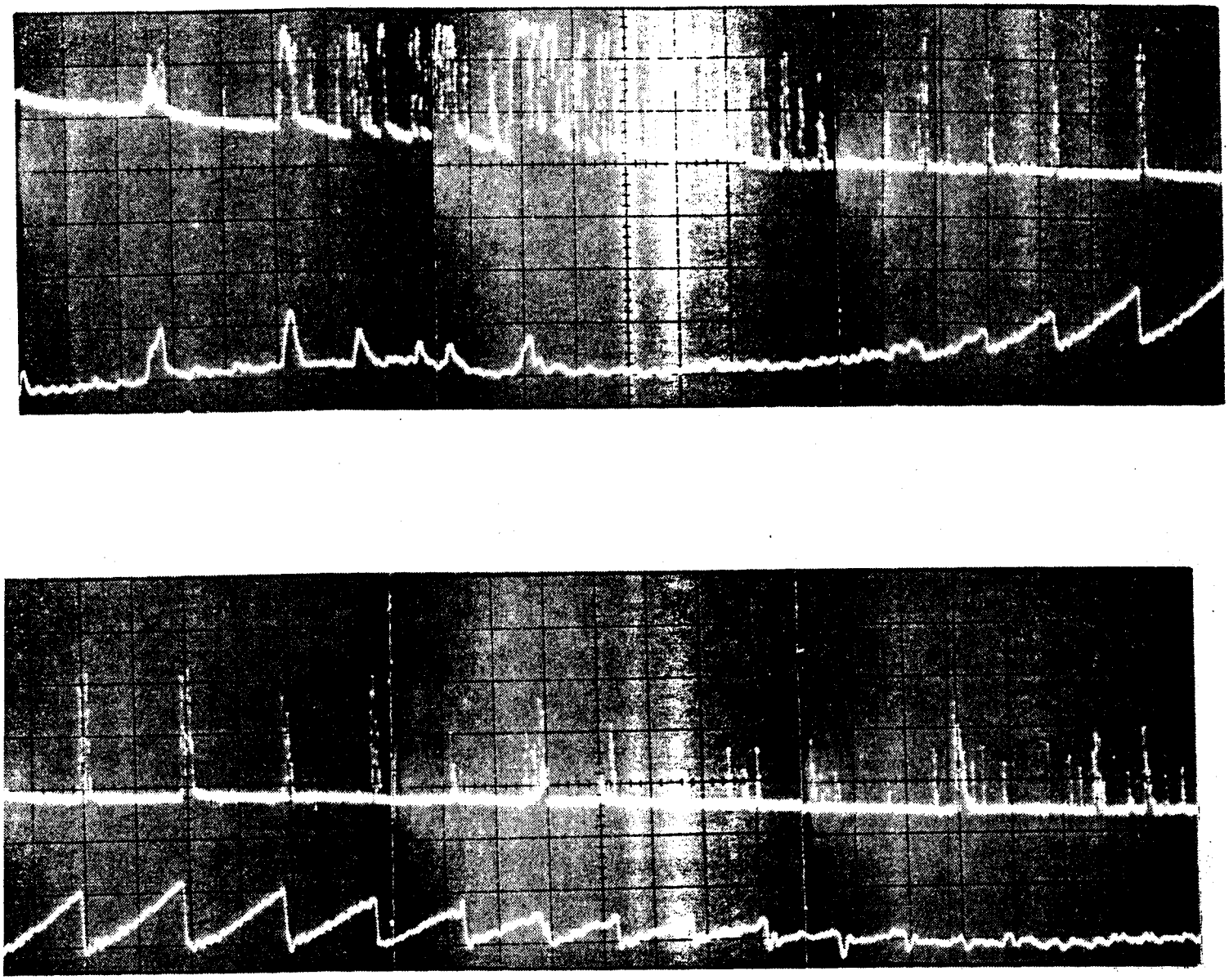

UPPER TRACE: BROAD-BAND SUBMILLIMETRE

LOWER TRACE: SOFT X-RAY CENTRAL CHORD

1 MSEC/DIV.

Fig.(8)
Continuous picture of discharge starting 50 msec after ionisation.

SEC 8.0 SPECTRAL MEASUREMENTS OF FLUCTUATING EMISSION

Spectral measurements of the fluctuating ω_{pe} emission show that radiation occurs in an extremely narrow bandwidth near the central electron plasma frequency. The spectral narrowness of the fluctuating emission distinguishes it from the broader radiation feature discussed in Sec.(6). Because of the novelty of the fluctuating emission a detailed account of the techniques and results of spectral measurements will be presented in this section so that meaningful comparison with other experimental results and discussion of various theoretical interpretations can be made.

SEC 8.1 MICHELSON INTERFEROMETER

As mentioned in sec (5) the Michelson interferometer is not well suited for the study of signals which vary during the 10-15 msec sweep time of the vibrating mirror. This is not because the system is insensitive to more rapid fluctuations, but due to the false interpretation of these temporal fluctuations by the Fourier transform routine as resulting from the changing path difference of the instrument. In the case of sawtooth or loop voltage induced oscillations, the amplitude of fluctuation is small enough so that the effect on the generated spectra is very small. However, because the fluctuating ω_{pe} emission is many times larger in intensity than the thermal background the effect upon the resulting spectra is catastrophic. Even when the interferogram is smoothed prior to the Fourier transform the spectrum is usually dominated by unreal noise features resulting from the sudden bursts.

Fortunately it is not necessary to Fourier transform the Michelson interferometer signal in order to recover information concerning the incident radiation. Fig.(1) is an example interferogram occurring during a period of fluctuating emission. In addition to the characteristic 10 KHz spiking there is a slower signal modulation resulting from the action of the interferometer. That this effect is not the manifestation of a peculiar time history of emission can not be demonstrated by a single example. However repeated observations bear out the contention that this modulation effect is indeed caused by the interferometer. In this example, the minima occurring at approximately 1.8, 3.5, 4.9, 6.3, 7.6 msec after the zero path difference correspond to situations where the path differences are integral multiples of the emission wavelength(s). Since these conditions, $\Delta x_j = N_j L$, can be satisfied for only a single wavelength, the recurring minima imply that the fluctuating emission must be restricted to an interval about a single frequency. As the mirror motion is nearly sinusoidal with known amplitude and period, the observed minima can be converted to a radiation frequency. In this case the indicated frequency is about 100 GHz, which compares favourably with the expected central plasma frequency.

The persistence of the modulations throughout the interferogram is a reflection of the spectral narrowness of the radiation. A feature will no longer produce coherent interference when the path difference is equal to the inverse of the frequency spread of the feature: $\Delta X = c/\Delta\nu$. Thus by measuring the 'coherence length' of the interferogram the spectral width of the feature can be determined. This technique was employed in the 19th century by Fizeau[1] and others

to measure widths of optical lines resulting from atomic transitions. A similar attempt to measure the coherence length of the fluctuating emission is restricted by the mechanical limitations of the instrument, however an upper limit of 5 GHz can be assigned to the bandwidth of the emission feature.

SEC 8.2 FABRY-PEROT SYSTEM

In order to investigate any spectral structure of the fluctuating ω_{pe} feature it is desirable to obtain higher resolution spectra than the Michelson allows. As an example, for reasons discussed in sec (9) the emission might be expected to occur as the doublet $\omega_{pe} \pm \omega_{pi}$ where ω_{pi} is the ion plasma frequency. For Alcator conditions ω_{pi} is approximately 1 to 2 Ghz, which is smaller than the resolution capability of the Michelson. High resolution spectral measurements are made with a rapid scan Fabry-Perot interferometer system. Because this device is not a standard instrument it is necessary to describe its operation before a presentation of resulting measurements can be undertaken.

The experimental arrangement of the Fabry-Perot interferometer system is shown in fig.(2). Radiation from the Tokamak follows the same optical path described in the appendix, and is incident upon a wire mesh polariser which splits the signal between two detectors. This polariser is oriented to couple equal amounts of both polarisations to each detector. One of these detectors is a broadband monitor having a nearly constant response from 50 to 200 GHz. The radiation coupled to the second detector must first pass through the Fabry-Perot etalon which transmits only specific frequencies. The

etalon is similar to that described in sec (5), and consists of two wire meshes of 100 lines per inch mesh constant. One mesh is statically mounted on a moveable stage, the other on the dome of a loudspeaker[2]. When the loudspeaker is driven the separation between the two meshes varies with time in a sinusoidal manner. Typically the loudspeaker is driven at 110 Hz with an oscillation amplitude of ± .3mm. Thus the etalon can be swept over a small frequency range, for example from 54 to 68 GHz. The location of this range can be varied by adjusting the position of the static mesh with respect to the loudspeaker dome. During operation the system generates three signals, one from each of the two detectors and a third which serves as a position monitor for the moving mesh. In order to make any sense from these signals it is necessary to know how the transmitted frequency is related to the position monitor signal. It is also important to know the frequency resolution of the instrument.

This calibration is made with an 83 GHz klystron radiation source. Fig.(3) shows such a calibration. By varying the location of the static mesh with respect to the moving mesh and noting the changing location of the 83 GHz signal with respect to the position monitor signal, an accurate calibration of the position monitor signal is made, thus allowing the conversion of this signal to transmitted frequency. The position monitor signal is nearly proportional to the mesh separation, though a small phase shift must be included. The frequency resolution is measured by noting the width of the 83 GHz line. The line width of the source can be neglected so that the measured width results entirely from the finite resolution of the instrument. The measured finesse of 114 at 83 GHz is in agreement

with calculated values[3]. When measurements are made at frequencies other than 83 GHz it assumed that the finesse is proportional to the square of the wavelength as dictated by theory and experiment.

The relative spectral shape of the emission feature is determined by the ratios of the signals obtained from the two detectors. It is not necessary that the two detectors have the same response, only that their responses be in the same proportion at all frequencies. The measured spectra will be independent of temporal fluctuation since both detectors will be effected equally and the fluctuation will be lost when the ratio is taken. Because the Michelson results show the fluctuating emission to be quite narrowband, radiation passing through the Fabry-Perot can be assumed to occur in the first order of transmission only. The signal intensities are measured with respect to any existing baseline so that non-fluctuating thermal components will be ignored.

SEC 8.3 HIGH-RESOLUTION SPECTRA

Examples of the three signals from the Fabry-Perot system during the occasion of fluctuating emission are shown in fig.(4). This period occurs 10 msec from the initiation of the plasma discharge. During this interval the mesh motion corresponds to a frequency sweep starting at 50.5 GHz and increasing to 60.5 GHz. While the broadband fluctuating signal remains nearly constant, the Fabry-Perot signal shows a maximum of transmission indicating that during this time the etalon sweeps through the emission feature. This is shown clearly in the expansion of the region of emission in fig.(4). It should be mentioned that a good bit of chance is involved in making these

measurements. Since the frequency region to be scanned must be preselected, one must wait for the necessary conditions of plasma density and presence of fluctuating emission in order to measure the spectra.

The relative spectrum obtained from this example by dividing the Fabry-Perot signal by the broadband signal is plotted as a function of frequency, determined from the calibrated position monitor, in fig.(5). The spectrum shows an unambiguous transmission feature of very narrow bandwidth. The scatter of the plotted points arises primarily from uncertainties in reading the positions and amplitudes of the various bursts of emission. However, since it is assumed that the radiation frequency of the emission remains constant during the sweep time, the scatter might also result partially from small changes in the frequency. The residual level in the wings of the transmission feature is due to leakage of radiation around the etalon, so the baseline level should be regarded as slightly positive to compensate for this problem. The resolution corresponding to the FWHM of the Fabry-Perot is indicated on the spectrum and is such that the feature is regarded as being unresolved.

The electron density at which the plasma frequency equals the measured frequency of 54 GHz is $3.6\ 10^{-13}\ cm^{-3}$. The line averaged density is about $2.8\ 10^{-13}\ cm^{-3}$ and is rising rapidly at this time. If the radiation is assumed to occur at the central plasma frequency, a peak to averaged density ratio of approximately 1.6 is required. This is not too far from the typical measured values of 1.3, particularly when the relative accuracy of the line averaged density at these small values is considered. Because accurate values of

central density are not available, it can not be demonstrated conclusively that the emission does occur at the central plasma frequency. However, no examples have been found where the measured frequency of emission is not consistent with such an assumption. The emission frequency conceptually provides a sensitive measure of the plasma density since the instrumental resolution of 0.2 GHz translates to density changes of typically 1%. The absolute accuracy of this technique hinges upon the association of the radiated frequency with the central plasma frequency.

Occasionally the emission feature is observed to occur without the characteristic fluctuating behaviour. Fig.(6) illustrates the situation where a non-fluctuating type of emission is encountered by the Fabry-Perot system. The shape of the spectrum is directly shown by the transmitted signal. Once again the feature is unresolved, although it appears broader because of the reduced instrumental resolution at higher frequency. Whenever these non-fluctuating varieties are measured, the signal intensity is less than the fluctuating case, but they have the same narrow spectral shape as their namesake.

SEC 8.4 SHIFTS IN EMISSION FREQUENCY

The assumption that the radiation frequency remains relatively constant is necessary because the Fabry-Perot requires a finite time to sweep through a frequency interval. The required time is never more than a few msec, which is small in comparison to the time scale of density changes. Because of this it is not likely that variations in plasma frequency caused by density changes will have an effect upon

the measured spectra.

There is evidence of sudden change in radiation frequency of successive bursts of fluctuating emission. Fig.(7) shows such an example. The broadband signal shows a series of individual bursts of radiation, most of which belong to a sequence of evenly spaced spikes. In addition there are a few spikes which occur outside this sequence. The Fabry-Perot signal shows the transmission of the sequential spikes, but also shows that the additional spikes are not transmitted. The situations are indicated where two successive bursts occur, but only the one belonging to the evenly spaced sequence is transmitted. The frequency content of these bursts must differ by at least the instrumental resolution, which is 0.3 GHz for this example. Besides demonstrating sudden shifts in radiated frequency fig.(7) also suggests a connection between radiation frequency and the periodicity of temporal fluctuation.

It is difficult to make good spectral measurements of cases where the bursts are regularly spaced and few in number. This is because the peak spectral frequency will most likely be swept through during an interval between bursts, and the few points obtained will occur in the wings of the line. In cases such as fig.(4) where the bursts are irregularly spaced but much denser in time this problem does not happen. However, if the radiation frequency is changing in time it will not be so easily noticed in these cases. If the situation of irregularly spaced bursts is treated as the superposition of sets of periodic bursts, each with different periodicity, each set may have assigned to it a different radiation frequency. Thus the spectrum shown in fig.(5) may be some average of many frequencies.

The problem of changing frequency makes it difficult to be certain that in every case the spectrum is instantaneously very narrow. However, no apparently broad spectral features have been observed which could not be attributed to frequency changes during the scan time.

Because the two detectors are coupled to each mode of polarisation equally, the situation shown in fig.(7) can not result from a polarisation effect; such as the two successive bursts occurring in different polarisations. Polarisation measurements of fluctuating emission show no clear preference of mode, nor any evidence of sudden changes in polarisation. The measured intensity is always nearly equal in each mode. The polarisation of the emitted radiation is unknown. Because of the large effects of diffraction and reflection at these wavelengths it would be imprudent to assume that the absence of measured polarisation at the detector implies the similar situation at the region of emission within the plasma.

SEC 8.5 REFERENCES & FIGURES

1.) H. Fizeau
Ann. Chim. Phys. 66 429 (1862)

2.) D.S. Komm, R.A. Blanken, P. Brossier
Applied Optics 14 460 (1975)

3.) Renk & Genzel

MODULATION OF 'FLUCTUATING ω_{pe} EMISSION'
BY MICHELSON INTERFEROMETER

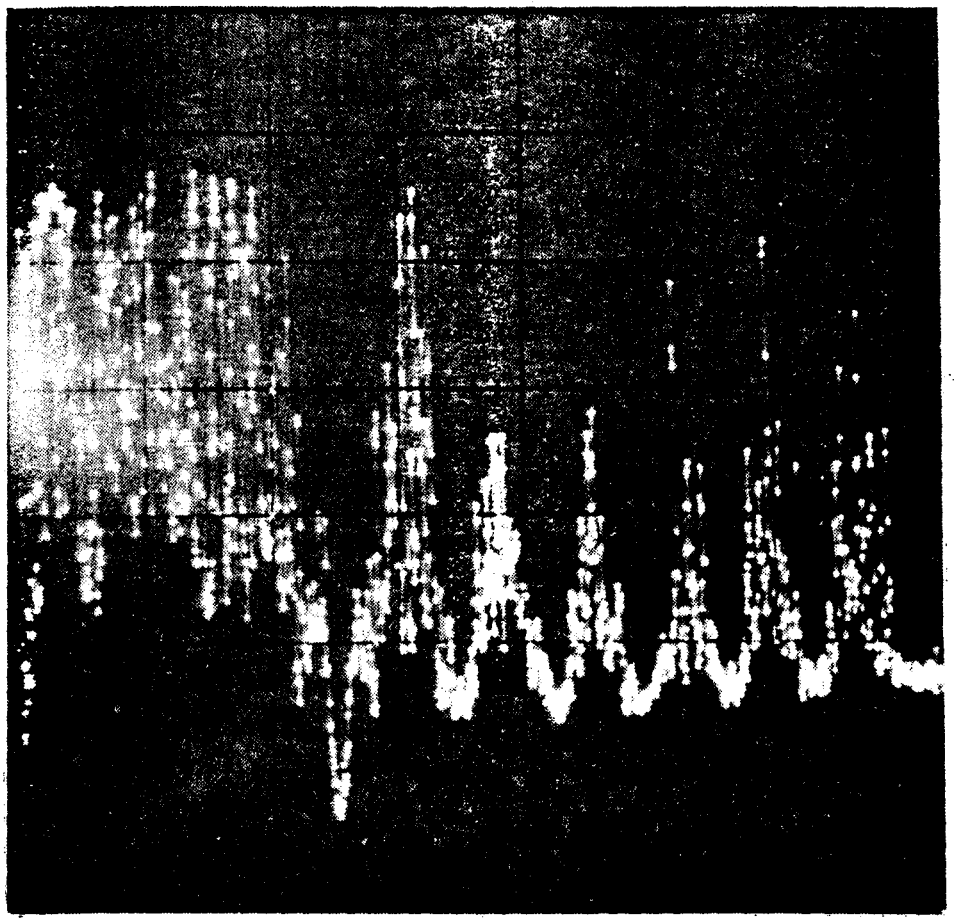

↑

2 MSEC/DIV.

Fig.(1)
The indicated point is the zero path difference of the Michelson interferometer. Extremes of mirror vibration occur 3 msec prior to and 12 msec after this time.

SCHEMATIC DIAGRAM OF FABRY-PEROT SYSTEM

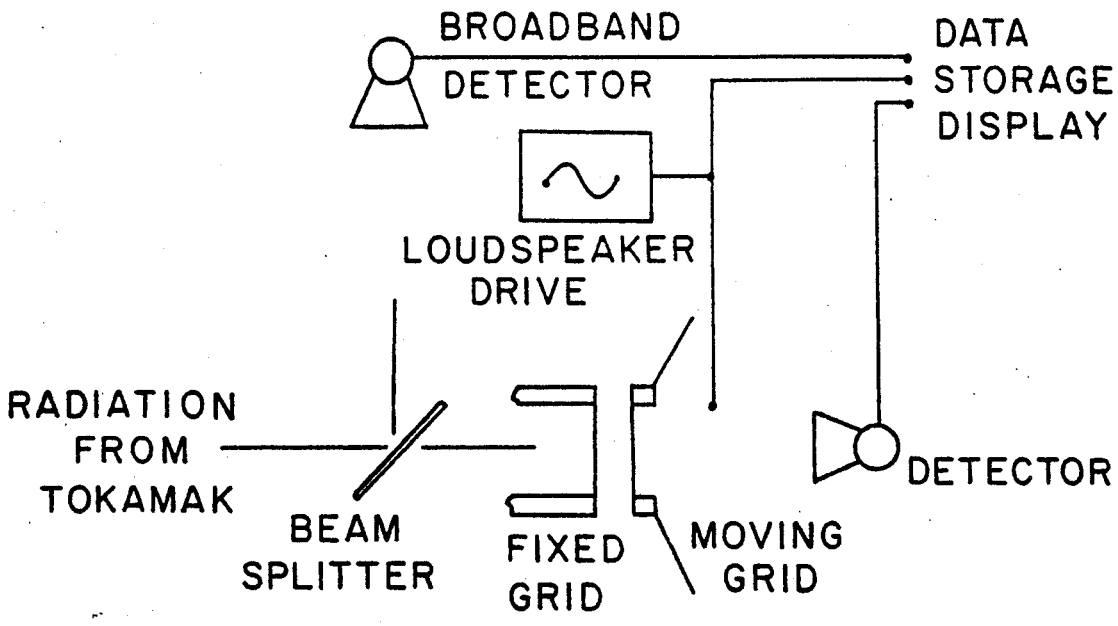

* DETECTOR: InSb crstal at 4.2° Kelvin
* MESH : 100 lines per inch electroform copper
* DRIVE : 110 Hz amplitude = $\pm$ .3 mm
* FINESSE: 114

Fig.(2)

CALIBRATION OF FABRY-PEROT SYSTEM
WITH 83.5 GHz KLYSTRON

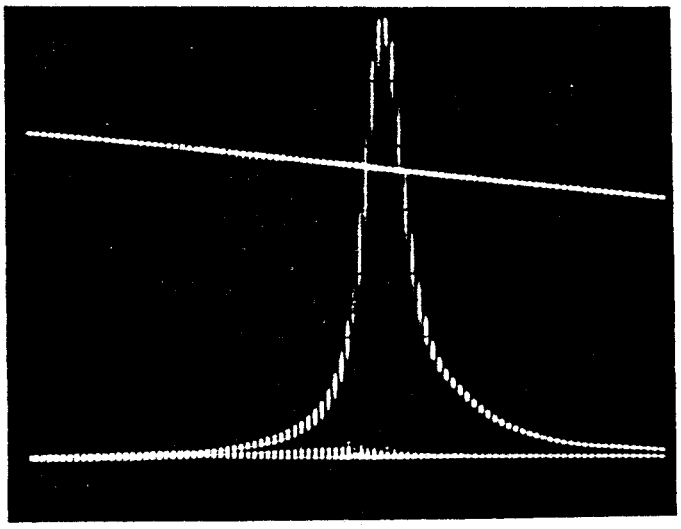

1 msec/division

Fig.(3)
The upper trace is the Fabry-Perot position monitor, the lower trace is the transmitted klystron radiation. The appropriate horizontal scale is 1 GHz/division. This implies a FWHM of 0.73 GHz, or a finesse of 114.

'FLUCTUATING ω_{pe} EMISSION'
EXAMPLE SIGNALS FROM FABRY-PEROT SYSTEM

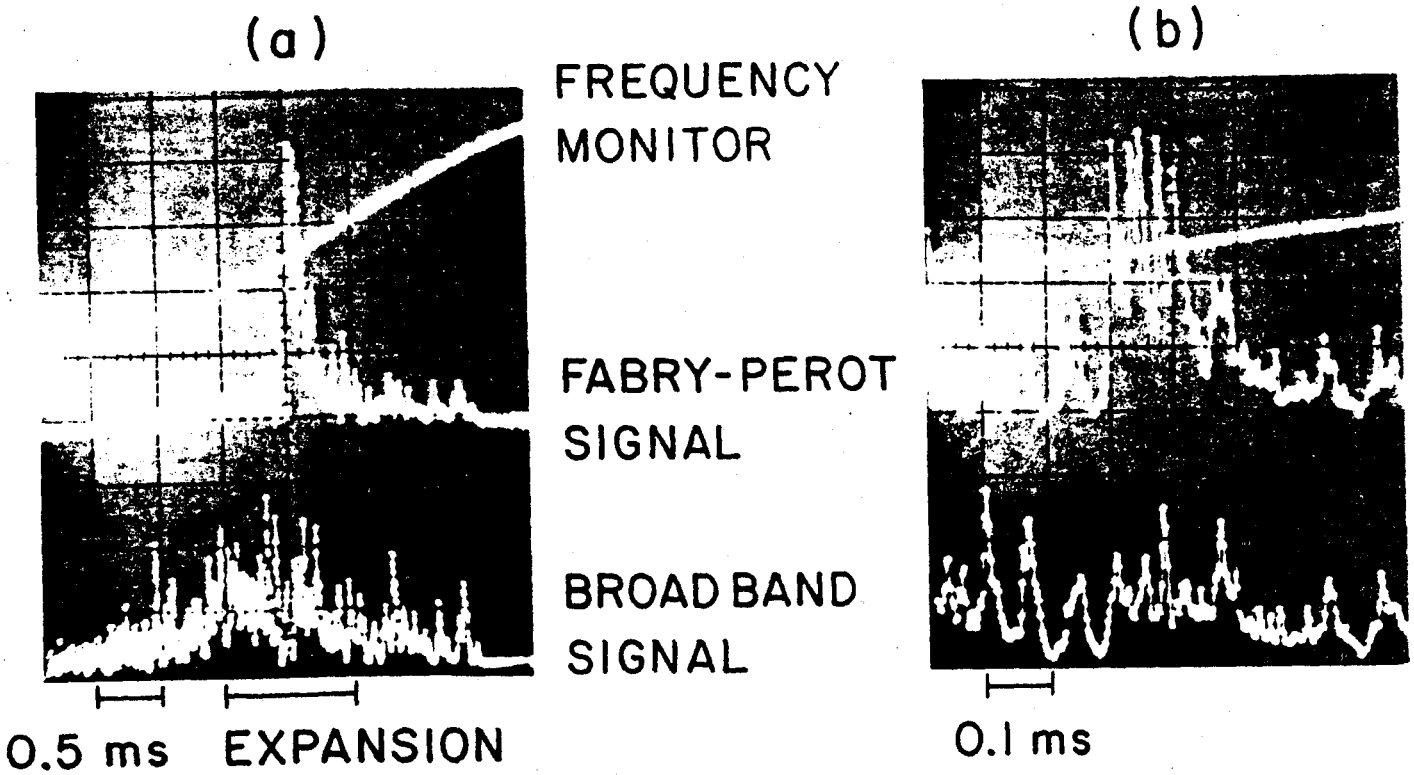

Fig.(4)
Emission from Hydrogen plasma in 60 kGauss magnetic field.
Density = 2.8×10^{13} cm^{-3} line average;
Current = 120 kAmperes at time of emission. a.) The Fabry-Perot is sweeping from 50.5 to 60.5 GHz left to right. b.)an expansion about the region of maximum transmission.

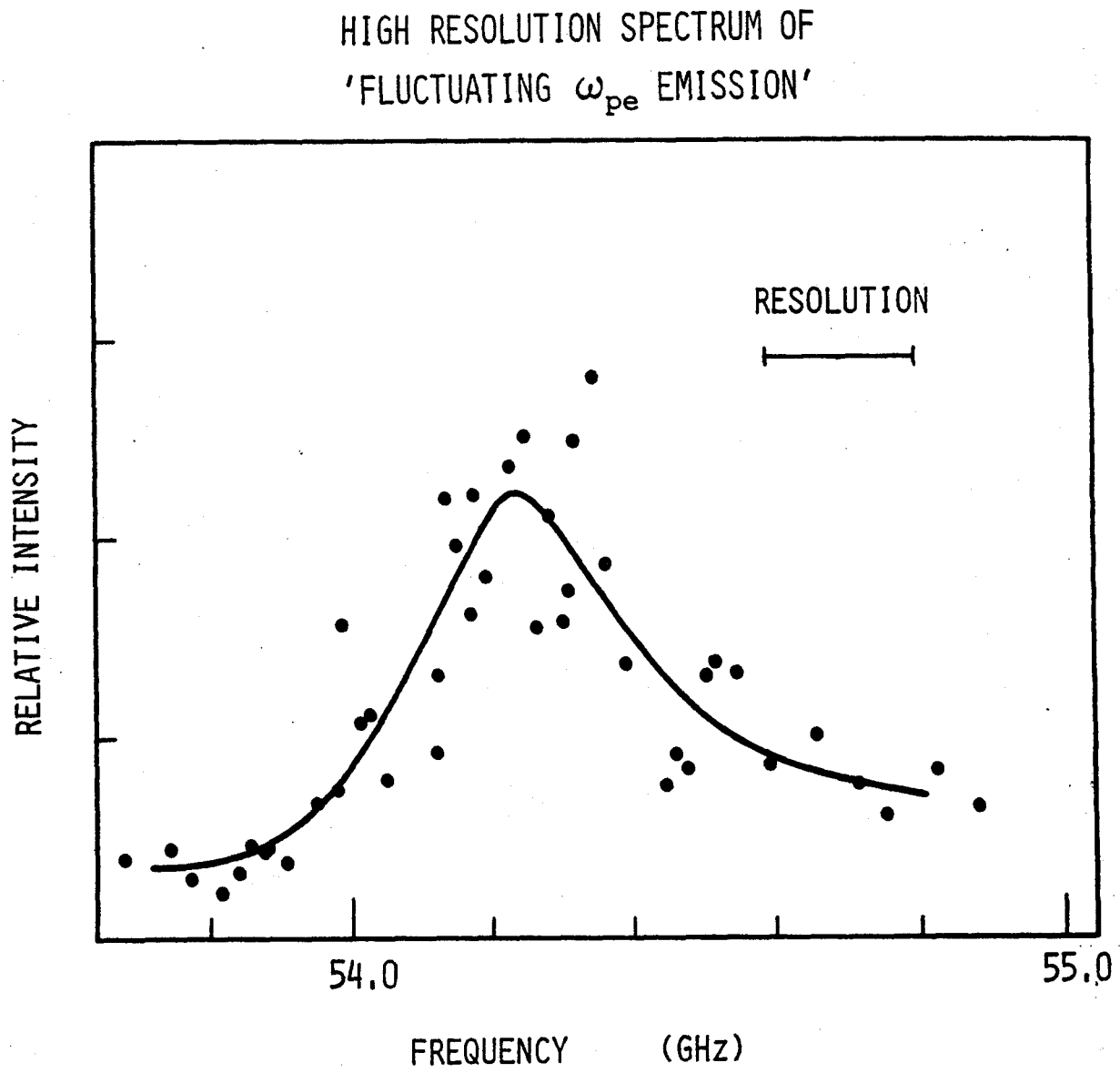

Fig.(5)
Spectrum obtained from previous figure. Instrumental resolution of .2 GHz is determined by the meshes used in the construction of the Fabry-Perot interferometer.

'FLUCTUATING ω_{pe} EMISSION'
SPECTRUM OF NON-FLUCTUATING COMPONENT

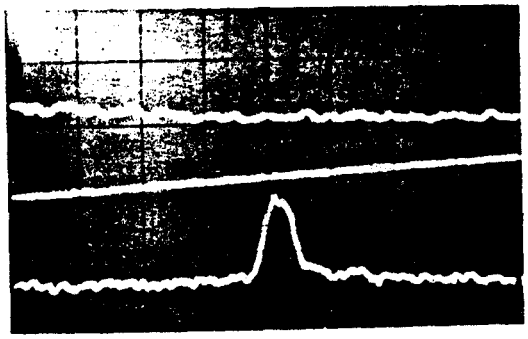

Fig.(6)
Horizontal scale corresponds to 1.3 GHz/division with the feature occurring at 71 GHz. The instrumental resolution at this frequency is 0.5 GHz, so that the feature is regarded as unresolved.

SUDDEN SHIFTS IN RADIATED FREQUENCY
OF 'FLUCTUATING ω_{pe} EMISSION'

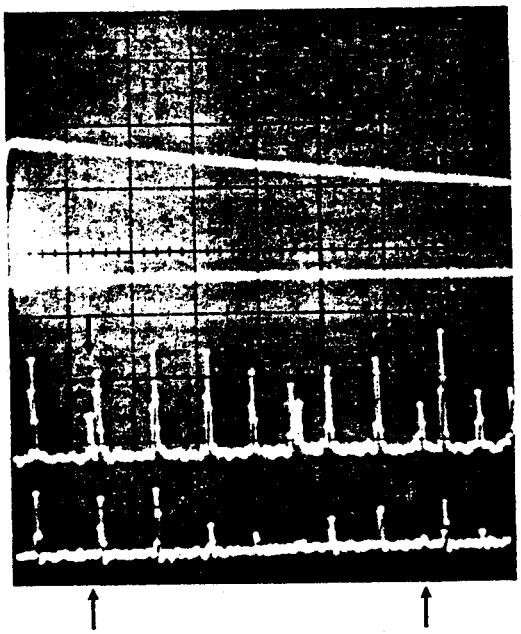

.1 msec/division

Fig.(7)
Horizontal scale corresponds to sweep in frequency from 55 to 52 GHz, left to right. At indicated times only one of two consecutive bursts is transmitted, indicating a frequency difference of .3 GHz or more.

SEC 9.0 FLUCTUATING EMISSION: PLASMA WAVES

The peculiar conduct of fluctuating ω_{pe} emission can generate numerous explanations, particularly when dealing with the complex Tokamak environment. Nonetheless, explanations can be dismissed as untenable when they predict behaviour contradicting the established experimental results, or when they impose unrealistic restrictions to plasma parameters. A candidate process must require the presence of runaway electrons, and must generate intense narrowband radiation near the plasma frequency. It must allow for the variety of temporal fluctuations and correlations observed, and must be capable of operating under a continuous variety of plasma conditions.

SEC 9.1 STIMULATED EMISSION

An example of a process eliminated from consideration is the spontaneous Cerenkov resonance discussed in sec (6). As demonstrated by experiment and theory, the spectral width of this radiation is very much broader than measurements of fluctuating emission, sec (8). The frequency domain of Cerenkov emission is determined through the dispersion relation by the density and magnetic field; quantities which are constant in neither time or space in the Tokamak plasma. For similar reasons spontaneous cyclotron radiation by runaways is discounted. This process, while capable of generating emission far in excess of thermal levels, is fundamentally very broadband in nature.

These spontaneous emission processes produce broadband emission because the dispersion relations governing electromagnetic waves are not particularly restrictive, allowing a single fast electron to be resonant with, and produce radiation at many frequencies. Stimulated

processes can produce narrow spectra by coupling the emission product back with the emitting plasma, allowing the most unstable frequency (the one with greatest growth rate) to dominate the spectra. One such possibility is the stimulated emission of extraordinary waves by Cerenkov resonance with runaway electrons. In analogy with an optical laser, this would require an unstable medium characterised by a population inversion or negative temperature, a coupling process, and some effective cavity to provide the feedback between wave and medium. Or, it is possible for the gain to be so large that in a single pass through the medium a dominant wave emerges, requiring no 'cavity'. As discussed in sec (6) trapping of extraordinary waves can result from the total internal reflection due to the radial decrease in refractive index. However, this trapping appears to be weak in the toroidal case, by the very fact that the spontaneous emission is observed.

It seems unlikely that stimulated emission of extraordinary radiation is responsible for the observed feature, since no accompanying spontaneous emission is ever seen in conjunction with fluctuating emission. Furthermore, the Cerenkov resonance requires a high electron energy, since the refractive index is close to unity, which contradicts the observation of fluctuating emission from plasmas which would appear to have marginal runaway energies.

The considered explanations of fluctuating ω_{pe} emission all involve some intermediary mechanism, electrostatic plasma waves in particular, which greatly restricts the range of frequencies to be eventually radiated. The utility of the plasma waves results from their narrow frequency spectrum and their possible resonance with marginally non-thermal electrons. In addition, the trapping condition

on electrostatic waves is much stronger, so that a 'cavity' exists, and electrostatic waves can be described as modes confined near the plasma centre. Given the existence of runaway driven plasma waves, it must be shown how these waves give rise to electromagnetic radiation.

SEC 9.2 RELATED EXPERIMENTAL OBSERVATIONS

Related experimental observations of an extraterrestrial origin concern a class of events known as type III solar bursts[1], characterised by radiation at the fundamental and second harmonic of the local plasma frequency. Energetic electrons (100 keV) are ejected from the sun during a solar flare and stream along field lines through the solar wind plasma, where they drive linearly unstable plasma waves. Saturation of these waves by a quasi-linear plateau formation would limit their propagation to only a few kilometers, conflicting with the observation of waves in the vicinity of earth. An alternate non-linear stabilisation mechanism has been proposed[2] which allows the plasma waves to propagate as localised wave packets, or solitons. This mechanism produces a spread in phase velocity of plasma waves through a parametric decay which generates an enhanced level of ion acoustic fluctuations. Radiation at the fundamental results from scattering of electrostatic waves from the density fluctuations of the ion waves, while radiation at the second harmonic occurs by coalescence of two plasma waves.

A somewhat contradictory model[3] of solar burst radiation involves the 'collapse' of the plasma wave packets on time scales much shorter than the growth time of the beam mode, rather than a stabilisation of the mode. The collapse of the wave packet is in the

spatial sense, and is produced by a spreading in wavenumber of the plasma waves. Radiation at ω_{pe} and $2\omega_{pe}$ occurs by the same scattering process described previously.

Regardless of what model is used, the fact remains that electromagnetic radiation associated with type III solar bursts occurs at twice the plasma frequency as well as the fundamental. The intensity at twice the plasma frequency is as or more intense than that at the plasma frequency, which is not the case for the Alcator results, where no radiation at $2\omega_{pe}$ is seen. Furthermore, the solar wind plasma is not strongly magnetised, ($\omega_{pe}/\omega_{ce} = 100$), so that the dispersion relation for plasma waves is not strongly dependent upon the wave vector direction with respect to the magnetic field. This is not the case for $\omega_{pe} < \omega_{ce}$, when the appropriate branch of the dispersion relation becomes[4]:

EQ (1) $$\omega^2 = \frac{\omega_h^2}{2} - \frac{1}{2}\left[\omega_h^4 - 4\omega_p^2\omega_c^2\cos^2\Theta\right]^{1/2} \cong \omega_p^2\cos^2\Theta$$

This means that the envisioned decay to a low frequency wave can only occur for resultant plasma waves propagating at small angles to the field, reducing the problem to one dimension, whereas the 'collapse' models are two dimensional. A final difference arises from the fact that the Alcator plasma has comparable electron and ion temperatures, so that acoustic waves will be strongly damped. Decay would then have to proceed into ion quasi-modes, and radiation would result by scattering from the thermal fluctuation level.

Back on earth, some of the earliest reports of spectral measurements of a fluctuating plasma frequency emission were made in conjunction with turbulence studies on the Uragan stellarator[5,6]. A bursting type of microwave emission above the thermal level lies in the vicinity of the electron plasma frequency, while the turbulent noise spectrum shows fluctuations at harmonics of the ion acoustic frequency. The radiation has an instantaneous spectral width of 10% while the spectrum of fluctuations shows two peaks at twice and four times the ion frequency. The radiation can be described by $\omega_{pe}+-\omega_{pi}$ and $\omega_{pe}+-2\omega_{pi}$, and is explained by the nonlinear scattering of plasma waves by density fluctuations at the ion acoustic frequency.

A fundamental difference concerning the Uragan and Alcator results is that the Alcator plasma is nearly isothermal, $T_e = T_i$, while for Uragan it is not, $T_e = 10\ T_i$. Significantly, when auxiliary ion heating produces equivalent temperatures in Uragan, $T_i > T_e$, the fluctuating emission vanishes. This can be explained by the strong ion Landau damping of ion waves which occurs when the ion thermal velocity approaches the ion sound speed. Also, the Alcator plasma is not in the same turbulent state, with the marked resistive anomaly, as the Uragan plasma. Finally, the spectral measurements from the two machines have a dissimilar character.

A more recent experiment on a linear device[7] has generated results which are similar to those reported from the Uragan stellarator. An electron beam is injected along the magnetic axis of a uniform plasma. High frequency electrostatic waves with frequency $\omega > \omega_{pe}$ are seen to grow and quickly saturate. Measurements of the dispersion of these waves identifies them as electron plasma waves.

Saturation of the plasma wave amplitudes corresponds to the onset and growth of low frequency density fluctuations, and the simultaneous emission of electromagnetic radiation near the plasma frequency. The density fluctuations are confined to a relatively narrow frequency band, and display the dispersion of ion acoustic waves propagating in the direction of the electron beam. The frequency spectrum of the electromagnetic radiation is a few percent wide, with centre slightly above the electron plasma frequency. The radiation is polarised in the direction of the incident beam (ordinary mode). The experimental results are shown to agree very well with a mechanism wherein radiation results from scattering of intense plasma waves from self consistently produced ion acoustic waves.

In this and other linear experiments, $T_e > T_i$ allows acoustic waves which are only moderately damped. In addition, there is often a high degree of turbulence, and even radiation at $2\omega_{pe}$[8]. Experimentally, beam injection at one end of a linear device allows downstream tracing of wave growth, so that distinctions between convective and absolute instabilities[9] can be made. In the case of a Tokamak, the 'beam' is injected continuously in space, so that the distinction between a instability that travels spatially with the beam and one that grows in time for all space can not be made.

Finally, some mention in passing should be made concerning a class of runaway instabilities noted in Tokamaks, which arise from an anomalous Cerenkov resonance effect[10]. While this mechanism does produce periodic bursts of plasma waves (the mechanism does not explain the radiation that is observed), it also generates simultaneous fluctuations in the loop voltage, temperature, current,

hard x-rays etc. The driving force of the instability is a severe temperature anisotropy, and the periodic fluctuates result from a sudden sudden attempt to equilibrate the parallel and perpendicular electron temperatures. This effect is not observed in Alcator, nor is it expected, since the total energy of the runaways is negligible compared to the background plasma, which is well behaved.

SEC 9.3 RUNAWAY ELECTRONS

An initial circumstance required in all the previous experimental results, including those from Alcator, is the generation of a detached component of suprathermal electrons. In the case of solar bursts and beam plasma studies, these electrons are created external to the plasma with which they interact, whereas in Stellarators and Tokamaks creation occurs within the very plasma. In these toroidal devices the source of suprathermal electrons is the runaway phenomenon associated with the current driving induced electric field. By equating the energy gain during free fall in the electric field with energy loss through coulomb collisions, a critical electron runaway field is found[11]:

EQ (2)
$$E_c = \frac{4\pi e^3 n_e \ln\Lambda_c}{m v_{th}^2} = \frac{4 \ln\Lambda_c}{15} \frac{n_e}{T_e}$$

{Volt cm^{-1}, 10^{14} cm^{-3}, KeV}

The highest electric fields, .12 V/cm, are encountered during plasma ionisation and shortly thereafter. These fields do not exceed the critical runaway field (E_c = 2 V/cm) during this time, so the plasma as a whole will not runaway, rather only electrons with motion in excess of a critical velocity will:

EQ (3) $$\frac{v_c}{v_{th}} = \left[\frac{E_c}{E}\right]^{1/2}$$

The rate of runaway production is determined by the ratio of the thermal electron velocity to this critical runaway velocity:

EQ (4) $$\lambda = K n_e \nu(v_{th}) \left[\frac{v_{th}}{v_c}\right]^{-3/4} \exp - \left[\left\{\frac{v_c}{2v_{th}}\right\}^2 + \frac{\sqrt{2}\, v_c}{v_{th}}\right]$$

An estimate of the number of runaways can be made by applying eq (4) to the period shortly after breakdown, while the voltage is high and before hard x-ray activity indicates the loss of runaways. In the case of fig.(2), sec (7) this approximation is between 10^6 cm^{-3} and 10^7 cm^{-3}.

The presence of runaway electrons alone does not a plasma wave make. The traditional linear formalism requires a positive slope to the runaway distribution, as in the case of the well known 'bump on tail' problem. This type of distribution can be expected when the critical runaway velocity decreases rapidly, so as to detach an isolated segment of velocity space from the bulk distribution. Such a situation can be realised during the early current rise portion of Tokamak discharges when the critical velocity changes from $U_c = 16V_{th}$ to $U_c = 60V_{th}$ in a period of 3-5 msec. Bumps in velocity space due to the presence of neutral atoms have also been noticed during the ionisation phase[12], which may account for the observation of fluctuating emission immediately following complete ionisation. It is not unreasonable to suppose that a beam type electron distribution accompanies fluctuating emission, but since no direct measurements of the distribution have been made this can only be an assumption. It is

noteworthy that grossly runaway discharges, produced by withholding neutral gas injection, do not generate fluctuating emission. This suggests the necessity of a subtle perturbation of the electron distribution, rather than a wallop of runaway current.

SEC 9.4 PLASMA WAVE MODES

A beam of runaway electrons will drive linearly unstable plasma waves which satisfy the resonance condition; $\omega - k\, v_b = 0$. If runaways are restricted to having only parallel velocity, the use of the cold plasma wave dispersion, eq (1), yields:

EQ (5) $$\omega_p \cos\Theta = |k|\, v_b \cos\Theta \quad ; \quad |k| = \frac{\omega_p}{v_b}$$

This means that a particular beam velocity will be resonant with waves having the same magnitude wavenumber. Since the duration of a single burst of radiation is much greater than the circumferential transit time of the driving electrons, it is reasonable to assume that the plasma waves can be represented by a toroidally uniform waveform or mode.

Inspection of the dispersion relation, $\omega = \omega_b \cos\Theta$ shows that as the wave propagates radially outward into regions of reduced density, $\cos\Theta$ must increase to maintain constant frequency. The condition $\cos\Theta = 1$ limits the radial extent of the wave, so that peaked density profiles will result in the trapping of plasma waves near the plasma centre. If the torus is treated as a cylinder with periodic boundary conditions over a length $2\pi R$, undamped plasma waves can be described by mode numbers representing the allowed perpendicular and parallel

components of the wave vector.

$$\Psi(r,z,t) = \Phi_{m,n}(r) \exp i\{k_n z - \omega_{m,n} t\} \quad ; \quad k_n = n/R$$

EQ (6)

$$\Phi_{m,n}(r) \to 0 \quad \text{for } r > 0$$

The parallel wavenumber must be an integer multiple of the reciprocal major radius. Because of the relative large size of the major radius with respect to typical plasma wavelengths, the axial mode number will be quite large, $n > 800$. Changes in the axial mode number will produce small changes in the wave frequency, typically $\Delta\omega = 70$ MHz, which is smaller than the resolution of the measurement system. The perpendicular extent of the wave is determined by the density profile, and by the frequency of the wave with respect to the central plasma frequency.

$$\frac{1}{r}\frac{d}{dr} r \frac{d}{dr} \Phi_{m,n}(r) + k_\perp^2(r)\Phi_{m,n}(r) = 0$$

$$k_\perp^2 = k^2 \left[\frac{\omega_p(r)^2}{\omega^2} - 1 \right]$$

EQ (7)

$$k_\perp^2(r) = k^2\{ [1 - r^2/r_{lim}^2]^{1/2} - \omega^2/\omega_p^2 \}$$

where a square root parabola density profile is assumed. For a particular k, as determined by the beam velocity, bounded radial solutions will exist for discrete values of ω only. The two lowest mode number radial solutions are shown in fig.(1), where it is seen that the radial extent of the plasma wave is confined to the plasma centre. This restriction offers a possible explanation for the correspondence of the emitted frequency to the central plasma frequency, and the correlation of emission with centrally located MHD activity. A shift in radial mode number, for example from $m = 1$ to $m = 2$, will produce a frequency change of 430 GHz under typical

conditions. This difference is larger than the instrumental resolution, so that the observed discontinuities in the emission frequency may be related to radial mode transitions of the plasma wave.

SEC 9.5 OTHER WAVES

Fig.(2) shows the Appleton-Hartree dispersion relation for nearly parallel propagation. The waves that have been discussed belong to the electrostatic limit of the low frequency ordinary mode branch. As shown, these waves occur at or just slightly below the plasma frequency, and can be resonant with many electron velocities. Additional branches also pass through the $\omega = \omega_{pe}$ region. One such branch corresponds to the extraordinary mode involved with the spontaneous Cerenkov emission. It is seen that waves in this region are resonant with relativistic electrons only, $1.0 > n > 1.1$. and because of their large phase velocity cannot be treated as purely electrostatic waves. Notice that the extraordinary mode resonance with relativistic electrons extends nearly to the cyclotron frequency. This is why the spontaneous Cerenkov emission is fundamentally broadband. Ignoring stimulated Cerenkov emission means that waves on this branch are not considered.

Electrons resonant with the magnetised plasma waves can also resonate with electron cyclotron waves near ω_{ce}. If the fluctuating emission involves driven waves belonging to the ω_p branch, then some consideration of the higher frequency electrostatic waves should be made. These waves have the following angular dependence:

EQ (8) $$\omega^2 = \frac{\omega_h^2}{2} \frac{1}{2}\left[\omega^4 - 4\omega_p^2 \omega_c^2 \cos^2\Theta\right]^{1/2} \approx \omega_c^2 + \omega_p^2 \sin^2\Theta$$

As the wave propagates outward to regions of decreasing magnetic field and density, the angular term must increase to maintain constant frequency. Eventually the wave travels perpendicular to the field where it is absorbed at the upper-hybrid layer, which will always lie between the cyclotron resonance and the observer. If the wave propagates inward, the increase in field and density will decrease Θ and reflect the wave. In contrast to the magnetised plasma waves, the electron cyclotron waves are excluded from the centre. Thus no stimulated process is expected to occur with these waves. If some non-thermal radiation process were to occur at the cyclotron frequency, it would not be observed from the outside in any case, since the fundamental is optically thick in the ordinary mode, and is cutoff by the hybrid layer in the extraordinary mode.

SEC 9.6 SATURATION OF PLASMA WAVES

Given the instability of plasma waves to linear growth, a fair question concerns the saturation mechanism of these waves. Two known mechanisms are beam trapping[13], and decay instabilities[14]. For a small cold beam, the initial limitation of the instability is determined by trapping of beam electrons in the potential of the driven wave, while decay processes require larger levels of beam energies.

According to the trapping model, a single wave emerges from the initial unstable band of wavenumbers. If a beam has density n_b and velocity v_b, this single wave will have the maximum growth rate:

EQ (9) $$\frac{\gamma_{max}}{\omega_p} = \{ 3^{1/2}\, 2^{-4/3} \}\{ \frac{n_b}{n_e}^{1/3} \} \qquad k = \frac{\omega_p}{v_b}$$

When the beam density is small, the wavenumber spread of the growing waves will be negligible, and trapping of beam electrons will occur in the potential wells of the nearly sinusoidal wave electric field. After several trapping times, the wave energy tends toward a meta-equilibrium:

EQ (10) $$W = \frac{n_b\, m\, v_b^2}{2}\; 2^{-4/3} \left[\frac{n_b}{n_e}\right]^{1/3}$$

In the most extreme case this energy is expected to be less than 1% of the thermal electron energy, so in no way is this a strong beam plasma case. The meta-equilibrium will persist until other waves have grown to a similar amplitude as the original unstable mode, when a quasi-linear description becomes appropriate. This will produce a broadening of the wave spectrum and the formation of a plateau in the beam distribution.

The decay instability limits growth due to the non-linear transfer of energy from beam resonant waves to non-resonant modes. This is the process applied to the case of solar bursts, where the original plasma wave decays into another plasma wave of larger wavenumber, and an ion acoustic wave. The product plasma wave will have lower phase velocity, so it will be non-resonant with the beam, but may be damped by the ambient plasma. Without measuring the spectrum of high frequency fluctuations, it cannot be definitely stated which saturation process is occurring. However, the trapping

model requires only a coherent linearly unstable wave, and will operate for small values of beam energy. Eq (10) may be regarded as an upper limit to the expected wave energy, since any decay process will only reduce this value by transferring energy to other modes.

SEC 9.7 LINEAR RADIATION PROCESSES

A plasma wave by itself will not radiate. Although a thermal test electron will undergo an oscillation which in vacuum would produce radiation, the particle under consideration is moving in a medium of changing dielectric. Because of this, a dipole moment is generated which cancels the effect of the electron motion, so that no radiation results. Alternately it can be said that since the density and velocity perturbations of the plasma wave are out of phase, no net oscillatory current results. If the test particle has a relativistic mass, radiation can result from its motion through the plasma wave[15]. However, the plasma waves are being driven by non-thermal electrons and have phase velocities close to the speed of light, so that most relativistic particles will be moving in phase with, rather than through the wave. Furthermore, this relativistic effect produces a broadband radiation spectrum, which is contrary to the experimental measurement.

Another mechanism providing a direct conversion of plasma waves to electromagnetic radiation is linear mode conversion in the presence of an inhomogeneity, such as the steady state density gradient. It has been shown by theory and experiment[16] that such a process occurs in an unmagnetised plasma, however, the treatment cannot be extended to the strongly magnetised case. The reason for this is the inability

to match both frequency and wavenumber of the two modes, as required by the linear theory. The plasma wave can be described by the cold plasma dispersion, eq (1), and the resonance condition:

$$\text{EQ (11)} \qquad k_{\parallel}^2 = \frac{\omega_p^2}{v_b^2} = \frac{\omega_p^2}{c^2}\frac{c^2}{v_b^2} > \frac{\omega^2}{c^2}$$

The conversion must occur near $\omega = \omega_{pe}$ into electromagnetic waves propagating parallel to the field, that is, into left circularly polarised waves. The appropriate cold plasma dispersion is:

$$\text{EQ (12)} \qquad k_{\parallel}^2 = \frac{\omega^2}{c^2}\left[1 - \frac{\omega_p^2}{\omega(\omega + \omega_c)}\right] < \frac{\omega^2}{c^2}$$

It is seen that for a typical situation, $\omega_{ce}/\omega_{pe} = 4$, it is not possible to satisfy both conditions on the wavenumber. The two mode branches remain separate, and no linear conversion may occur.

It has been assumed that the density gradient is totally in the perpendicular direction, that is , $\nabla n \cdot B = 0$. This is expected to hold in steady state since the rapid parallel diffusion will produce a toroidally symmetric density distribution. The mode conversion treatment also assumes that the scale length of the inhomogeneity is much greater than the wavelengths of the modes involved. If this is not true, it is no longer possible to treat the wave modes continuously across the inhomogeneity, and a scattering description becomes appropriate.

REFERENCES & FIGURES

1.) E.N. Kruchina, R.Z. Sagdeev, V.D. Shapiro
Pis'ma Zh. Eksp. Teor. Fiz. 32 443 (1980)

2.) H.P. Freund, K. Papadopoulos
Phys. Fluids 23 732 (1980)

3.) M.V. Goldman, G.F. Reiter, D.R. Nicholson
Phys. Fluids 23 388 (1980)

4. This approximation to the actual cold plasma dispersion is accurate to better than 5% for all angles Θ under the Alcator plasma conditions. It is better than 1% accurate for angle $\Theta < 30^{o}$.

5.) N.Perepelkin, V.Suprunenko, M.Vasiliev, A.Dikii
Paper 19 III Int. Sym. Toroidal Plasma Confinement
Garching, FDR (1973)

6.) A.Longinov, N. Perepelkin, V.Suprunenko
Fiz. Plazmy 2 626 (1976)

7.) D.A. Whelan, R.L. Stenzel
Phys. Rev. Lett. 47 95 (1981)

8.) Y.Kalinin, D.Lin, V.Ryutov, V.Skoryupin
Zh. Eksp. Teor. Fiz. 55 115 (1968)

9.) M. Seidl, W. Carr, D. Boyd, R. Jones
Phys. Fluids 19 78 (1976)

10.) L. Muschietti, K. Appert, J. Vaclavik
Phys. Fluids 24 151 (1981)

11.) H. Knoepfel, D.A. Spong
Nuclear Fusion 19 785 (1979)
Review paper on runaway electrons in Tokamaks

12.) G.A.W.Lins, H.-J.Kunze
Phys. Fluids 24 839 (1981)

13.) T.M. O'Neil, J.H. Winfrey, J.H. Malmberg
Phys. Fluids 14 1204 (1971)

14.) A.L. Throop, R.R. Parker
Phys. Fluids 22 491 (1979)

15.) A. Gailitis, V.N. Tsytovich
Zh. Eksp. Teor. Fiz. 46 1726 (1981)

16.) R.W.Means, L.Muschietti, M.Q.Tran, J.Vaclavik
Phys. Fluids 24 2197 (1981)

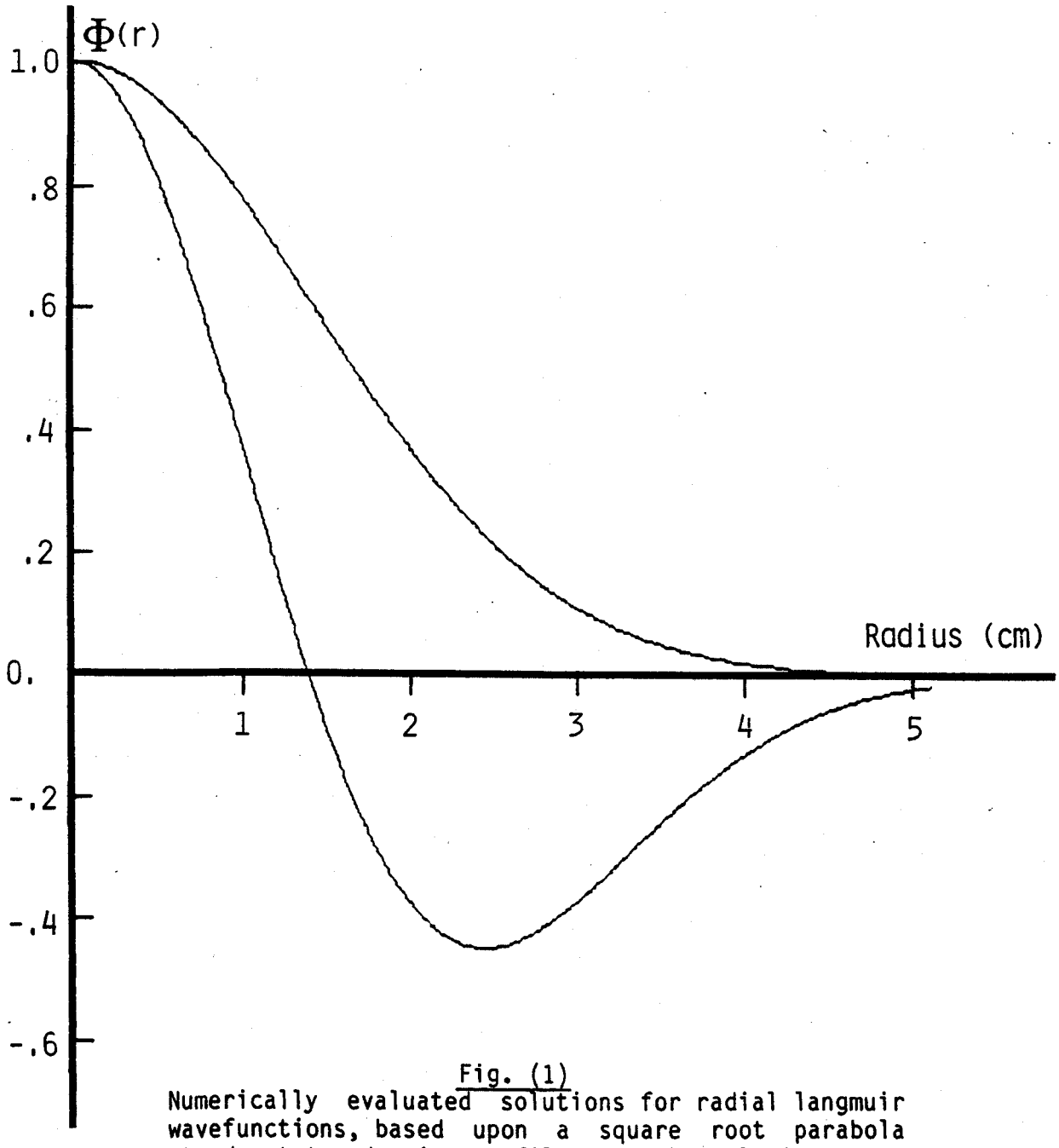

Fig. (1)

Numerically evaluated solutions for radial langmuir wavefunctions, based upon a square root parabola steady state density profile. Both solutions are for the case $k_{\parallel} = 13 cm^{-1}$. The two modes are separated by 430 MHz for a central plasma frequency of 60 GHz.

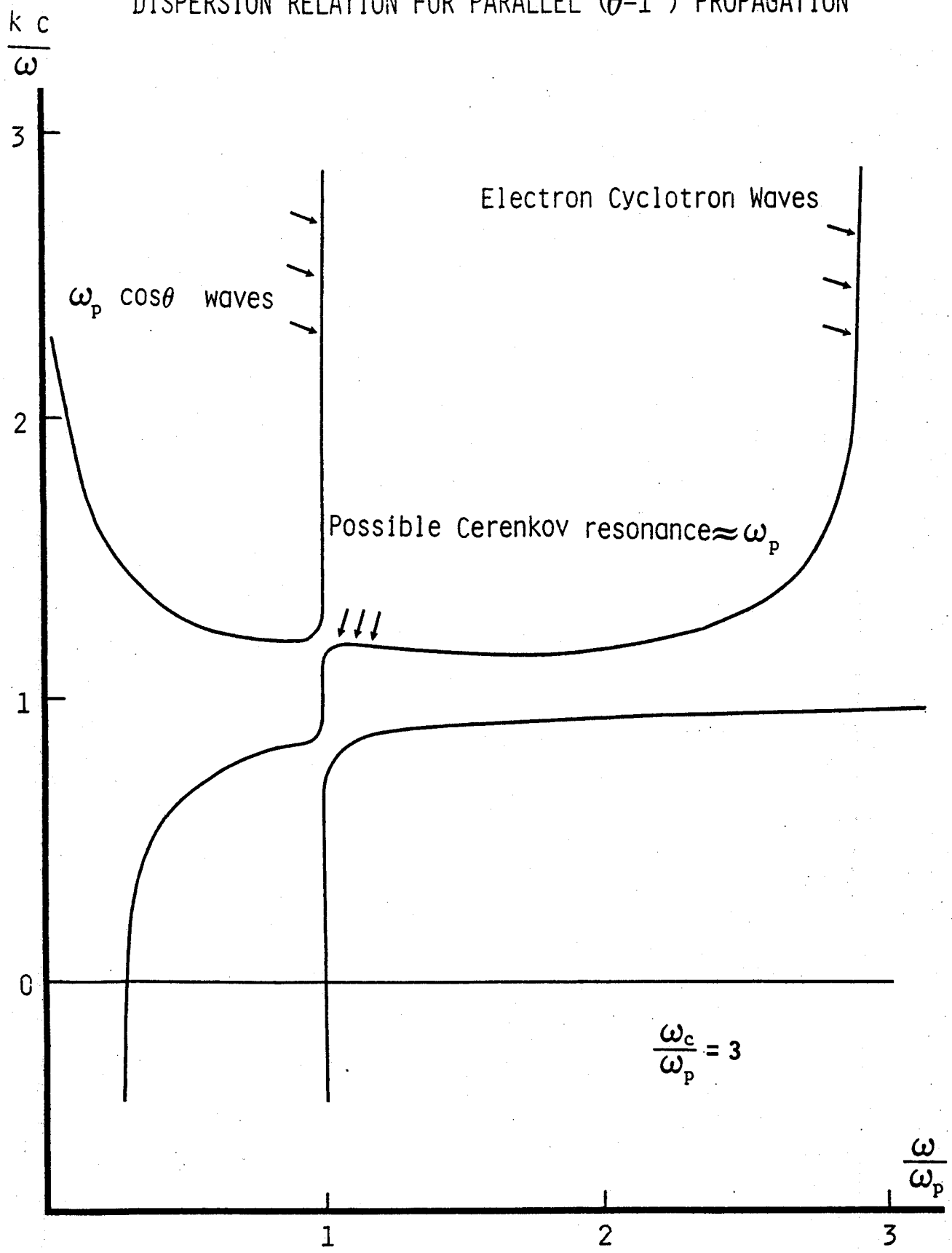

Fig.(2)
Appleton-Hartree dispersion for cold plasma. The two nearly electrostatic waves which may be resonant with non-thermal electrons occur

SEC 10.0 FLUCTUATING EMISSION: NON-LINEAR EFFECTS

The resonant three wave interaction is a non-linear coupling of modes which allows the transfer of energy between the three oscillating waves. Pertinent to a discussion of fluctuating ω_p emission is the interaction involving magnetised plasma waves and electromagnetic radiation near the plasma frequency as two of the constituents. The former wave is expected to exist by the linear coupling to runaway electrons, and is described in terms of axial and radial mode numbers per the previous section. The electromagnetic wave is known to exist, since it is directly measured, albeit after having exited the plasma. The identity of the third wave is unknown, however, its frequency and wavenumber are restricted by resonance conditions, and by the measured spectral width of the radiation feature. Because of the numerous experimental and theoretical studies of three wave interactions involving acoustic fluctuations, this mode is of particular interest as a possible third wave.

SEC 10.1 RESONANCE CONDITIONS

The process under consideration can be schematically represented by the following expression:

$$[\ \omega_l, k_l\ ] + [\ \omega_s, k_s\ ] \rightarrow [\ \omega_t, k_t\ ]$$

EQ (1)

$$[\ \omega_l, k_l\ ] \rightarrow [\ \omega_s, k_s\ ] + [\ \omega_t, k_t\ ]$$

where the subscripts l,t refer to the plasma (langmuir) and electromagnetic (transverse) waves, and s to the scattering wave. No restriction has yet been placed on the scattering wave, which in fact can be a particular fourier component of a steady state perturbation;

i.e $\omega_s = 0$. The resonance condition is the fairly obvious requirement that the sum of the constituent waves and the product wave must maintain a nearly constant phase in both time and space:

EQ (2)
$$\omega_1 + \omega_s \cong \omega_t \qquad k_1 + k_s \cong k_t$$
$$\omega_1 \cong \omega_s + \omega_t \qquad k_1 \cong k_s + k_t$$

Because the measured frequency of the emitted radiation is nearly equal to that assumed for the plasma wave, the third wave must have a relatively small frequency in comparison. This eliminates, for example, the scattering process involving two plasma waves. The resonance condition thus restricts the scattering wave:

EQ (3)
$$\omega_t \approx \omega_1 + \omega_s << \omega_1$$

While the close proximity of the transverse and langmuir wave frequencies limits the magnitude of ω_s, this consideration alone is far less restrictive when applied to the allowed wavenumbers. The reason is that the resonance condition applies to the waves at the location of scattering, i.e. within the plasma, where the strong dispersion allows for a variety of transverse wavenumbers for any particular frequency. The refractive index near the plasma frequency depends strongly upon the wave polarisation, and upon the angle of emission with respect to the magnetic field [see fig.(6) of sec(6)]. As these quantities cannot be measured, the appropriate wavenumber of the emitted transverse wave is uncertain. The central plasma density is not known well enough to determine if the measured transverse wave frequency lies above or below the associated plasma

frequency. However, the separation of the lowest order langmuir mode and the central plasma frequency is 430 MHz for a typical situation. Thus, if the scattering wave has a frequency above this difference, the condition $\omega_t > \omega_p$ can be satisfied everywhere in the plasma. Such a situation could result from scattering by acoustic waves where ω_s = 1 GHz. The case $\omega_t/\omega_p > 1$ allows the transverse wave access to both polarisations for all emission angles. Since ω_s is small, the alternate situation, $\omega_t < \omega_p$, can only be satisfied near the plasma centre. This can be seen in fig.(1) of sec(9) where the inflection point (change in sign of curvature) of the radial langmuir mode occurs at the point where $\omega_l = \omega_p$. Thus the condition $\omega_t < \omega_p$ can only be satisfied for a region within a few cm. of the centre. It is not appropriate to localise the emission process to a volume of characteristic dimension less than a few wavelengths and still maintain a description of the wave as being everywhere a mode of a continuously varying medium. Even if the transverse wave frequency is slightly less than the central plasma frequency, in the plasma volume outside of the region of emission the dielectric is still described by the condition $\omega_t > \omega_p$.

The inability to experimentally discern a preferred polarisation for the transverse wave does not indicate a lack of polarisation of the emitted wave. As was the case for the second gyroharmonic, the effects of wall reflections and diffraction will scramble the polarisation. This effect is expected to be more severe at lower frequencies when the wavelengths are comparable to the physical dimensions of the flange and internal bellow assemblies. Although consideration of the polarisation of the non-linear oscillating

current favours radiation into the ordinary mode, there is no justification for disallowing the extraordinary mode, particularly if the waves are emitted with small angle to the magnetic field.

SEC 10.2 DISPERSION RELATION

Fig.(1) shows the wavenumbers as a function of angle for the two polarisations of transverse waves emitted at a frequency slightly above the plasma frequency. The Appleton-Hartree cold plasma dispersion relation is the source of these curves. In addition, a region of k-space is indicated where the langmuir waves are expected, as determined by their required resonance with non-thermal electrons. These electrostatic modes are also solutions to the Appleton-Hartree equation for the special case of a large refractive index. To satisfy the resonance condition, the scattering wave must connect the wavevectors of the langmuir and transverse waves. Several such possible scattering waves are indicated. Fig.(1) shows that k_s is fairly restricted in direction, so that the scattering wave must propagate mostly along the magnetic field, and in a direction opposite to the plasma waves. This means that a purely perpendicular wave cannot satisfy the resonance condition. The magnitude of k_s is quite unrestricted. For values of k_s ranging from near 0 to greater than 2.5 ω_p/c a possible scattering solution exists. The extrema of allowed scattering wavenumber apply only to emission into the extraordinary mode, k_s must satisfy $.68\ \omega_p/c < k_s < 2.2\ \omega_p/c$ in order to produce radiation in the ordinary mode.

The escape condition discussed in conjunction with Cerenkov emission can also be applied to the possible transverse waves. Transverse waves emitted close to the field direction in the extraordinary polarisation will be internally reflected and trapped in the plasma centre. For the conditions shown in fig.(1), trapping occurs for angles less than .14 rad. Thus, if the scattering wave propagates along the magnetic field, it is possible for both the langmuir and transverse waves to be trapped in the same volume. While this trapping may provide for strong interaction between the waves, it forbids detection of emitted transverse waves unless some disturbing perturbation (MHD activity?) allows the escape of radiation. Of course, if the radiation is emitted in the ordinary polarisation no such trapping may occur, regardless of the emission angle. Because of the small perpendicular scale of the langmuir modes, it can be argued that coupling is more efficient for transverse waves which propagate nearly parallel to the magnetic field direction, this because in such a case the interaction volume of the waves is maximised.

Fluctuations which propagate across magnetic fields include electrostatic ion cyclotron waves and magnetosonic waves, with frequencies near the ion plasma frequency, and drift waves at considerably lower frequency. Measurements of low frequency density fluctuations[1] by laser scattering indicate a broad spectrum of frequencies and perpendicular wavenumbers; typically $k_\perp = 0 - 25\ cm^{-1}$, $\omega = 300 - 400$ kHz. These fluctuations are continuous during most discharges, showing no correlation with plasma frequency emission. While the fluctuation level is highest at the plasma edge, a tentatively identifies secondary maximum occurs at the

centre, with typical magnitude of $\tilde{n}/n = 3\%$. It is suspected that these fluctuations result from drift waves, though this identification is very uncertain[2]. Regardless of their identity these fluctuations can only satisfy the resonance condition if the parallel component of the wavevector is sufficiently large. An upper bound of 6 cm^{-1} has been placed on this parallel component, that is, the typical wavevectors are preferentially perpendicular, and cannot satisfy the resonance condition. However, the range of measured values of $k_\perp$ and $k_\parallel$ allow for possible solutions. These possible drift waves are mentioned since they constitute the only measured fluctuations in the Alcator Tokamak. It seems that they are unlikely candidates for the non-linear emission process.

SEC 10.3 NON-LINEAR CURRENT

When all three waves are plasmons the resonance condition is equivalent to a statement of conservation of energy and momentum[3]. In the case considered here, the necessity of the resonance condition follows directly from the mechanics of the radiation process. The source term for electromagnetic waves is an oscillating current distribution, which cannot be produced by the plasma wave alone. The three wave interaction allows the generation of a non-linear oscillating current, which results from the mixing of the density and velocity perturbations from the coupled waves:

EQ (4) $$J_{nl}(r,t) = -e\,\tilde{n}_l(r,t)\,\tilde{v}_s(r,t) - e\,\tilde{v}_l(r,t)\,\tilde{n}_s(r,t)$$

where only the electron fluctuations need be considered. If the scattering wave has a small phase velocity in comparison to the plasma

wave (such as an acoustic wave), or if it is a steady state density perturbation, the first term in eq (4) is negligible compared to the second, so that the current density becomes:

EQ (5) $$J_{n1}(r,t) = \frac{-e\,\omega}{k}\,\frac{\tilde{n}_1\,\tilde{n}_s}{n_e}\,\exp\{i[k_1 + k_s]\cdot r - i[\omega_1 + \omega_s]\,t\}$$

$$J_{n1}(r,t) = J_o \exp i[k_j \cdot r - \omega_j\, t]$$

The radiation field resulting from the non-linear current distribution is found by solving for the vector potential:

EQ (6) $$A(r,t) = \frac{J_o}{cr}\,\exp i[\frac{\omega_j}{c} r - \omega_j\, t]\quad \exp i[k_j - \frac{\omega_j}{c}\hat{n}]\cdot r'\, d^3dr'$$

The oscillating coefficient determines the frequency and wavenumber of the radiated wave, i.e.; $\omega_t = \omega_j = \omega_1 + \omega_s$ and $k_t = \omega_j/c$, and the integral insures that $k_t = k_j = k_1 + k_s$. These are precisely the resonance conditions of eq (2).

The degree to which the resonance condition must be satisfied is determined by the extent of the integral eq (6), which in turn is controlled by the degree of coherence of the plasma and scattering waves. For example, if the current density is treated as a spatial wave packet of parallel extent L, a spread in wavenumber, $\Delta kj = 2\pi/L$, and thus radiated frequency, $\Delta\omega_t = \omega_t \cdot \Delta k_j/k_t$, results. The measured upper limit of the radiated frequency bandwidth, $\Delta\omega_t/\omega_t < 1\%$, indicates a minimum wave packet extent, L = 50 cm, which is comparable to the toroidal circumference, so that a wave packet representation becomes unacceptable. For this reason the plasma wave mode description of sec (9) is favoured. The narrowness of the bandwidth of radiated waves also restricts the frequency extent of the

scattering wave by a similar argument. However, since the scattering wave is known to have a low frequency anyway, applying a 400 MHz bandwidth for example, does not require an especially coherent wave.

SEC 10.4 ABSORPTION

When the size of the interaction region becomes large enough so that the radiated wave amplitude is comparable to that of either the plasma or scattering wave, it is necessary to consider the inverse processes, whereby energy is removed from the transverse wave and returned to the plasma modes. This situation is analogous to the treatment of emission and absorption of cyclotron radiation, in that a transport equation results.

When wave-particle interactions can be ignored, the transverse mode can be described by[4]:

$$\text{EQ (7)} \quad \left[\frac{d}{dt} + V_t\ (\text{group})\ \frac{d}{dr}\right] N_t = A_{t,l,s} \left\{N_l N_s - N_t N_l - N_t N_s\right\}$$

where N_a is the number density of mode a, related to the spectral energy density by $W_a = \omega_a N_a$. It is assumed in eq (7) that the resonance condition is satisfied by the three waves, so that frequency and wavenumber indices are ignored. Two similar equations describe the evolution of the other waves. The interaction kernel A_{tls} depends upon the identity of the scattering wave, and expresses the relationship between the non-linear current and the energy densities of the plasma and scattering waves.

By eq (7) it is evident that a quasi-equilibrium solution can exist. If the density of scattering waves is small, so that $N_l \gg N_s$, the last term in eq (7) is ignorable, so that for steady state:

EQ (8) $$N_t = N_s \rightarrow W_t = \left[\frac{\omega_p}{\omega_s}\right] W_s$$

This has been considered in the context of explaining dominant wp emission by the scattering of plasma waves from a thermal level of ion acoustic fluctuations[5], the intensity of the acoustic fluctuations being determined by the equipartition theorem. The result is an intensity of emitted radiation which is independent of the level of plasma wave energy, and is described by the effective temperature of the acoustic fluctuations:

EQ (9) $$I_t = I_{bb}(T_{eff}) \; ; \; T_{eff} = \frac{\omega_p}{\omega_s} [T_e \, T_i]^{1/2}$$

For the specific case of ion acoustic waves, an intensity of greater than 40 times the thermal level results, which is fairly representative of typical fluctuating wp intensities. Provided that the damping (second) term in eq (7) is large enough, the results of eq (9) will be true regardless of the type of scattering wave used. Accordingly, other branches of the ion spectrum will produce a similar result. If the damping term is small, then the emission term will also be small, so that a negligible amount of radiation results. The radiated intensity will be determined by the effective temperature, which presumably will be equal to or greater than the plasma temperature, and the frequency of the scattering wave. From eq (3) the scattering wave is known to have a low frequency compared to ω_p,

so the predicted emission intensity will be much greater than the thermal level. Drift waves, because of their lower frequency, will generate an even greater effective temperature. The case of drift waves in fact cannot be treated by eq (8) because the drift waves are saturated modes. The saturation mechanism, whatever it may be, must be included in eq (7), so that the process will no longer involve only three waves.

SEC 10.5 RELATION TO EXPERIMENT

A consequence of eq (9) is a constant expected emission intensity. Quite often the observed fluctuating emission can be described as having a nearly constant level. This is particularly true with regard to radiation which accompanies MHD activity, or which occurs in periodic bursts; figs. (3), (5), (7) of sec (7) are examples of this. (The discerning experimentalist refrains from citing those cases where constant intensity results from saturation of detector and/or electronics.) According to the scattering model, the emission fluctuations result from like oscillations in the non-linear current. This requires either the density of plasma or scattering waves to change rapidly. If the scattering waves are populated to an effective thermal level, then only fluctuations of the plasma waves can produce the observed emission behaviour. Because there is no correlated hard x-ray emission, the oscillation in plasma wave amplitude probably does not result from the wholesale loss of resonant runaway particles, but rather some subtle alteration of their velocity distribution which destroys the positive growth of the wave.

The correlated behaviour of fluctuating emission with m = 1 activity can result either from a direct involvement of the MHD mode in the radiation process, i.e. the m = 1 is the scattering wave, or indirectly, for example by trapping of the transverse and langmuir waves in the local density maxima.

If the m = 1 mode is regarded as a nearly stationary density perturbation of a few percent, with infinite parallel extent and perpendicular scale length of order .5 cm, reference to fig.(1) shows that a $k_s\perp = 3\ cm^{-1}$ could satisfy the wave matching condition only if a similar or larger $k_s\parallel$ were present. However, an infinite parallel extent implies a 0 parallel wavevector component. The MHD mode cannot satisfy the resonance condition because it is a purely perpendicular perturbation.

If the scattering wave is independent of m = 1 activity, the radiation can be imagined as occurring continuously. The observed correlation with m = 1 rotation may result from trapping and untrapping of the emitted transverse wave in the region of increased refractive index associated with the density perturbation. If the steady state density profile is peaked enough on axis, the radiation may escape only when a large rotating mode flattens the profile. This then could explain the result that during steady state emission is only observed in phase with large m = 1 oscillations which precede or follow sawtooth disruptions. Unfortunately, the absolute phase of the rotating mode relative to the emission is unknown.

SEC 10.6 REFERENCES & FIGURES

1.) R.L. Watterson et.al.
Bull. Am. Phys. Soc. 26 885 (1981)

2.) C.M. Surko, R.E. Slusher
Phys. Fluids 23 2425 (1980)

3.) R.C. Davidson
Methods in Non-Linear Plasma Theory
Academic Press, New York (1972) p.117

4.) V.N. Tsytovich
Nonlinear Effects in Plasmas
Plenum, New York (1970) p.90

5.) I.H. Hutchinson, Kim Molvig, S.Y. Yuen
Phys. Rev. Lett. 40 1091 (1978)

SCATTERING GEOMETRY
OF WAVEVECTORS

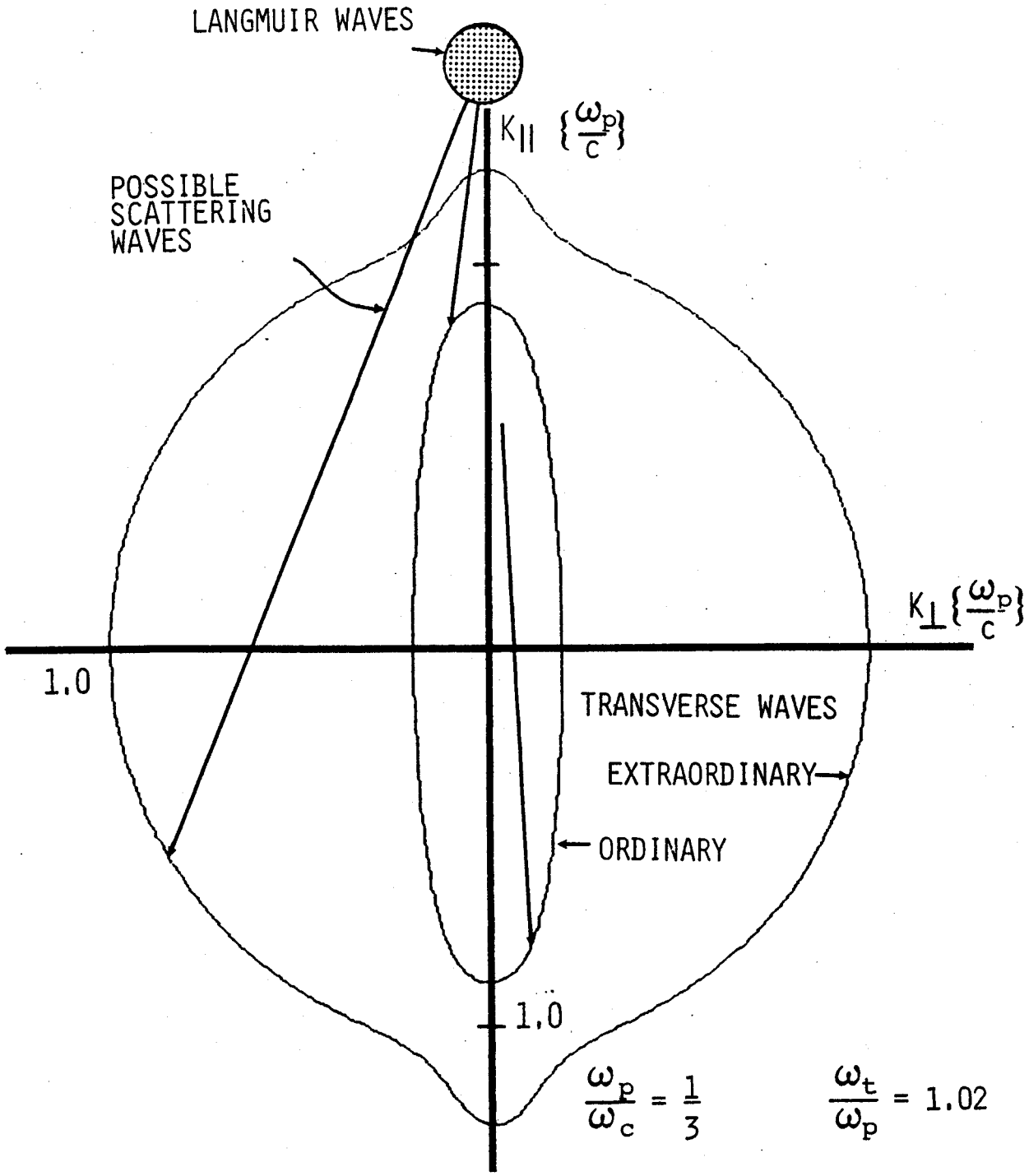

Fig.(1)
Because of only approximate knowledge of the plasma frequency (central density) the choice of ω_t/ω_p is somewhat arbitrary. Dashed line indicates trapped transverse waves. Langmuir waves are assumed to be resonant with runaway electrons; $v_{||} \cong c$, $v_{||} >> v_{\perp}$

SEC 11 CONCLUSION

The utility of submillimetre emission measurements as a diagnostic of plasma condition should be manifest from the previous sections. As a technique for determination of temporal and spatial evolution of electron temperature the measurement of emission at the optically thick second gyroharmonic is demonstrated to be particularly well suited. The ability to describe the temperature profile by the simple Gaussian expression should assist those persons interested in modelling transport properties in Tokamak plasmas, or to anyone in need of any analytic expression for the spatial temperature variation. That the temperature and profile width are consistent with a classical resistivity model indicates a relative small influence by anomalous and possible neo-classical effects. In addition, the repeatability of the scaling of profile width with limiter q allows the prediction of results in new parameter ranges, such as high current and field.

Radiation at the third gyroharmonic has been shown to be useful as a method for self consistent calibration of the entire system. This is not a trivial matter, as calibration remains a serious and difficult problem. As a possible topic for future work, it is suggested that a meticulous attempt to calibrate the diagnostic be undertaken. This would probably require the development of an intense broadband reference source, and possibly the resolution of the wall reflection, polarisation scrambling problem.

Sawtooth measurements have been made which do not involve the ambiguities inherent in chord-average techniques, such as soft x-ray emission. These results together with profile scaling suggest a range

of central current density such that q_o fluctuates between .8 and 1.0 during the sawtooth, with time average value of q_o = .85. The peculiar behaviour of sawteeth in helium plasma should be of interest to persons attempting an explanation of the sawtooth phenomena.

The observation of non-thermal submillimetre emission can be used as an indicator of a non-equilibrium electron distribution. However, the degree of the deviation from equilibrium is uncertain since the emission process, at least in the case of fluctuation ω_{pe} radiation, is uncertain. In fact it would appear that only a subtle perturbation of the electron distribution is required. Since the fluctuation emission occurs in such a narrow bandwidth, a technique for extremely accurate density measurement suggests itself. Furthermore, the interesting correlation behaviour of fluctuating emission with m = 1 modes may provide new information regarding these events. It is hoped that in reporting this novel radiation event others will be stimulated to duplicate the measurements on other devices, and perhaps to offer explanations regarding the origin of the process.

APX 1 OPTICAL PATH

Optical access to the Alcator plasma is limited by construction to six diagnostic ports. Each port offers vertical and horizontal views of the plasma through narrow gaps in the toroidal field magnet called keyways. The horizontal view is preferable for the measurement of cyclotron radiation since it allows sampling of the full frequency spectrum generated by the magnetic field variation. Because of the narrowness of the keyway, only radiation emitted within .10 rads of the perpendicular can be observed directly. When viewed from the outside this keyway is the limiting constriction that determines the observable plasma area. This situation is illustrated in fig.(1). Having passed from the torus, radiation is brought to the detector by a series of front surface mirrors as shown in fig.(2). A spherical mirror images the detector aperture onto the inside edge of the keyway. Since the wavelengths involved are not ignorable compared to the physical dimension of the optics employed, every mirror, window, and aperture is a source of diffraction.

The effective aperture diameter of the Michelson interferometer is 5 cm. Plane radiation incident on this area will be focussed into the detector. In the very short wavelength limit when diffraction can be ignored, this 5 cm diameter would approximately equal the area of the plasma viewed, since the spherical mirror is located halfway between the plasma and the entrance aperture of the Michelson interferometer. For a wavelength of .67 cm, corresponding to the second gyrofrequency at 80 KGauss, diffraction effects will increase this spot size slightly. Tracing backwards from the detector, rays incident upon the spherical mirror will be nearly plane waves, so the

resulting diffraction will be the usual circular aperture Airy pattern.

$$\frac{dP}{d\Omega} \approx \left| \frac{2\, J_1(\alpha)}{\alpha} \right| \qquad \alpha = 1/2\ ka\ \sin\theta$$

EQ (1)

$k = 95\ cm^{-1}$

a = mirror diameter = 15 cm

J_1 = first order Bessel function

The image upon the 10 cm vacuum window will have a maximum extent determined by the imaged aperture size plus the diffraction from the spherical mirror. At 1.5 m from the mirror the first zero of the Airy pattern will be determined by:

$$\Delta r = L\theta_{min} = .4\ cm \qquad L = 1.5\ m$$

EQ (2)

$$\theta_{min} = 2.7 \times 10^{-3}\ rad \text{ (first zero of Bessel function)}$$

The spot size is 7.5 cm, so no diffraction effect from the window is expected. The keyway is 4 cm wide by 30 cm tall, so it will produce the characteristic diffraction pattern of a vertical slit:

$$\frac{dP}{d\Omega} \approx \left| \frac{\sin\alpha}{\alpha} \right|^2 \qquad \alpha = 2\ ka\ \sin\theta$$

EQ (3)

$k = 95\ cm^{-1}$

a = slit width = 4 cm

This will effect only the horizontal direction. By analogy to eq (2) a horizontal diffraction size is found at the plasma centre a 20 cm distance from the 'slit' exit.

$$\Delta r = L\theta_{min} = .16\ cm \qquad L = 20\ cm$$

EQ (4)

$$\theta_{min} = \sin^{-1}(\pi/ka) = 8 \times 10^{-3}$$

This distance is added in the horizontal direction only. The two dimensional spot size at the plasma centre is found by adding the separate horizontal and vertical diffraction effects to the 5 cm aperture image:

EQ (5)

$$\text{Vertical: } \Delta r = \Delta\theta_{min}(\text{mirror})\times 3\text{m} = .81 \text{ cm}$$

$$\text{Horizontal: } \Delta r = \Delta\theta_{min}(\text{mirror})\times 3\text{m} + \Delta\theta_{min}(\text{slit})\times 20\text{cm} = .97\text{cm}$$

The spot size is an oval with first minimum defined by 6.6 cm vertical and 6.9 cm horizontal diameters.

To determine the temperature profile resolution that this spot size mandates it is assumed that the profile is vertically and toroidally symmetric. The vertical resolution is straight forward; using the Rayleigh-Jeans criterion, Δr = 3.3 cm. In the horizontal direction the resolution is determined by the doppler width (and magnetic field ripple). This effect is totally ignorable (or unmeasured and assumed small). The axial (in-out) extent is fixed by the 20 GHz Michelson frequency resolution, Δr = 3 cm. When viewing a temperature profile of 20 cm diameter, the finite spatial resolution will produce a 5% overestimate of the profile width. The effect upon the measured central temperature can be ignored since the calibration process will correct any error resulting from averages over finite volumes. In the case of the Fabry-Perot, sec (5), both the aperture spot size and the frequency resolution were much better, resulting in a more accurate measurement.

APX 2 REFLECTIONS & POLARISATION

None of the optics employed can significantly alter the polarisation state of the emitted radiation. Rotation of the electric vector may result from mirror reflections, but orthogonal polarisations will remain distinct in this process. Reflections within the keyway will retain their polarisation identity since the reflective metal surfaces are planes parallel (perpendicular) to the extraordinary (ordinary) mode polarisation vector. The polarisation mixing mentioned in sec (1) must occur elsewhere if it is to account for the observed ordinary mode radiation. In an effort to demonstrate this effect a reflective mirror was affixed to the back wall of the vacuum chamber [see fig.(1)]. This mirror was designed to image the vacuum window onto itself, so that no randomly reflected radiation could be observed. Reflections within the keyway are not prohibited by this addition, but presumably will not effect the polarisation state. The effective of this beam dump was only a modest 10% improvement in the degree of polarisation, with a significant amount of ordinary mode still present. A further refinement involved the placement of a glass liner on the inside of the port extension. This was intended to absorb any incident radiation, thus preventing reflective polarisation mixing in the port extension. This absorber had no effect upon the measured degree of polarisation. In retrospect, neither experiment provided a severe enough test to either confirm or disprove the polarisation scrambling model. The beam dump was not large enough, and unfortunately could not be aligned properly, while the glass covered only a small portion of the exposed metal surface.

APX 3 THE MICHELSON INTERFEROMETER

The plasma emits a broad spectrum of submillimetre radiation, the intensity varying in time during a tokamak discharge. The function of the Michelson interferometer system is to measure as much of this spectrum as necessary, with the best temporal resolution possible. For the Alcator Tokamak the measured spectrum should include the first three cyclotron harmonics, but need not extend beyond this since intense radiation at higher harmonics is rarely encountered. The mechanics of the interferometer inversely relate time and frequency resolution, so that improvement of one comes at the expense of the other. Of the two, the spectral resolution is the more important. Unless improvement beyond characteristic emission fluctuation times, such as sawteeth, can be achieved, there is no reason for the pursuit of higher temporal resolution. However, the spectral resolution should allow determination of temperature profiles with reasonable spatial resolution since these profiles are the raison d'etre of the interferometer.

In simplest form the Michelson interferometer[1] is a beam splitter with two reflective beam paths. Radiation from the two paths recombines constructively or destructively depending upon the length difference of the two paths. By varying this path difference an interferogram is generated. The interferogram can be analysed to recover the radiation spectrum. In the case of the polarising Michelson interferometer, Fig.(3), the beam splitter is a wire mesh which transmits or reflects according to polarisation. An initial wire mesh selects one polarisation and the beam splitter is arranged to couple equal intensities into the two beam paths. If the path

difference is zero, the beams recombine to form the original polarisation, and are rejected from the interferometer by the initial mesh. If the path difference is one half wavelength, the recombined beam is rotated $\pi/2$ with respect to the original polarisation and is reflected by the initial mesh into the detector. Unlike the conventional device, the polarising interferometer detects a minimum at the zero path difference.

The length of one path is varied by an electromechanical vibrator attached to a reflecting mirror. Typically the vibrator motor is driven at 35 Hz to produce a swing of +-5 mm. The second path length can be varied manually and is adjusted so that the zero path difference state occurs near the extreme of the moving mirror excursion. Two complete interferograms result from one vibration period.

The position of the moving mirror is measured by an auxiliary HeNe laser, so that the path difference is known at all times. The data is sampled at equal intervals of path difference, which because of the sinusoidal mirror drive does not correspond to equal intervals of time. The sampling interval is variable, but is usually 126.5 μm of path difference

Data sampling is controlled by a Z-80 micro-processor. Input to the Z-80 includes the analog interferometer signal, a mirror drive reference signal, and the output of the auxiliary HeNe interferometer. The number of complete vibration periods to be sampled is preselected; typically about 12, which corresponds to the full duration of the plasma discharge. The entire sampling process is initiated by a

trigger from the Alcator sequencer. After sampling the data is transferred to a PDP 11-55 computer for treatment.

APX 4 FOURIER TRANSFORM INTERFEROMETRY

The output of the idealised Michelson interferometer depends upon the spectral intensity $I(\omega)$ and the path difference of the two arms x:

EQ (1)
$$J(x) = \overline{J} - \frac{1}{2} \int_0^\infty I(\omega) \cos(\omega x/c)\, d\omega$$

$\overline{J}$ is the average level of the interferogram $J(x)$ and is equal to one half the total intensity of all frequencies. Experimentally $\overline{J}$ is the non-fluctuating baseline of the interferogram. $I(\omega)$ is related to $J(x)$ by the inverse transformation[2]:

EQ (2)
$$I(\omega) = \frac{-4}{c\pi} \int_0^\infty \cos(\omega x/c)\{J(x)-\overline{J}\}\, dx$$

Provided that $J(x)$ is measured for a semi-infinite range of x, the entire spectrum can be recovered. In practice $J(x)$ can only be measured for a finite range of path difference, hence limiting the accuracy of the deduced spectra.

A standard technique for treating interferograms of finite extent is the process of apodisation. According to this procedure the inverse transformation is:

EQ (3)
$$I(\omega) = \frac{-4}{c\pi} \int_0^L A(x,L) \cos(\omega x/c)\{J(x)-\overline{J}\}\, dx$$

where L is the maximum path difference and A(x,L) is called the apodisation function. Apodisation may be considered a convolution of the true spectrum with an instrumental line shape which reflects the finite resolution capabilities of the system. Different apodisation functions correspond to different line shapes. A triangular apodisation function is fairly standard, and has been employed throughout this thesis:

EQ (4)
$$A(x,L) = \left[1 - \frac{|x|}{L} \right]$$

where L may be chosen equal to or less than the maximum path difference. According to eq (3), the spectrum produced by a triangularly apodised interferogram resulting from a single frequency source, $I_o(\omega_o)$ is:

EQ (5)
$$I(\omega_o) = I_o \frac{L}{2\pi c} \operatorname{sinc}^2 [(\omega-\omega_o)L/c]$$

By way of comparison, the unapodised spectrum is a sinc rather than sinc^2 function. Applying the Rayleigh criterion to eq (5), the condition that two frequencies of separation $\Delta\omega$ be resolved is expressed by:

EQ (6)
$$\Delta\omega = \frac{2\pi c}{L}$$

Thus the resolution is inversely proportional to the maximum path difference, which in turn is the amplitude of the vibrating mirror displacement. For example, a 1 cm total mirror travel (2 cm path difference) provides a conceptual 15 GHz resolution. Since data from

the entire mirror oscillation may not be used, the resolution will usually be less. For data presented in this thesis, the frequency resolution is typically 20 GHz.

The interferogram is actually a series of sampled points, rather than a continuous curve. Hence the integral over x in eq (3) is in reality a summation:

EQ (7) $$I(\omega) = \frac{-4}{c\pi} \sum_{j=0}^{N-1} \cos(\omega j \Delta x/c)\ A(j\Delta x, L)\ [J(j\Delta x) - \bar{J}]$$

where N is the total number of interferogram points sampled. Eq (7) can be used to generate spectral intensities $I(\omega)$ for all frequencies ω, so it must be borne in mind that the resolution is still determined by eq (6). As the frequency in eq (7) is increased, at some point $I(\omega) = I(\omega - 2\pi c/\Delta x)$, and the spectrum will repeats itself. The maximum frequency that may be recovered is determined by the sampling interval:

EQ (8) $$\omega_{max} = \frac{\pi c}{\Delta x}$$

Thus the standard 126.5 μm separation implies a maximum measurable frequency of 1186 GHz.

Although eq (7) as it stands is a perfectly reasonable means of generating spectra, it is rarely used in this form. Instead a derivative expression based upon the Cooley-Tukey algorithm is employed. Called the fast fourier transform, this routine introduces a significant savings in computation time, and for this reason has become the favoured process in fourier transform spectroscopy. A

description of the Cooley-Tukey algorithm can be found elsewhere[3], and for the sake of brevity will not be included. A requirement of the fast fourier transform routine is that the number of sampled points to be transformed be an integer power of 2, i.e.: $N = 2^n$.

To satisfy this requirement a zero-filling technique is used to generate additional interferogram points. The additional points all have zero value, and do not effect the generated spectra. This is seen in eq (7) where the summation can be extended to larger integers without effect provided that the corresponding $J(x)-\overline{J}$ are zero. This is precisely what zero-filling accomplishes.

A complication arising from the discrete nature of the interferogram is a phase shift that results from not sampling a point precisely at the zero path difference. For example, if the nearest sampled point is measured at some displacement δ from the actual zero point, eq (7) should be recast as:

$$I(\omega) = \frac{-4}{c\pi} \sum_{j=0}^{N-1} A(j,L) \cos[(j\Delta x-\delta)\omega/c] [J(j)-\overline{J}]$$

$$= \frac{-4}{c\pi} \cos(\omega\delta/c) \sum_{j=0}^{N-1} A(j,L) \cos(\omega j\Delta x/c) [J(j)-\overline{J}] \qquad \text{EQ (9)}$$

$$+ \frac{-4}{c\pi} \sin(\omega\delta/c) \sum_{j=0}^{N-1} A(j,L) \sin(\omega j\Delta x/c) [J(j)-\overline{J}]$$

Thus if δ is known, the spectra can be recovered provided that the

cosin and sin transforms are both computed. Fortunately, this is manifest in the fast fourier transform.

The raw digitised data from a typical discharge is shown in fig.(4), where the entire analysis process is schematically followed.

(1) The data is segmented into blocks corresponding to individual oscillation periods. Each block contains two interferograms, one for each direction of mirror motion. The second interferogram is backwards with respect to the first, and must be reversed. Now all interferograms may be treated equally.

(2) The $\overline{J}$ level is subtracted from each interferogram. This level is found by fitting a line to the flat part of the interferogram. The line may have a slight positive or negative slope if the emission intensity is increasing or decreasing. The data is scaled accordingly, under the assumption that all frequency components change in the same way. Subtraction of the base level is necessary to avoid generation of large zero frequency spectral components when the fourier transform is performed. Because of the inverting effect of the polarising meshes, the interferogram is next reflected about the new zero level.

(3) Because the sampling of data occurs before the zero path difference is encountered, and since it is unlikely that a sample will be taken exactly at this time, the location of this point in the interferogram must be approximated. A parabolic fit is made to the three largest data points, and the center of this parabola is identified with the zero path difference. δ is determined.

(4) The interferogram is next apodised. A triangular apodisation function is used. Because the employed fast fourier transform routine

requires 2^n data points, the zero filling technique is used, typically to create 2^9 points. Zero filling involves the extension of the interferogram to larger values of path difference by adding data points of zero magnitude.

(5) Since the fourier transform requires equally spaced points starting from the zero path difference point, the interferogram is shifted by the spacing between the first data point and the point closest to the actual zero path point. The small section of interferogram occurring before this point is reattached at the other end, which is allowed because of the periodicity of interferograms. Because the first data point is not the actual zero path point the interferogram is not symmetric about this point. Both cosin and sin components should result from the fourier transform.

(6) The fast fourier transform is now computed, and the sin and cosine components are combined as indicated in eq (9). Corrections due to calibration of the detector response, or absorption in windows or other effects may be included.

The spectra are now available for further analysis. The second or third harmonic may be extracted and studied, or non-thermal components may be investigated. For purposes of data storage, the raw interferometer signal is used, thus allowing for retrospective changes in calibration etc. The time required to reprocess the data is small compared to the benefits gained in this caution.

APX 5 DETECTOR

Regardless of which, if any, interferometer system was used, the same detector was employed. This consisted of an InSb crystal mounted in a liquid helium cooled cryostat. The crystal was manufactured by QMC Ltd[4]. of the United Kingdom. When biased with 100 μamps current, the detector has a sensitivity of about 1 Volt per mWatt of incident radiation. For typical emission power levels of a few μWatts incident on the detector, a 1000 gain amplifier produced a signal level of a few volts. Calibration with a modulated klystron source show that the temporal frequency response of the detector is adequate to at least 100 kHz, so that in general, finite resolution limitations will be set by the data gathering system rather than by the detector itself.

APX 6 CALIBRATION

The problem of calibration is two-fold. When measuring broad spectral features such as cyclotron harmonics, which may vary in frequency due to changing magnetic field, the relative sensitivity of the detection system to the complete range of radiation frequencies is required. Furthermore, if the emission at some particular frequency is to be equated with a physical parameter, such as the second harmonic intensity with electron temperature, an absolute measure of the system sensitivity is needed. Of these two, the first is by far the easier, since it requires only a radiation source of known relative spectral shape. An absolute calibration requires a source of known intensity, as well as a precise determination of the solid angles subtended by the source and by the plasma being measured.

Relative calibration is performed using a mercury arc lamp which approximates a blackbody of a few thousand degrees temperature. Additional sources such as liquid nitrogen cold loads have also been used with similar result. The problem with this technique is that no available broadband radiation source begins to approach the intensity of the plasma. To overcome this inherent source weakness during calibration, many interferograms are averaged by the Z-80. An example of the resulting spectrum is shown in fig.(5). Bearing in mind that this spectrum represents the emission from a blackbody source, it is seen that the system response begins to decrease substantially above 400 GHz. This rolloff results mainly from the detector response, however at high frequencies the interferometer wire meshes will begin to fail as the radiation wavenumber approaches the mesh constant. The problems at low frequency evident in fig.(5) result from the Fourier transform process. The noticeable features near 560 and 760 GHz are due to absorption by molecular water vapour present in the interferometer chamber, a topic of later discussion. As the magnetic field, and consequent cyclotron frequencies, is raised, the decrease in the detector response is offset by the blackbody emission scaling with the square of the frequency, and by the increase of temperature with magnetic field [sec (1)]. For example, the second harmonic emission will increase as $w^{7/2}$, so that the detected signal intensity will not degrade until about 700 GHz, corresponding to a field of 120 KGauss is reached.

Also shown in fig.(5) is a calibration spectrum made with the QMC detector before its modification. The spectral fluctuations at 400 GHz result from channelling in a 1 mm thick quartz disc on which

the InSb crystal was mounted. Modification involved wedging this disc so the faces were no longer parallel, thus preventing channelling. As can be seen, this simple expedient eliminated the problem. For the same reason the window on the detector cryostat is also wedged.

By dividing the spectrum of fig.(5) by the assumed blackbody spectrum, a relative sensitivity curve is obtained. This curve is then used by the cyclotron computer routines to correct measured spectra from the plasma. Not considered by this technique is absorption by the .25" fused quartz vacuum window, an important factor at higher frequencies. This effect need not be considered when dealing with a small frequency range, such as the second or third harmonic alone, because the attenuation coefficient of fused quartz is a weak function of frequency. However it has been included in fig.(1) of sec (4) where emission at the two harmonics is compared, the net effect being a 15% increase in the relative intensity of the third harmonic emission. Above 800 GHz absorption by the fused quartz window will become particularly severe, and a crystal quartz replacement window should be used.

It has been found that the system response is different for the two polarisations. This is due in part to the differing condition of the meshes used to select the incident polarisation. Consequently in fig.(2) of sec (1) a separate calibration was used for each mode to account for this difference.

Absolute calibration is performed by scaling the optically thick second harmonic extraordinary mode emission with an independent measure of the electron temperature. The temperature as measured by

soft x-ray pulse height analysis is the usual basis for this scaling, although the results of sec (4) have been used succesfully in a pinch. The calibration factor arrived at in this fashion remains constant with plasma parameters such as density and current, so that once in agreement the two techniques always generate the same electron temperature. The calibration factor does change when modifications of the optical system due to deliberate or accidental realignment occur. However, if the system is left undisturbed, the calibration will remain in effect indefinitely.

APX 7 ATMOSPHERIC WATER VAPOUR ABSORPTION

The absorption lines seen in the calibration spectrum result from rotational transitions of molecular water vapour. The transitions at 557 and 752 GHz are particularly evident, but less intense lines at 380 and 450 GHz can also be detected. Five other lines occur in the interval from 100 to 900 GHz, but are sufficiently weak to be ignored. As long as the magnetic field is such that the cyclotron harmonics avoid these absorption lines, no significant problem exists. At certain fields, particularly above 90 KGauss, atmospheric water vapour alters the measured spectra and profiles dramatically. In an attempt to alleviate this problem, the entire optical system including the interferometer was enclosed in a plexiglass chamber, and this volume was continuously purged with nitrogen gas. A noticeable improvement resulted, but distortions still remained. Fig.(6) is an example of such an effect. While ruining the temperature profile, the absorption feature does demonstrate the spatial resolution of the system, since the line width of the feature is due entirely to the finite instrumental resolution.

It is useless to hope for a dry day, or to move the detector closer to the vacuum chamber to avoid this problem. The 557 GHz is so strongly absorbent, that under typical conditions a 1 cm air path will produce nearly a 5% reduction in signal.

APX 8 REFERENCES & FIGURES

1.) M. Born, E. Wolf Principles of Optics
Pergamon Press New York (1964)

2.) W. Steel Interferometry
Cambridge University Press, Cambridge (1967)
Contains pertinent discussions of transformations
apodisation, phase shifts, zero-filling .....

3.) R. Bell Introductory Fourier Transform Spectroscopy
Academic Press (1972)
Contains a graphic demonstration of the Cooley-Tukey
algorithm for a case of N=8.

4.) QMC Instruments Ltd.
229 Mile End Road
London E1 4AA
Trivia question: What does QMC stand for?

OPTICAL PATH TOKAMAK INTERIOR

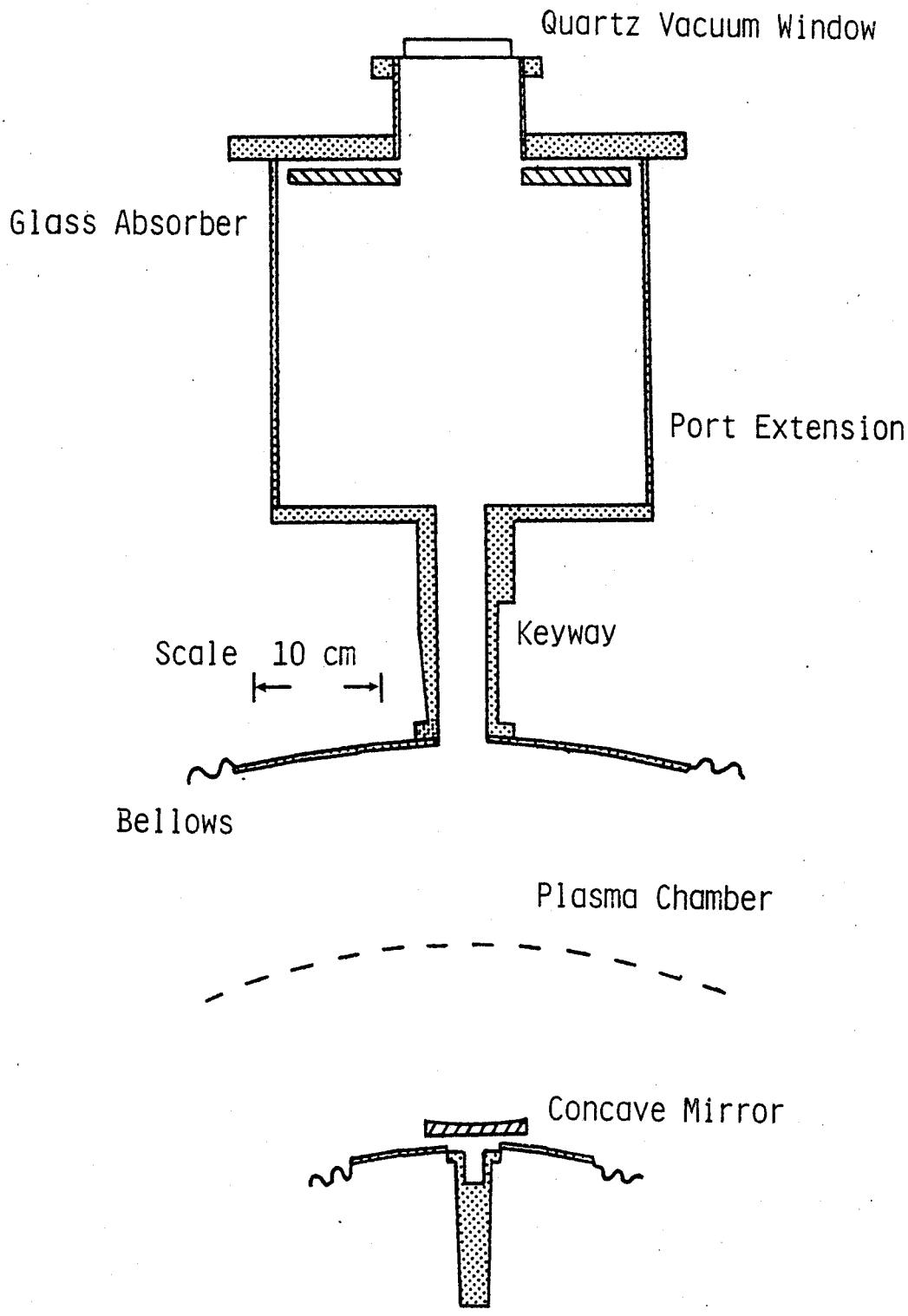

Fig.(1)
Vertical view of torus section slit through the mid-plane. Internal structure is entirely stainless steel except for absorber and window.

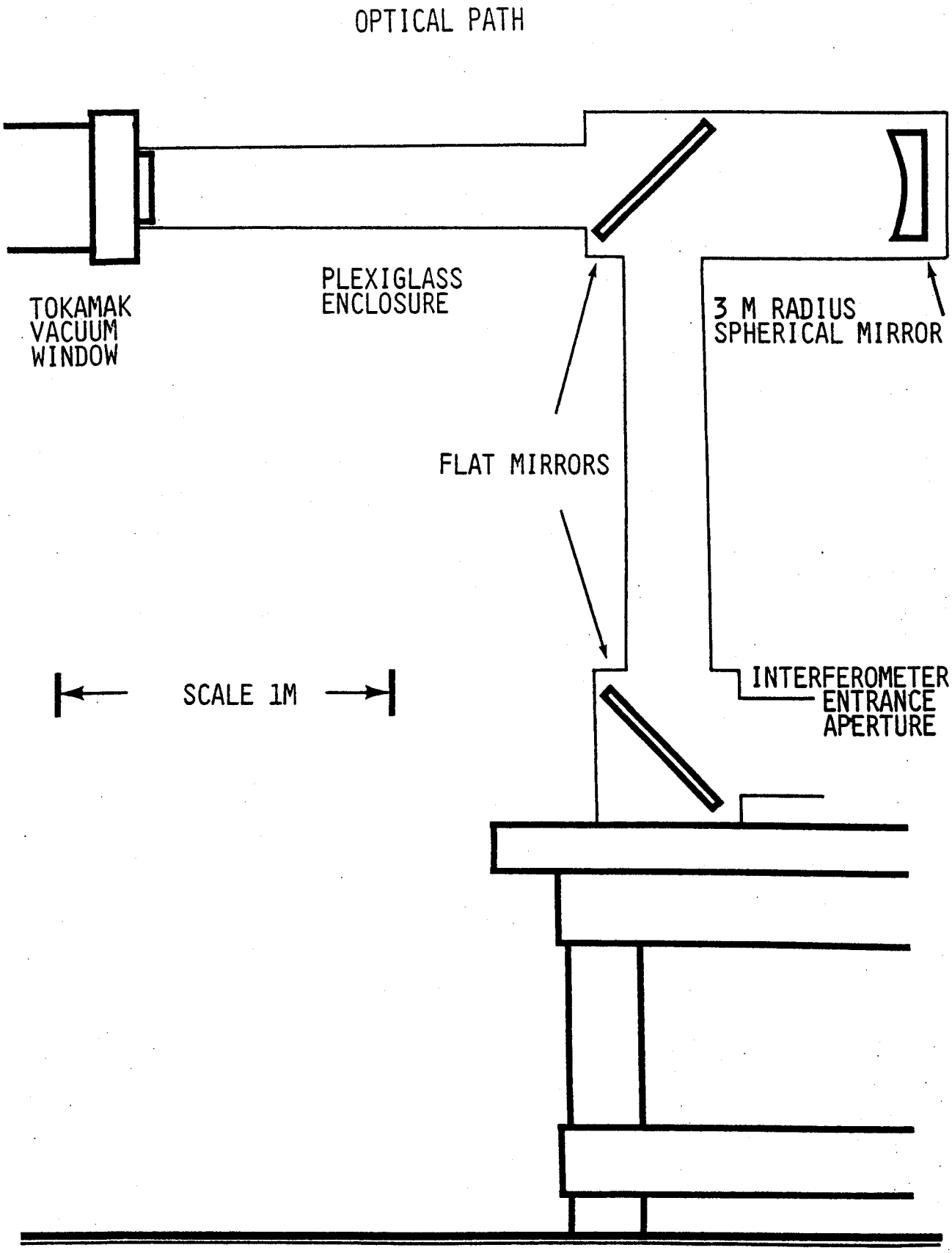

Fig.(2)
All mirrors are front surface aluminium coated reflectors. The enclosure is continuously purged with nitrogen gas, when necessary, to minimise radiation absorption by water vapour.

THE MICHELSON INTERFEROMETER

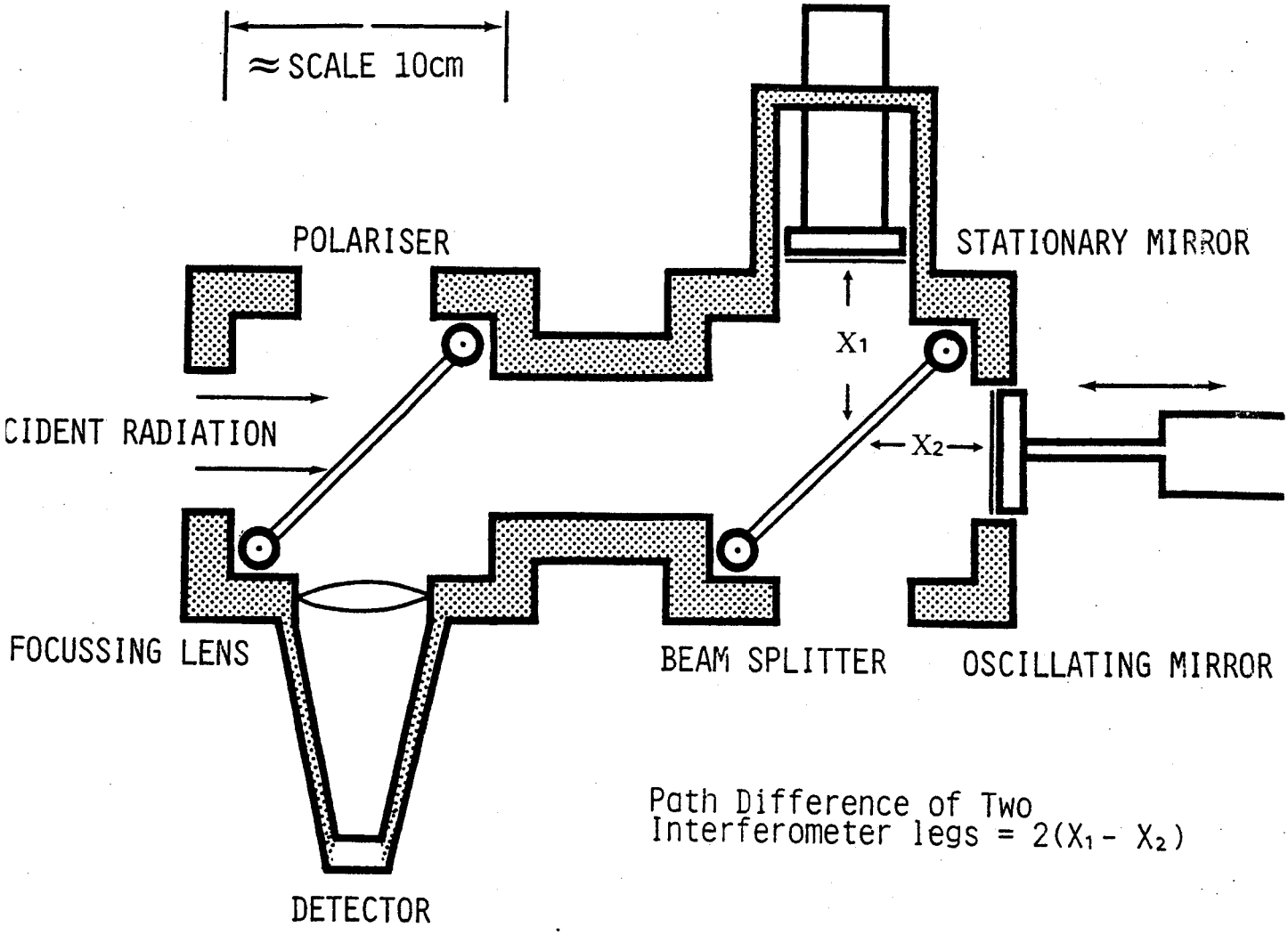

Fig.(3)

Both beam splitter and polariser are wire meshes. Mirrors are flat front-surface aluminised. The initial polariser is selected according to the mode of radiation (Ordinary, Extraordinary) to be viewed. The beam splitter couples equal amounts of either polarisation into the two legs. If the path difference is zero, a minimum signal is detected. By varying the path difference via the oscillating mirror, an interferogram is generated.

DATA PROCESSING

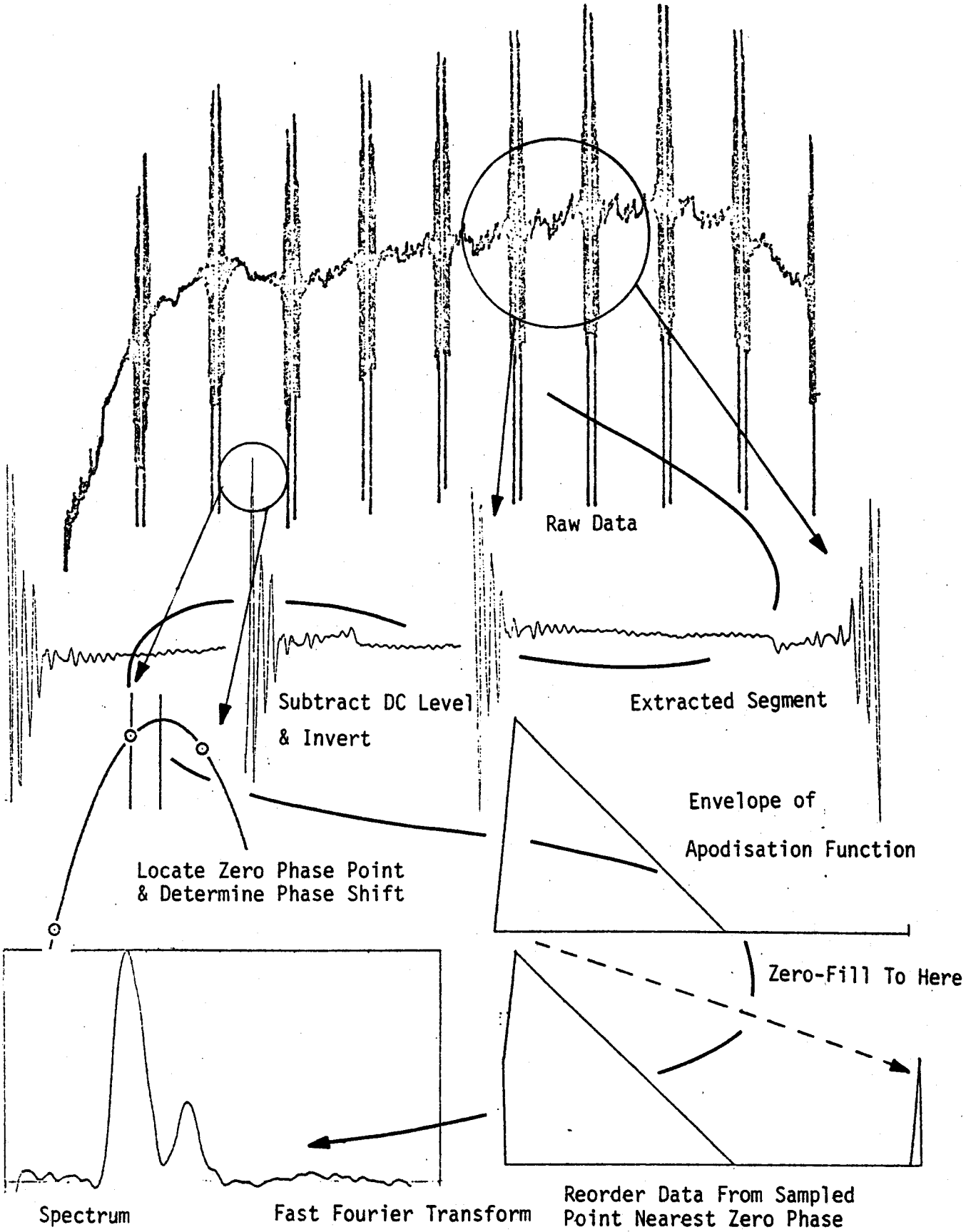

Fig.(4)

CALIBRATION SPECTRA

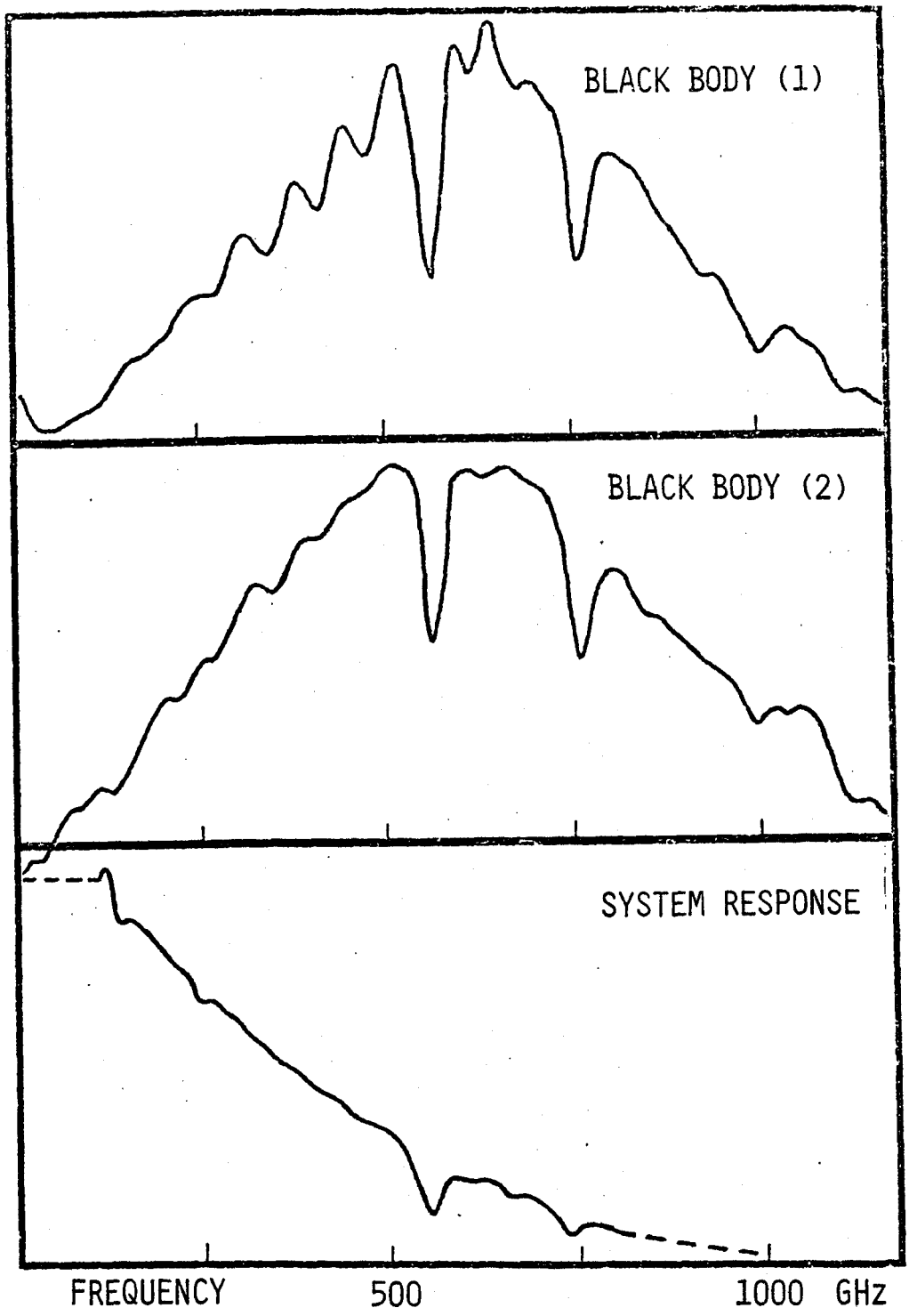

Fig.(5)

First two spectra are produced by black body ($\alpha\ \omega^2$) mercury lamp. Periodic structure in first spectra results from channelling in detector, which has been corrected; second spectra. Relative system response is determined by dividing black body spectrum by ω^2. Vertical scales are arbitrary linear units. Absolute calibration results from scaling $2\omega_c$ emission to an independent temperature measurement.

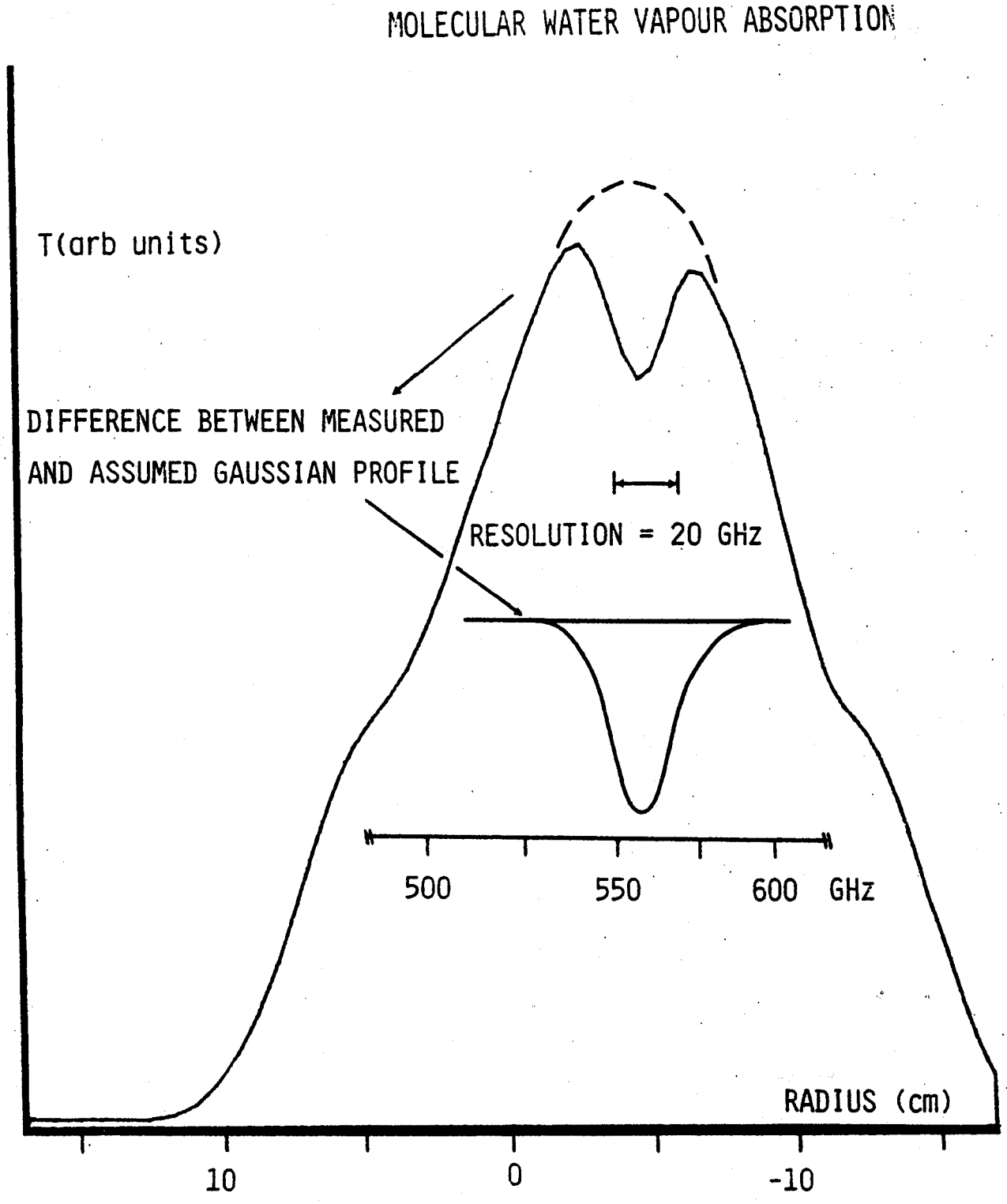

Fig.(6)

Example of 557 GHz absorption feature due to molecular water vapour in the air path between Tokamak and detector. The line width is determined by the instrumental resolution, and is consistent with the 20 Ghz resolution determined by the apodisation technique employed in the fourier transform process.

BIOGRAPHY

BY

WALLACE STEVENS

One must have a mind of winter
To regard the frost and the boughs
Of the pine-trees crusted with snow;

And have been cold a long time
To behold the junipers shagged with ice,
The spruces rough in the distant glitter

Of the January sun; and not to think
Of any misery in the sound of the wind,
In the sound of a few leaves,

Which is the sound of the land
Full of the same wind
That is blowing in the same bare place

For the listener, who listens in the snow,
And, nothing himself, beholds
Nothing that is not there and the nothing that is.

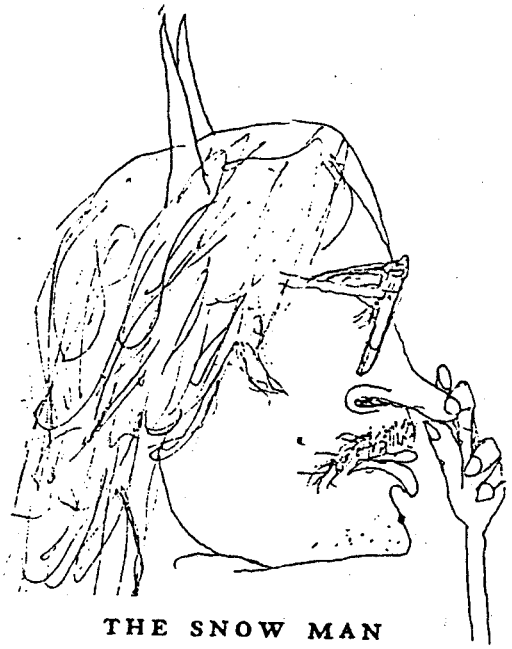

THE SNOW MAN

Fig. (0)

Distribution

B. Coppi
MIT 26-201

R.C. Davidson
MIT NW16-205

PFC Library
MIT NW16-255

U.S. Dept. of Energy
Washington, D.C. 20545
ATTN: DOE Library

General Atomic Company
P.O. Box 81608
San Diego, CA 92138
ATTN: Library

Princeton Plasma Physics Laboratory
Princeton University
P.O. Box 451
Princeton, NJ 08540
ATTN: Library

Associazione EURATOM - CNEN Fusione
C.P. 65-00044 Frascati (ROME)
ITALY
ATTN: The Librarian (Miss C. Depalo)

Association Euratom - CEA
Département de Physique du Plasma
et de la Fusion Contrôlée
92260 Fontenay-aux-Roses
FRANCE
ATTN: Bibliotéque

Prof. Bruce Kusse
Cornell University
Laboratory for Plasma Studies
Ithaca, NY 14850